공학박사학위논문

모세관 현상 기반의 패터닝 기법을 활용한 고효율 삼차원 면역세포 항암효능 평가 플랫폼

Capillarity Guided Patterning Based High-throughput 3D Immune Cell Cytotoxicity Assay

2020 년 8 월

서울대학교 대학원
기계공학부
박 도 현

모세관 현상 기반의 패터닝 기법을 활용한 고효율 삼차원 면역세포 항암효능 평가 플랫폼

Capillarity Guided Patterning Based High-throughput 3D Immune Cell Cytotoxicity Assay

지도교수 전 누 리

이 논문을 공학박사 학위논문으로 제출함

2020 년 4 월

서울대학교 대학원

기계공학부

박 도 현

박도현의 공학박사 학위논문을 인준함

2020 년 6 월

위 원 장 김 호 영 (인)

부위원장 전 누 리 (인)

위 원 신 용 대 (인)

위 원 도 준 상 (인)

위 원 조 덕 (인)

Abstract

Organs-on-chips have been developed for recapitulating human organ functions in *in vitro* as microfabrication techniques meet biology since the early 2000s. Specifically, polydimethylsiloxane (PDMS) based microfluidic devices enabled to mimic organ functions by providing spatially compartmented cell patterning for culturing cells with *in vivo* like layout. The selective cell patterning enabled 3D cell culture and spatiotemporal analysis which were challenging to conduct with conventional cell culturewares such as petri-dishes, flasks, and well-plates. However, traditional organs-on-chips have limitations in salability, experimental throughput, and absence of standard due to their closed channel designs based on PDMS. Here, we introduce two capillarity guided patterning (CGP) methods by integrating microstructures with conventional cell culturewares. First, we fabricated micropillar arrays on open polystyrene (PS) surfaces and the micropillars can capture liquids swept over the surface. Using the devices, we demonstrated 3D culture applications, single cell capturing and retrieval and multiple cell co-culture. Second, we integrated rail-structures with microplate. Beneath a rail-structure, hydrogel precursors can selectively remain according to meniscus dynamics when the pre-loaded precursors are aspirated. These two CGP methods can be produced with injection molding and provide enhanced experimental throughput. Using the rail-

based CGP method, we developed a 3D cytotoxicity assay for cancer immunotherapy based on an injection molded plastic culture (CACI-IMPACT) device to assess killing abilities of cytotoxic lymphocytes in 3D microenvironment through a spatiotemporal analysis of the lymphocytes and cancer cells embedded in 3D extra cellular matrix (ECM). Owing to the aspiration-mediated patterning, hydrogel precursors can be patterned in 12 wells within 30 s. For functional evaluation of the cytotoxic lymphocytes engineered for cancer immunotherapy, HeLa cells encapsulated by collagen matrix were patterned beneath low rails and NK-92 cells were loaded into the channel formed by the collagen matrix. We observed infiltration, migration and killing activity of NK-92 cells against HeLa cells in collagen matrix. Through image-based analysis, we found ECM significantly influences migration and cytotoxicity of lymphocytes. Hence, the CACI-IMPACT platform has the potential to be used for pre-clinical evaluation of *ex vivo* engineered cytotoxic lymphocytes for cancer immunotherapy against solid tumors, and the CGP methods are expected to accelerate the commercialization of organs-on-chips.

Keyword : organ-on-a-chip, high-throughput screening, liquid patterning, open microfluidics, cancer immunotherapy, 3D cytotoxicity assay

Student Number : 2015-20697

Table of Contents

List of Figures

Chapter 1. Introduction

1.1. History of organs-on-chips

Since the advent of polydimethylsiloxane (PDMS), a number of microfluidic devices have been introduced in biological and chemical research field such as diagnostic devices (*1*), chemical gradient generators (*2*), nanoparticle synthesis (*3*), and particle separators (*4*). Especially, PDMS-based devices brought great improve in cell biology due to its characteristics favorable for cell culture. Gas permeability of PDMS enables long term cell culture and transparency of PDMS facilitates observation of cultured cells within the PDMS-based devices (*5*). Most of all, molding microstructures with PDMS revolutionized cell-based studies that were challenging with conventional labwares. For example, microwell devices facilitated studies of heterogeneity of cells and deformation of micropillar array enabled analyzing distribution of forces applied by a single cell (*6, 7*).

Organ-on-a-chip is one of the most successful applications utilizing the characteristics of PDMS advantageous for cell-based studies. Huh et al. opened the era of organ-on-a-chip as they recapitulate organ-level function by utilizing the characteristics mentioned so far (*8*).

Furthermore, hydrophobicity of PDMS enables micro-pores to work as capillary bursting valves that facilitate to arrange cells into physiologically relevant layouts (*9*). Along with the hydrophobicity, elasticity of PDMS allows to apply mechanical stimulation to the cultured tissue so that the device can mimic stretching and relaxation of the lung. Since the lung chip has shown the possibility of recapitulating organ-level function in microfluidic devices, a number of microfluidic devices have been developed, mimicking diverse organ functions such as blood-brain barrier (*10*), gut (*11*), bones (*12*), airways (*13*), and kidney (*14*). Following the development of organ units, there were trials to integrate of the organ chips. In 2014, NIH funded 11 institutions to do the work and DARPA entered into cooperative agreements with NIH award recipients to develop platforms capable of integrating 10 or more organ systems. As a result of the projects, Edington et al. reported interconnected microphysiological systems (MPS), or organs-on-chips, by integrating 4, 7, and 10 MPSs for pharmacological testing (*15*). Although they showed the possibility to connect multiple organ chips and to analyze drug response, they discussed that quantitative analysis is challenging as the number of interconnected MPSs increases. Furthermore, diverse cell sources, culture medium, control of flow rate

make the multi-MPS system difficult to be realized and used by researcher other than the developers. The hurdles in developing multi-organ chip systems has led the trend of organ chip research to develop disease models that are specific applications with a single organ chip. In 2016, NCATS announced a funding opportunity as part of the tissue chips for disease modeling and 13 institutions were funded to develop disease models such as Parkinson's disease, inflammation in muscle, vascular malformations, etc.

Along with the change of research trend and technical improvement in organ chip field over a decade, the field has been matured to commercialization. Emulate spun out from Wyss institute supports kidney, liver, and intestine chips and hardware for manipulating the chips efficiently. They also provide services to execute studies utilizing the chips as customer wants such as toxicity test and drug efficacy test. As their devices are made with PDMS which is challenging to make scalable, they are developing manufacturing systems and enhancing experimental throughput by utilizing hardware. Tissuse is a german company where has profound experience in multi-organ chip devices. Their four-organ (intestine, liver, skin, and kidney) chip demonstrated long-term co-culture of the organs for up to 28 days (*16*).

Instead of using gravity driven flow, they utilize a built in micropump driven by an external pneumatic controller. For the pneumatic control, their device utilizes a thin PDMS film. To address limitations in manufacturing of microfluidic devices using PDMS, some companies develop plastic-based microfluidic chips. Mimetas is a representative company developing well-plate formatted devices produced with thermal plastic. Using their multi-lane devices several research groups reported organ models such as kidney proximal tubule (*17*), blood-brain barrier (*18*), gut (*19*), and glomerular filtration barrier (*20*). Unlike premature era of microfluidics when most of the articles were reported by inventors, recent articles using devices from Mimetas show that commercialized microfluidic devices are widely used by biological researchers.

1.2. Challenges in current organs-on-chips

As commercialized organ chips are used by biologists, pharmaceutic companies, and medical researchers, their usefulness should be verified for prosperity of the market. In order to be used for screening systems in development process of drugs or cosmetic products,

not to be a single time use for novelty in research, some challenges remain to be addressed.

First, improvement in manufacturing process is needed. Making devices with PDMS is time consuming and requires intensive labor. Normally, the fabrication process consisting of PDMS molding, cutting, punching, and plasma bonding takes 1-2 hours and recovering hydrophobic surface after plasma bonding requires one or more days if the device utilizes the hydrophobic surface for cell patterning (*21, 22*). Hence, many organ chip companies produce their products with thermal plastics which are scalable via injection molding.

The second problem is low experimental throughput. Even though they changed material, most of the devices keep using cell patterning methods that utilize capillary bursting pressure between narrow gaps formed by micropillars or microbumps (*23, 24*). As critical capillary pressure at narrow gaps depends on the hydrophibicity of the surface, thermal plastics have smaller critical capillary pressure than PDMS. The lowered critical capillary pressure in plastic devices induces larger patterning failure rate as users can easily exceed the pressure if they are not sufficiently trained. Even though they are skillful for the

patterning process, sophisticated pressure control is required which limits automation of the loading process.

For the last, absence of standard in size and shape causes inefficiency in maintenance and analysis (*25*). Even though a number of organ chip devices have been developed for a decade, there is no standard for their sizes and formats. It means that each device requires customized setup for cell culture and analysis. Furthermore, the variety in designs is not familiar with researchers who do not have experience in microfluidics so that it hinders introducing organ chips to potential users. Berry et al. reported inserts for well-plates generating rail-structure that can work as microfluidic channel (*26*). The article showed the possibility for microfluidics to be combined with conventional cell-culture products which are widely used and compatible with automated equipment. However, commercialized microfluidic devices still have their own formats and the companies develop equipment for handling the microfluidic devices.

It is believed that the limitations are originated from closed channel designs based on PDMS-glass bonding whose opening exist only at inlet/outlet ports. Even though Aim biotech produces microfluidic devices with injection molding (*27*), its experimental

throughput varies with users' skills due to lower hydrophobicity of plastic compared with PDMS. Hence, to address all the limitations, a new approach in design, material selection, fabrication method, and patterning method is required.

1.3. Models for cancer immunotherapy

Cancer immunotherapy is a new approach to treat cancers by increasing cytotoxic capability of patient's immune system against cancer cells. Programmed death-ligand 1/programmed death-1 (PD-L1/PD-1) blockade is one of the most representative therapies of cancer immunotherapy. The blockade enhances recognition of cancer cells by T cells as non-self, inducing cytotoxic activity of T cells against cancer cells. This approach significantly enhanced long-term survival rate compared with conventional therapies such as targeted therapy and chemotherapy (*28*). The great success of immune checkpoint inhibitors led the inventors, Tasuku Honjo and James Allison, to receive the 2018 Novel prize in physiology or medicine.

As the efficacy of immune checkpoint inhibitor is verified and the market share is growing, a number of immunotherapy drugs are developed and are under clinical trials (*29*). The intensive development

of immunotherapy drugs has increased the demand for screening models in the preclinical stage (*30*). Mouse models takes the major position in preclinical studies, however, the immune system reconstituted in mice cannot elucidate the one in the human body even though human immune cells are transplanted (*31*). Furthermore, tumor-immune microenvironment (TIME) consisting of cancer cells, fibroblasts, lymphocytes, and macrophages, is hardly maintained in mouse models. Hence, a need for pre-clinical model recapitulating anti-tumor immune system exists.

1.4. Purpose of Research

In previous chapters, limitations in commercialized organ chip devices and demand for preclinical models screening immunotherapy drugs are introduced. In this thesis, we will introduce two capillarity guided patterning (CGP) methods to address the aforementioned limitations of conventional organs-on-chips. Using CGP, we will introduce a 3D cytotoxicity assay platform for evaluating cell-based cancer immunotherapy. For the CGP methods, microstructures will be integrated with conventional cell culturewares, petri-dish and well-plate, which provide open culture environment. To enhance productivity, we

utilized plastics which can be mass produced via injection molding. In order to enhance experimental throughput, we developed automated patterning system (chapter 2) or simple patterning process (chapter 2 and 3). Lastly, as we utilize standardized culturewares, petri-dish and well-plate, the platforms are compatible with conventional automated equipment such as automated dispensers or automated imaging systems. We believe overall improvement in production, usability, and standardization will maximize the versatility of organ chips, which will lead organ chips to success in the market, not just in the research stage.

In chapter 2, we introduce a fast multiscale microliquid-patterning method on an open surface using embossed microstructures without surface modification for the first CGP method. Arrays of micropillars can trap microliquids when a bulk drop is swept by an elastic sweeper on polystyrene (PS) substrates such as petri-dishes. In chapter 3, we present a swift and robust hydrogel patterning technology, where preloaded liquid in a microfluidic device is aspirated while leaving the only desired section of liquid for the second CGP method. The device is designed such that differing critical suction pressure conditions are established over the interfaces of the loaded gel, which leads to controlled removal of the liquid as negative gage pressure is applied.

In chapter 4, we present a high-throughput 3D cytotoxicity assay platform using the design introduced in the chapter 3. Rail-based microfluidic design was integrated within a single 96-well and the wells were rectangularly arrayed in 2 × 6 to enhance the experimental throughput. The 3D cytotoxicity assay for cancer immunotherapy using an injection molded plastic array culture (CACI-IMPACT) device can assess killing abilities of cytotoxic lymphocytes in 3D microenvironment through a spatiotemporal analysis of the lymphocytes and cancer cells embedded in 3D extra cellular matrix (ECM).

Chapter 2. Microstructure-guided multi-scale liquid patterning on open surface

2.1. Introduction

Cell-based screening is an important aspect of research in a variety of fields. Many miniaturized cell-based assays have been introduced since the development of microliquid manipulation techniques. Robotic printing of microdroplets enabled fabrication of cellular microarrays for high-throughput screening of small molecules (*32, 33*), genomic libraries (*34-36*) and have aided in the study of extra cellular matrices (ECM) to cellular differentiation (*37*). Although cellular microarrays have reduced the resource requirements of screening, this method is limited to screening of adherent cells in a 2D environment, and requires complicated fabrication processes. Droplet microfluidics-based technologies seek to address the limitations of earlier 2D cellular microarray techniques. Droplets containing cells are produced with ultra-fast frequency up to kHz when cell suspension and oil meet at a T-junction of a microfluidic channel. High-throughput screening (HTS) utilizing encapsulated droplets are capable of both single cell based

screening (*38-40*), and multi cellular spheroid screening (*41, 42*). However, droplet encapsulation requires sophisticated instrumentation to control the two immiscible liquids precisely. Moreover, additional observation and control systems are required for the separation of discrete droplets, and sample recovery from separated droplets is more difficult due to rinsing steps (*43, 44*).

Recently, a one-step droplet patterning method, droplet array plate was proposed for cell-based studies (*45*). Partition of hydrophobic and hydrophilic surface regions induces separation of droplets from a bulk drop. The droplet microarray device was applied to a study of cell-cell interaction (*46*), 2D co-culture (*47*), and fabrication of cell-laden hydrogel particles (*48*). Although these platforms are capable of quickly and easily patterning droplets in a single step, the utilization of super-hydrophobic and super-hydrophilic materials necessitates a more difficult and expensive production process for the plate itself in comparison to single substrate platform proposed here.

In this study, we introduce a new liquid-patterning method, which utilizes simple micropatterned pillar arrays on a flat substrate. The microstructures enhance shear force applied to a liquid drop. When driven by an elastic sweeper, bulk liquids are trapped and retained as

small droplets inside area cornered by microstructures. A succeed of liquid patterning was determined by dimensionless parameters and they were validated experimentally. The subsequently derived designs were then applied to single cell screening and 3D co-culturing experiments. This liquid patterning method is: (i) simple and fast, (ii) easily accessible to sample, (iii) able to capture microliquids with high aspect ratios, and (iv) adaptable to various wettability of substrates.

2.2. Materials and Methods

2.2.1. Fabrication of the microstructured PS surface

To fabricate microstructures on polystyrene surfaces, solvent-assisted molding was used as shown in Figure 2.1 (*49*). A negatively micropatterned polydimethylsiloxane (PDMS) mold replica, fabricated with conventional soft lithography, was used as a template. First, the solvent (AZ 1500 Thinner, AZ Electronic Material, Germany) was applied to the micropatterned base of the PDMS mold via immersion. The solvent-wetted PDMS mold was then carefully applied to a PS substrate surface in a reverse peeling motion. Once the solvent-wetted PDMS mold was applied to the

PS surface, the assembly was placed on a 65℃ hotplate for 30 minutes to evaporate the volatile solvent and to cure the molded PS substrate. At this time, the solvent on the PDMS mold surface dissolved the PS surface and rearranged the dissolved PS solution inside the micropatterned grooves of the mold. Upon evaporation, the solvent deposited the dissolved PS in the shape of the negative PDMS micropatterns, leaving a positively structured PS surface. After curing, the PDMS mold is detached from the now embossed substrate. For the cell culture, the newly patterned PS surface was ventilated for three days in room conditions to remove any residual solvent.

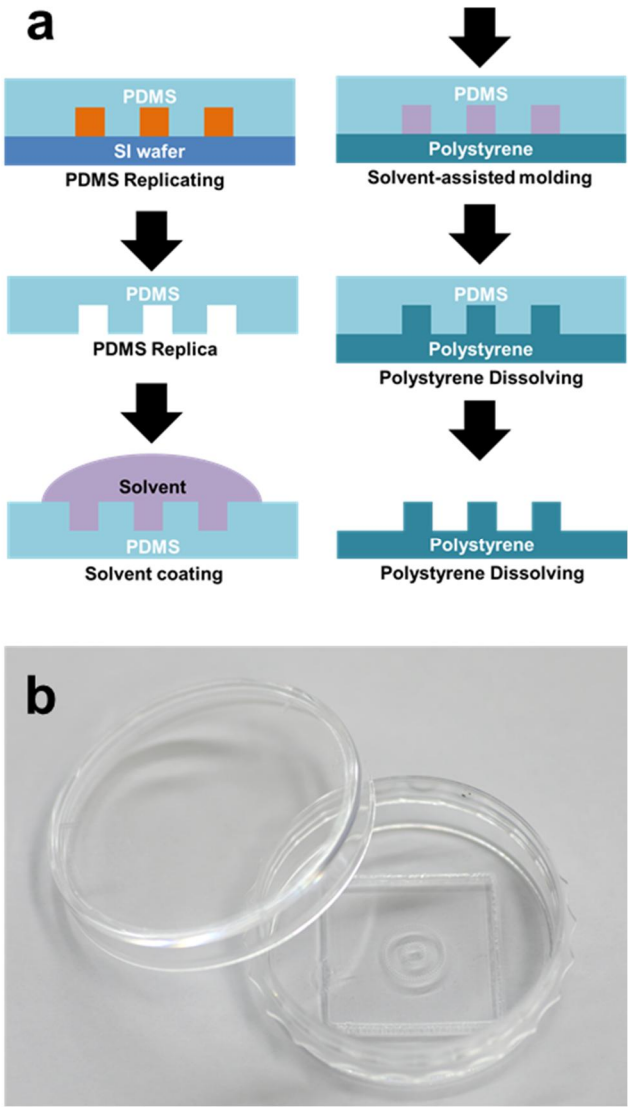

Figure 2.1. (a) Schematic diagram of solvent-assisted molding. (b) A petri-dish with microstructures molded via solvent-assisted molding. Micropillars are molded with concentric doughnut-shapes on a conventional 35 mm diameter petri-dish. *In vitro* blood vessel vasculogenesis was demonstrated with this device.

2.2.2. Single cell isolation and retrieval of single colony

A wild-type CC-124 strain and a mutant strain with the GFP gene CC-4488 (D1blic::D1bLIC-GFP, Chlamydomonas center) were prepared at a concentration of 0.7 x 10^6 cells/ml. The two cell suspensions were mixed at a 1:1 ratio and the mixture was then mixed with a 4% alginic acid sodium salt (Sigma) solution at a 1:1 ratio again. A cell suspension with a density of 0.35 x 10^6 cells/ml in the 2% alginic acid sodium salt solution was formed as a result. The cell suspension was patterned on an embossed dish for a single-cell analysis and polymerized with a 2% $CaCl_2$ solution. After 10 seconds of polymerization, the solution was replaced with TAP medium. The patterned cells were then cultured for two days.

For recovery of the colonies, the medium was drained and 2 μl of a 0.2 M EDTA solution was introduced above the patterned alginate gel. After 10 seconds, the mixture of the degraded alginate gel and the EDTA solution was retrieved with a micropipette and applied onto an agar plate with a TAP+N medium. The colony was cultured for seven days again to increase its population, and it was genetically verified whether the strain was the mutant or the wild type. The CrGFP plasmid, CC-4488 (D1blic::D1bLIC-GFP) strain

and CC-124 (137c mt–) strain were from CC-124 (137c mt–)r, and the genomic DNA of these strains was extracted by the traditional PCI (Phenol : Chloroform : Isoamyl alcohol (25:24:1 v/v)) method. Subsequently, 20 ng of each sample was amplified by i-Taq with Maxime PCR PreMix Kits (iNtRON Biotechnology, Cat. No.: 25035) using 10 pmole of GFP gene-specific primer pairs, a forward primer (5'-GACGGCAACTACAAGACCC-3') and the corresponding reverse primer (5'-TGTACACGTTGTGGGAGTTG-3'), with 40 cycles at 95℃ for 20 seconds, at 56℃ for 20 seconds, and at 68℃ for 25 seconds. The PCR product of 148 nts was separated by 2.0% agarose gel electrophoresis.

2.2.3. *In vitro* vasculogenesis

Human umbilical vein endothelial cells (HUVECs, Lonza) were cultured in an endothelial growth medium (EGM-2, Lonza) and passaged from 4 to 7. Normal human lung fibroblasts (LFs, Lonza) were cultured in a fibroblast growth medium (FGM-2, Lonza) and passaged from 6 to 9. All cell types were maintained at 37°C in 5% CO_2 in a humidified incubator. The HUVECs and LFs

were then detached from the culture dishes, centrifuged for two minutes at 1100 rpm and suspended at a concentration of 6.67 x 10^6 cells/mL in EGM-2. Fibrinogen powder from bovine plasma (F8630, Sigma-Aldrich) was dissolved in phosphate-buffered saline (PBS, Hyclone) and with 0.45 U/ml of aprotinin (A1153, Sigma-Aldrich) added to create a fibrinogen solution with a concentration of 10 mg/ml. The prepared fibrinogen solution and cell suspension were then mixed at a 1:3 ratio, finally creating solutions of HUVECs and LFs with fibrinogen concentrations of 2.5 mg/ml and cell densities of 5 x 10^6 cells/ml. The mixture of HUVECs was then mixed with thrombin at 50 U/ml (T4648, Sigma-Aldrich) at a volume ratio of 50:1 and quickly dropped uniformly on a patterned petri dish as soon as the mixing was done. The mixture was gently swept with a PDMS block to ensure that the gel solution was evenly dispersed and to have the pillar arrays trap the gel with cells. After three minutes for the gel to be polymerized, the mixture of LFs was introduced to fill the area guided by the previously patterned gel. EGM-2 was applied to fill the petri dish again after three minutes. The samples were cultured in a humidified incubator at 37℃ with 5% CO_2 for five days. The

medium was replaced with fresh medium on the third day by gently suctioning the old medium from the edge of the dish while not touching the microstructures where the gel was trapped.

2.2.4. Visualization of *in vitro* blood vessel

After fixing the samples with 4% paraformaldehyde buffered in PBS for 15 minutes, they were treated for 20 minutes with 0.15% Triton X-100 (Sigma) for permeabilization and one hour with bovine serum albumin (BSA, Sigma) to block nonspecific binding. To visualize the blood vessel networks, the samples were incubated with a mouse monoclonal antibody specific for human CD31 (AlexaFluor®488 conjugated, BioLegend) overnight at 4˚C. DNA was stained using Hoechst 33342 (Molecular Probes) for one hour at room temperature. For the z-projection of the 3D blood vessels, stained samples were imaged with an Olympus FV1000 confocal microscope using a 10x objective lenses. To display the vessel network patterned in large areas, the images from each field of view were captured and stitched using software.

2.3. Results and Discussion

2.3.1. Liquid patterning process

Liquid patterning process can be divided into two steps, infiltration and retention, as shown in Figure 2.2. First, liquid should infiltrate into the area cornered by the pillars. Physical conditions to determine whether infiltration would occur spontaneously on arrays of micropillars were studied on the basis of thermodynamic arguments (*50, 51*). Theoretical studies of the dynamics of infiltration process were reported (*52, 53*). If infiltration is not energetically favored, however, the structure will pin the meniscus and form an air pocket as illustrated in Figure 2.3a. Even in such a case, liquid can still be squeezed into the gap by applying additional pressure. In this study, the additional pressure is applied as a bulk liquid is swept by a PDMS block.

Retention corresponds to the separation of a targeted volume of liquid from a bulk liquid. The shear force acting on the liquid by the surrounding solid structures induces deformation and eventual separation (*54*). The critical speed of separation is known to decrease by using microstructures (*55*) and hydrophilic chemical treatments (*45*).

In this work, micropillars on PS plates formed by solvent-

assisted microcontact molding enhance the shear force to break up the liquid into tiny droplets. A minimal unit of the pattern is a 2X2 rectangular array of circular pillars. We sweep the liquid by moving the substrate with a velocity of U=30 mm/s relative to an elastic sweeper, using a prototype of automatic patterning system (Figure 2.4). We investigate whether the patterning scheme works as geometric parameters of the microstructures are changed: the height of pillars, h, ranges from 50 to 200 μm, and center-to-center distance, l, ranges from 130 to 410 μm. In addition, we test with various liquids of different viscosity, μ, and surface tension coefficient, γ. The physical properties of the liquids with critical advancing and receding contact angles, θ_{A} and θ_{R}, on the PS plate were measured with Smartdrop (FEMTOBIOMED.inc, Korea) as listed in Table 1.

We now consider the mechanical condition to cause infiltration of the liquid into the area cornered by the four pillars of diameter, d=100 μm, as shown in Figure 2.3a. For the liquid to replace the air pocket, an interface straddling the pillars spaced by l should meet the neighboring interface. When the interfaces advancing into the empty area with the advancing contact angle θ_{A} touch each other, the curvature is calculated to be $\kappa = 2\sin(\theta_{\mathrm{A}} - \pi/4)/\left(\sqrt{2}l - d\right)$. Then the Laplace pressure of

the given configuration is given by $\gamma\kappa$. The pressure of the liquid relative to the atmospheric gas pressure, which is scaled as $\sim\gamma/L$ with L being the characteristic thickness of the bulk being swept, should be strong enough to generated the foregoing Laplace pressure to enable the merging of the interfaces. Therefore, the dimensionless parameter that determines whether the liquid fills the area cornered by the pillars is given by the ratio of the two relative pressures, γ/L and $\gamma\kappa$:

$$\Pi_{\text{infiltration}} \sim \frac{(\sqrt{2}l-d)}{2L\sin\left(\theta_{\text{A}}-\frac{\pi}{4}\right)} \qquad (1)$$

This consideration only holds for the advancing contact angle higher than 45°. Otherwise, the liquid spontaneously fills the volume between the microstructures because of the concave curvature of liquid-air interface. If the center-to-center distance between the pillars, l, is large, the liquid easily fills the patterning area. Our experimental results with the thickness of bulk liquid fixed at $L \approx 2.6$ mm are plotted in Figure 2.3b, which clearly shows that whether the infiltration succeeds or fails is determined by the value of $\Pi_{\text{infiltration}}$.

To achieve successful retention, the bulk liquid should shed a tiny droplet as retained by the pillars (Figure 2.3a). If the liquid that used

to fill the patterning area is dragged with the bulk, the patterned area is re-occupied by the air. Since the retention behavior is critically dependent on whether the viscous shear force exerted by the sweeper exceeds the capillary force that tends to keep the drop intact, we introduce the ratio of the viscous force to capillary force, the Capillary number, $\mathrm{Ca} = \mu U/\gamma$. The viscous force in the liquid consists of the forces acting at the bulk and near the contact line (*56*). For a liquid trapped in the space cornered by the pillars with the aspect ratio $h/(l-d) \sim 1$, the viscous force near the contact line dominates that in the bulk (*57*). Integrating the shear stress in the wedge-shaped region near the contact line with the receding contact angle θ_{R}, we obtain the scaling estimate of the shear force as $\sim \mu U(l-d+2h)\cot\theta_{\mathrm{R}}$. This estimate is valid for $\theta_{\mathrm{R}} < 90°$, which is the case for most surfaces except for superhydrophobic ones. The capillary force that resists the shearing is scale as $\gamma(l-d)$. Therefore, the boundary whether the liquid that has filled the patterning area would be retained is given by the ratio of the foregoing forces:

$$\Pi_{\mathrm{retention}} \sim \left(1 + \frac{2h}{l-d}\right) \mathrm{Ca} \cot\theta_{\mathrm{R}} \qquad (2)$$

Denser and higher pillars lead to higher $\Pi_{\text{retention}}$, which facilitates the retention of the droplets in the patterned area. Figure 2.3b shows that the experimental conditions having the value of $\Pi_{\text{retention}}$ higher than a critical value lead to successful retention while those with lower values fail.

We also verified the patterning regime with lower values of surface tension and contact angle by mixing surfactant (TX 100) that result in larger dimensionless numbers. As we expected, small droplets were separated from bulk drop in all cases (Figure 2.5). However, the microliquids were not pinned as the initial shape in higher density of surfactant. This may allow the adjacent droplets to merge, but the merging of droplets cannot happen in applications for cell-based assay because the PS surface and water-based solutions have larger contact angles and surface tension coefficients.

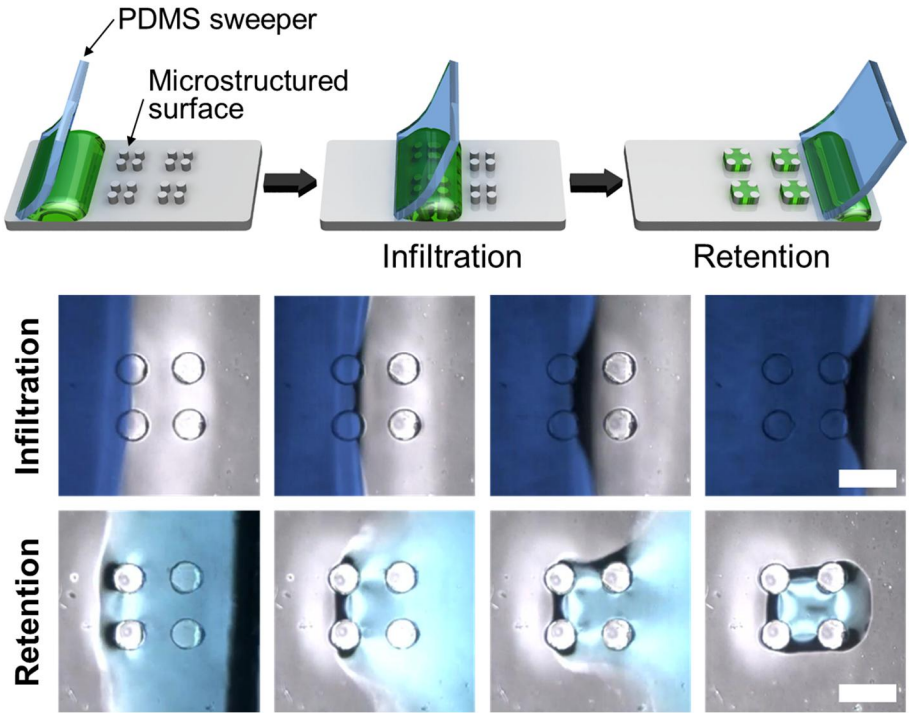

Figure 2.2. Process of the microstructure-mediated liquid patterning on a positively structured surface. A bulk drop, swept by an elastic sweeper, leaves small droplets in the patterning area cornered by the microstructures. The liquid patterning process consists of two steps: infiltration and retention. Scale bar: 200 μm.

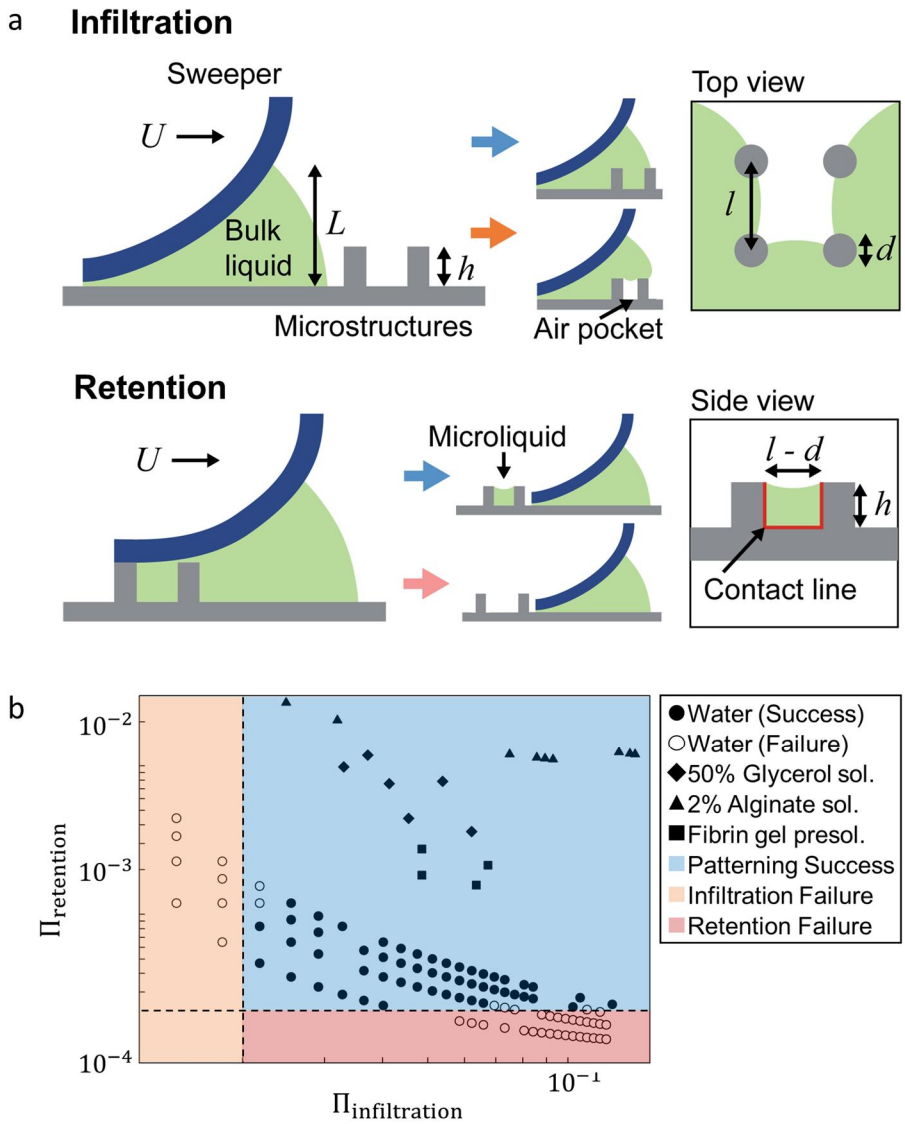

Figure 2.3. The effect of liquid properties and geometries to the liquid patterning process. (a) A schematic demonstration of the success and failure of the two patterning processes. (b) Results obtained from the dimensional analysis are plotted on a graph with axes of dimensionless numbers. To succeed, both of the dimensionless numbers $\Pi_{infiltration}$ and $\Pi_{retention}$ must exceed the value of the boundaries.

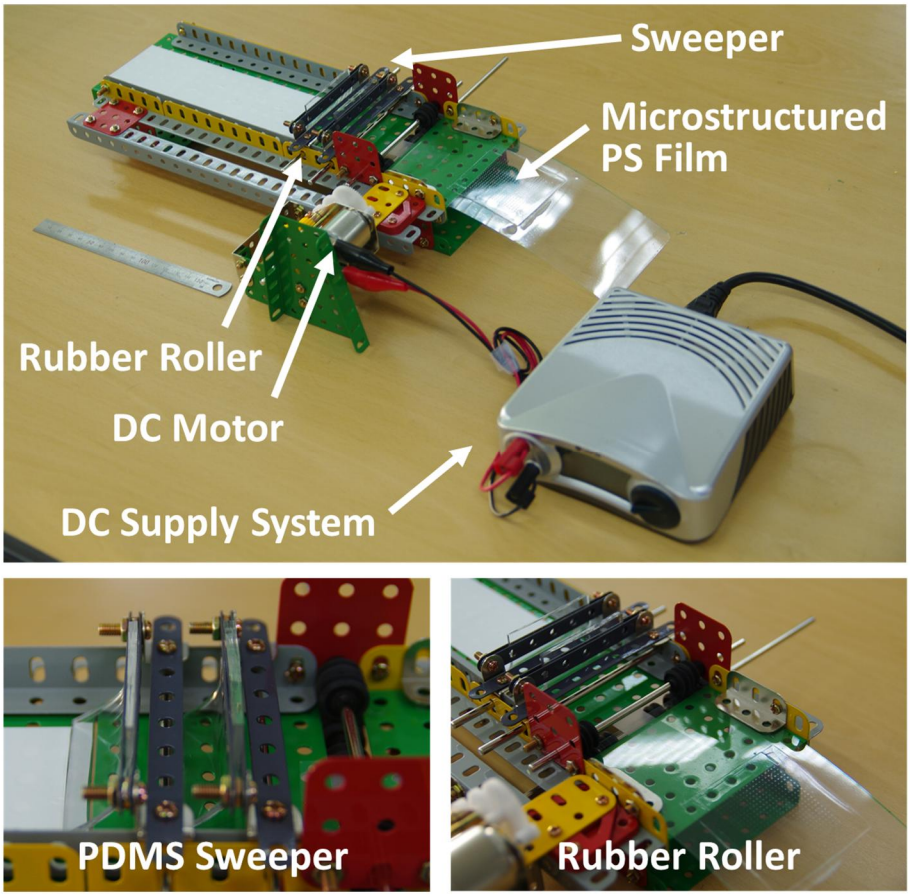

Figure 2.4. A prototype of automatic sweeping system. The rubber roller transports a micropatterned PS film under a fixed PDMS sweeper. This system provides stable sweeping speed and uniform contact between the sweeper and the film.

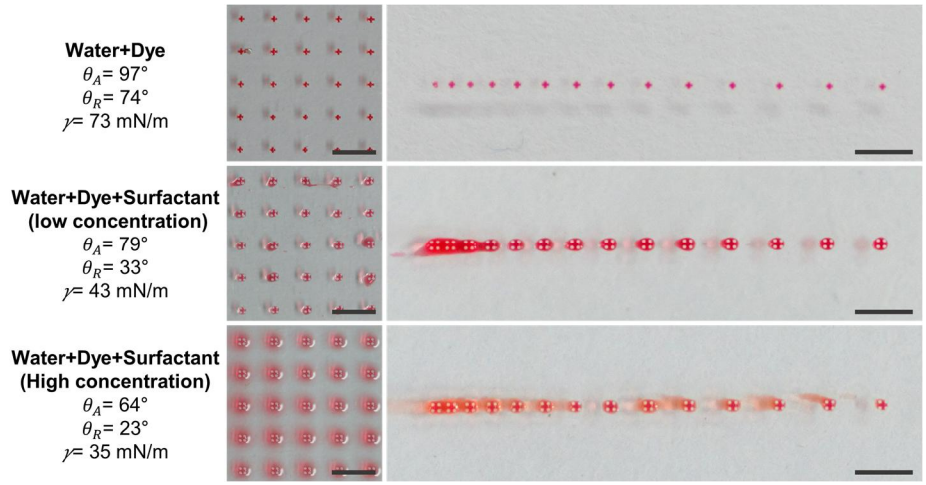

Figure 2.5. Result of droplet patterning with liquids having various contact angles on PS surfaces and surface tension coefficient. The droplets deform to lower surface energy after retention. In the right figures, the patterning spots are arrayed with spacing ranging from 300 μm to 1500 μm. Closely patterned droplets merged when the liquid has low contact angle and surface tension coefficient. Triton X 100 was added to dyed water as surfactant with volume ratio of 0.008% and 0.02% for low and high concentration condition, respectively. The height of pillars is 100 μm and scale bar is 2 mm.

Liquid	Surface tension [mN/m]	Viscosity [mPa·s]	Advancing/receding contact angle [°]
Water	72.9	0.853	92.8/72.9
50% aqueous glycerol solution	57.0	4.66	85.8/51.3
2% alginate solution	58.0	26.8	94.4/61.0
Fibrin gel pre-solution	57.2	1.33	91.4/37.2

Table 1. Physical properties of the liquids used in the experiments

2.3.2. Comparison of microliquid trapping with a micropillar array and microwells

Microwell devices are similar to micropillar arrays in that both mechanisms utilize surface microstructures. Microwells are one of the most widely used platforms for single cell studies such as selection of hydrodoma (*58*), screening of circulating tumor cells (*59*), DNA damage analysis (*60*), and genome sequencing of single cells (*61*). The popularity of microwell devices is due to the compactness of the experimental platform with thousands of trapping wells in a substrate no larger than a glass microscope slide. Filling liquids in a microwell requires that the free surface of the liquid makes contact with the bottom of the well substrate, and failure to make contact results in a large rate of unsuccessful capture. To mitigate patterning failures, many microwell devices require hydrophilic surface treatment. In comparison, micropillar arrays have more accessible faces for fluid entry, translating to more opportunities for fluid capture. In this chapter, we will compare the patterning efficiency of both structures through dimensional studies and suggest suitable cases for each patterning method.

For a quantitative comparison of patterning with micropillar arrays and microwells, we fabricated micropillar arrays and microwells

to capture square-shaped liquids with side lengths, *w*, of 100, 300, and 500 μm, respectively. For pillar arrays, 100 μm by 100 μm square pillars were arranged at center-to-center intervals of 200 μm, which was confirmed to succeed the patterning in the previous section. Figure 2.6 shows the liquid patterning schemes on both structures and the results of the patterning by changing the height of pillars and the depth of wells from 10 μm to 200 μm. For the micropillar array, the patterning efficiency increased as the height was increased while the efficiency on the microwell decreased as the depth was increased.

The results show that micropillars are capable of capturing microliquids at higher aspect ratios than microwells. However, the positive pillar array requires long distance between each patterning area to make the patterned liquid separated perfectly. Hence, microwell devices can be used for the case that large number of samples, imaged in a single focal plane, are required while micropillar array is suitable for screening the development of cells in a 3D microenvironment as will be further discussed in this paper.

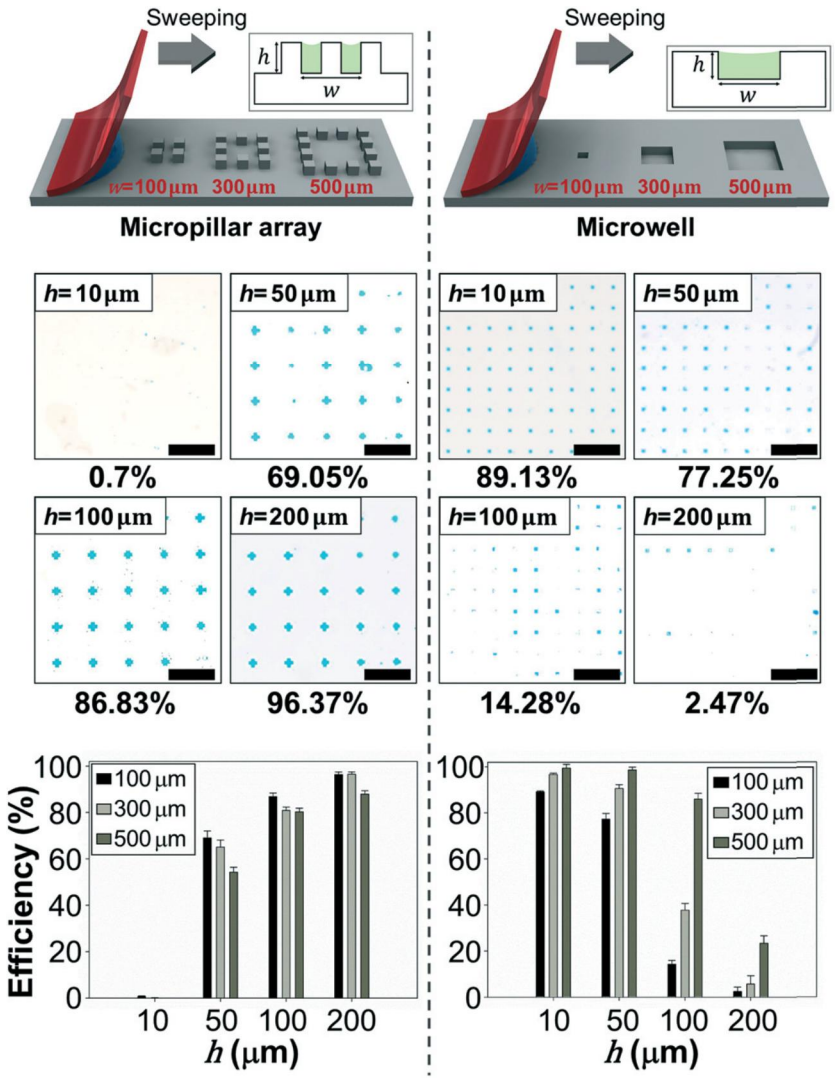

Figure 2.6. Comparison of the liquid-capturing efficiency between positive and negative structures on PS substrates without hydrophilization. The blue dyed water was swept over square pillar arrays whose center-tocenter gap is 200 μm and over microwells whose one side length is 100 μm. Taller micropillars increase the number of trapped droplets while deeper microwells decrease the number. The graphs show the same tendency when the patterning area has longer sides. Scale bar: 1 mm.

2.3.3. Arrangement of micropillars for controlling volume and shape of patterned liquids

The shape and volume of liquid can be controlled by arranging pillars in patterned arrays as shown in Figure 2.7a-e. First, the height, spacing, and number of pillars can be adjusted to control the volume of the patterned liquid. By arranging pillars at a height of 100 μm on a 2X2 array at intervals of 100 μm, water droplets can be patterned with approximate volumes of 5.5 nl. To pattern a larger volume, pillars are placed in the boundary and added inside to guide liquids. Therefore, liquids can be patterned on various scales from nanoliters to microliters. Furthermore, the patterned shape of the liquid can be determined by the arrangement of the pillars. Two rows of pillars were arranged in a curve, and it was possible to trap liquids in the designed shapes on the surface. In the case of patterning lquids in a pattern containing an acute angle, there is potential for off target liquid trapping to occur on the interior of the angle outside of the post boundaries due to the proximity of guiding posts on either side of the patterning array. Such off target liquid patterning can be avoided by incorporating a design which specifically arranges the interior arrays outside of the patterned areas to have lower values than the critical dimensionless numbers described in the chapter

2.3.1.

The shape of the micropillars itself can also be designed to control the patterning efficiency or the uniformity of patterned liquids. A patterned surface with arrays comprising of two bilaterally symmetrically facing “C” shape micropillars was compared to a surface with cylindrical four pillar arrays. It was determined that patterned arrays with a greater number of open faces, such as the 2X2 pillar configuration, resulted in a higher fluid infiltration rate while arrays with a larger contact area between captured liquids and the substrate, such as the C shape arrangements, resulted in greater uniformity of the patterned fluids. (Figure 2.7f) The method measuring volumes of the patterned liquids is described in supplementary information.

Although the basic form of 2X2 pillar array showed volume variation of 10% (CV%), the expanded forms (Figure 2.7b-d) showed smaller variation (2-5%) because most of the variation comes from the boundary of patterning area. As a whole, the proposed microstructure guided patterning mechanism resulted in droplets with a variability of volumes (<10%) comparable to other microfluid patterning techniques at the nanoliter scale: droplet microfluidics (1-3%) (*62*), inkjet printing (<3%) (*63*), electro wetting (12-17%) (*64*). Further improvements in

droplet uniformity can be achieved by controlling for environmental humidity and by refining the uniformity of the sweeping mechanism.

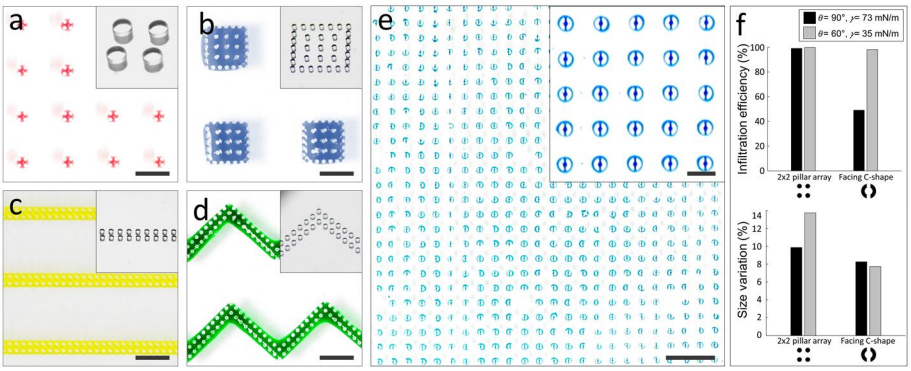

Figure 2.7. Various multi-scale liquid patterns ranging from nanoliter to microliter scale, formed on microstructure-embossed surfaces. (a–d) All pillars have heights and diameters of 100 μm and scale bars represent 1 mm. The approximate volume of each pattern is as follows: (a) 5.5 nl, (b) 140 nl, (c) 850 nl, and (d) 1.3 μl. (e) A 55 mm × 55 mm array of C-shaped pillars captured approximately 8000 droplets within a second of sweeping. Scale bar: 500 μm (magnified image), 2 mm (large area). (f) Effect of the geometry of the pillars on the patterning quality. Facing C-shaped microstructures result in a lower infiltration rate, while they enhance the uniformity of trapped liquids. The black column is DI water and the grey column is DI water with Triton X 100 (0.008%, v/v).

2.3.4. Single Cell Culture & Recovery Platform

Along with the development of microfabrication methods, a number of single-cell analysis platforms have been developed (*65-67*). However, only a few platforms enabled both of spatiotemporal analysis and retrieval of a specific cell from the isolated samples. Infrared laser mediated release of single cells trapped in microwells was introduced (*68*). A separate microchannel based device integrating single particle trap and its release using bubbles generated by IR laser was also developed (*69, 70*). These platforms require perfect alignment between the device and the laser system, and the heat generated by the laser can lower the viability of handled cells. Dielectrophoretic (DEP) force mediated single cell trap methods can capture single cells with a high success rate, but they require a complex and expensive multilayered chip with integrated electrodes and off chip circuitry (*71, 72*). Recently, a microfluidic chip for single-cell trap and selective release using pressure actuated microfluidic OR logic gate was proposed (*73*). Although this platform had high efficiency of extraction, sophisticated controls were necessary for the OR logic gate and backflow. In this chapter, we are introducing a simple single cell analysis platform on which single cells can be patterned, cultured, and retrieved without cross-contamination

between nearby colonies.

We used 2X2 rectangular arrays of circular pillars (d= 100 μm, l= 200 μm, and h= 100 μm). An array of trapping spots was molded on a petri dish with a diameter of 60 mm. Each patterning spot has a coordinate and an indicator to enable efficient screening and recovery. Alginate gel containing microalgae was patterned through a simple sweeping motion as described in the experimental section. After two days of cultivation, single colonies grown from a single microalga was retrieved, following the process of Figure 2.8a. We experimentally found the cell concentration in alginic acid solution that maximizes the portion of patterned spots having single cells. Figure 2.8b shows the distribution of cells in trapping spots according to the cell density. The portion of spots with a single cell was maximized at 32.8% when the density was 0.35×10^6 cells/ml. After two days of cultivation, the single cells grew to form colonies with a top view area of 1.31×10^{-3} mm^2 on average (n=7) (Figure 2.8c). To demonstrate the retrieval of a single colony, we patterned two types of microalgae: CC-4488, a mutant strain with green fluorescence and CC-124, a wild type. The coordinates of patterning spots possessing a single cell were recorded, and after two days, cell types were distinguished according to the presence of green fluorescence

(Figure 2.8d). Using an EDTA solution to dissolve the alginate gel, we retrieved the single colonies of both CC-124 and CC-4488 with a micropipette and the naked eye with the help of the coordinates and indicators. To verify the absence of cross-contamination during retrieval process, a genetic analysis was conducted. The extracted colonies were cultured on agar plates with the TAP+N medium for one week to obtain sufficient populations for gene amplification. Through GFP gene amplification and electrophoresis, as shown in Figure 2.8e, the GFP gene was not found in the sample without green fluorescence. This means that this patterning platform can isolate only one cell from a sample mixed with various strains and provide a chance to retrieve colonies consisting of a single strain.

Even though the maximized single cell throughput of this platform is smaller than that of other platforms using external forces, on the scale of single cells, the throughput of this platform (32.8%) was similar to those of other platforms following Poisson statistics: Droplet microfluidics (<36%) (*74*), microwells (32%) (*75*), and oil-covered cell array (32%) (*76*). The density of the patterning area is limited due to the positive pillar array, however, the device can be easily and cheaply fabricated with more patterning areas in a larger PS substrate using one

step of solvent molding or injection molding. We expect to obtain thousands of single cell samples in a device whose price is just one dollar.

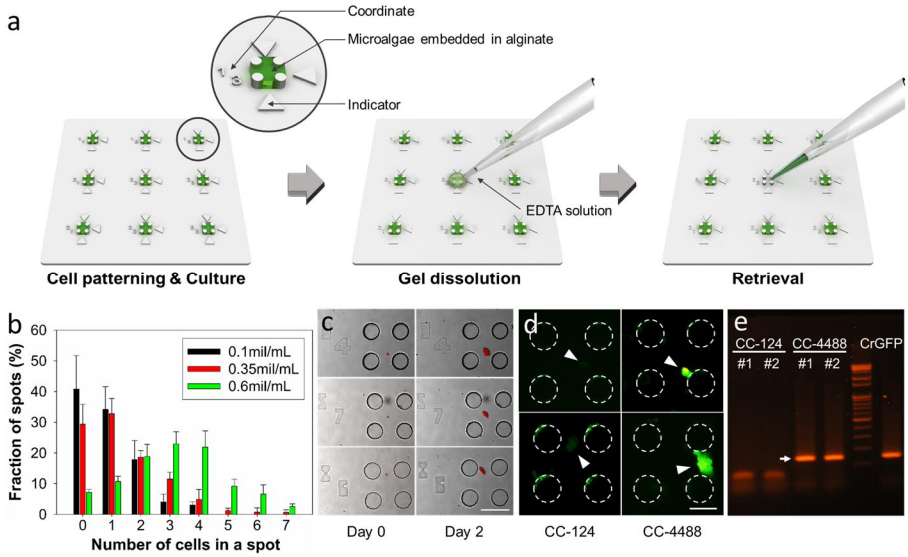

Figure 2.8. Single-cell patterning and retrieval platform. (a) The schematic process of retrieval of a single colony. The platform contains x- and y-coordinates and position indicators to provide precise positions of samples. C. reinhardtii samples embedded in alginate gel were cultured for two days, and the samples of interest were retrieved by gel dissolution using an EDTA solution by simple pipetting. (b) Distribution of captured cells in a single patterning spot according to various cell concentrations. (c) Microscopic images of single microalgae samples captured in single patterning areas (red: autofluorescence of a chloroplast, scale bar: 200 μm). (d) Fluorescence images of the wild-type (CC-124) and mutant strains (CC-4488) after two days of cultivation (scale bar: 100 μm). (e) Verification of the absence of cross-contamination during the retrieval process through gene amplification and electrophoresis. The arrow indicates a GFP gene with a length of 148 bp.

2.3.5. Sequential patterning for co-culture in 3D microenvironment

In our body, cells lie in cellular microenvironment composed of multiple cell types, extracellular matrix (ECM), and soluble factors. To understand the interactions between the composition, there have been a number of trials to control the cellular microenvironment (*77-79*). Spatially defined co-culture platforms using soft lithograph (*80-82*), negative dielectrophoresis (n-DEP) (*83*), and selective cell adhesion to ECM (*84*) were introduced, however, they remained in 2D culture or monolayer culture on ECM. Recently, as the importance of 3D microenvironment is emphasized in *in vitro* cell culture (*85*), 3D co-culture platforms were also developed such as microfluidic chip enabling hydrogel confinement (*86*) and hydrogel directed assembly (*87*). The microfluidic chip for 3D co-culture successfully patterns hydrogels with different type of cells, respectively, but further studies by retrieving the cells are challenging. The hydrogel assembly is soaked in medium so that it is difficult to observe a target assembly and two times of UV exposure for aggregation lower the cell viability. In this chapter, we are introducing a 3D co-culture platform on open surface.

Owing to the open surface, a shell-shaped liquid is patternable,

which was impossible in our previous research, microstructure mediated liquid patterning in microchannels (*88*). Figure 2.9 shows schematic process of sequential patterning using a shell-shaped liquid pattern. Pillars are arrayed to form two doughnut-shaped patterns when the liquid is swept over structures. By patterning the doughnut-shaped areas with a hydrogel, the inner area becomes another patterning area guided by walls of hydrogel. We demonstrated the reconstitution of an *in vitro* vascular network on a designed surface. Fibrinogen solutions with HUVECs was swept first to divide the inner areas into two loading zones. The core was filled with acellular fibrin matrix so that the vasculature, developed from the ECs in the inner doughnut-shaped area, can sprout into the core. The other space guided by the two fibrin walls was filled with fibrin matrix containing LFs. After five days of cultivation, the HUVECs grew, forming vascular networks with the designed shape.

This 3D microenvironment with high aspect ratio provides enough space for ECs to grow into tubular vessel network. This spatial patterning of ECs and stromal cells enables self-formation of 3D vessel network, which is difficult to accomplish in 2D platforms. Furthermore, the vessel network was formed on an open surface in contrast to on-chip vasculogenesis.[55] Thus, it is expected to enhance accessibility to samples

for further biomolecular analyses, such as western blotting. We also expect this multi-layer patterning tool can also be used for a cancer angiogenesis platform if adding cancer cells in fibrin matrix loaded in the core.

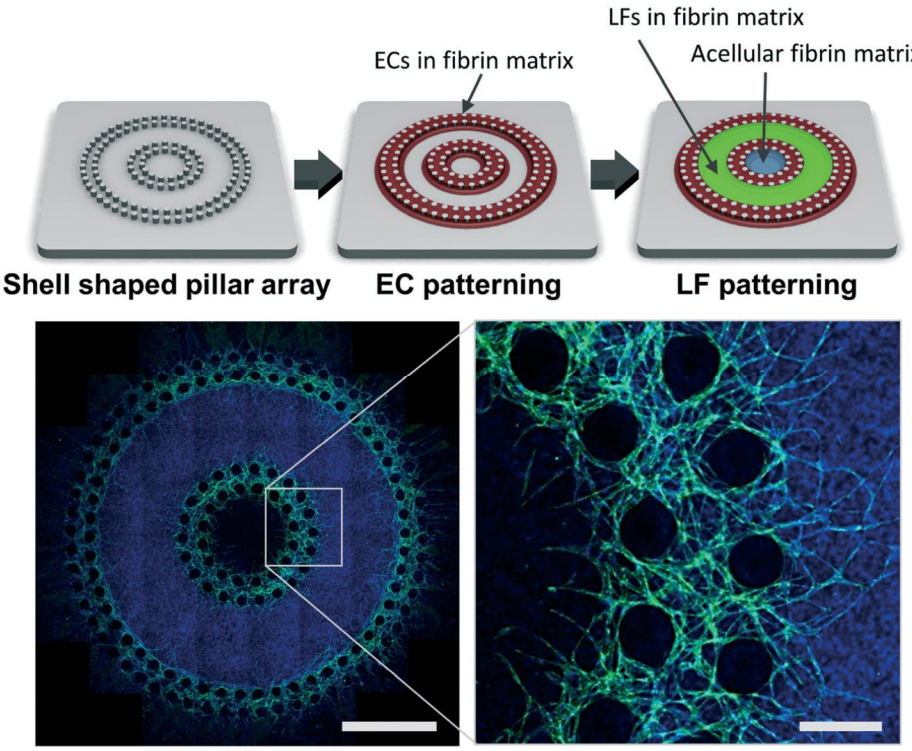

Figure 2.9. In vitro model of vasculogenesis. Endothelial cells (ECs) and lung fibroblasts (LFs) mixed with fibrinogen solution were patterned sequentially. A fibrin matrix containing ECs was initially trapped in two doughnut-shaped regions through a single sweeping motion and a fibrin matrix containing LFs was loaded into the area between the formerly patterned hydrogels. Acellular fibrinogen solution was loaded into the core region. The ECs formed vessel networks after five days of culture. Scale bar: 2 mm (left), 300 μm (right).

2.4. Conclusions

In summary, we have developed a novel liquid-patterning technique using a simple sweeping motion over a microstructured PS substrate. When the microstructures are strategically positioned on a flat substrate, a swept bulk drop over the surface leaves small droplets inside the areas cornered by the microstructures. Due to the niches between the structures, liquid can infiltrate into the structures with high aspect ratios without surface modifications. We demonstrated a single-cell screening platform and a 3D co-culture platform with capabilities of controlling the shape and volume of patterned liquids. This multi-scale liquid-patterning technique can be used for cell-based high-throughput screening and for other biological experiments.

Chapter 3. Aspiration-mediated microliquid patterning using rail-based open microfluidics

3.1. Introduction

Proper understanding of interactions between various cell types is essential in tissue engineering and design of in vitro organ models (*77, 89*). Microfluidic co-culture platforms embedding multiple cell types suspended in hydrogels can recapitulate specific organ functions and thus provide insights into complex physiological systems (*90, 91*). Microstructures within these platforms facilitate the arrangement of cells into physiologically relevant layouts (*92*). For example, porous membranes may provide permeable scaffolding to reconstitute cellular interfaces, such as the alveolar-capillary interface and the gut microenvironment (*8, 11*). Micropillars or bumps can mediate meniscus-pinning for precisely segregating co-cultures in hydrogels to model vasculature (*93*), blood-brain-barrier (*94, 95*), tumor extravasation dynamics (*96*), and glomerular filtration barrier (*20*). Ease of studying responses to mechanical and chemical stimuli using various laboratory imaging instruments complement the broad application space of these

culture systems.

Selective patterning of cell-loaded hydrogels commonly guides the gel into the desired area either by confining with surrounding pillar structures (*8, 11, 20, 93-96*) or by spontaneous capillary wicking in wettable channels (*26, 97-102*). The hydrogel loading guided by surrounding microstructures and wettability patterns fails when the hydrogel pressure exceeds a limit, or capillary-bursting pressure, causing the gel to invade the undesired region (*9, 23*). Thus, a great care should be taken to limit the injection pressure, resulting in yield variation depending on the operator's pipetting skill and low throughput associated with short available time of hydrogel precursor (*21*). Furthermore, the complex microscale features of such devices, achieved typically through soft lithography, preclude application of scalable manufacturing processes like injection molding (*21, 22*). Open microfluidic devices that utilize spontaneous capillary flow along rail structures present an alternative avenue for gel patterning without relying on the capillary-burst valve (*26, 97-102*). Here, rails denote long hydrophilic plates between which liquids are confined owing to capillary forces, while the side areas are exposed to surrounding fluids (*101*). In general, the air-liquid interfaces in rail-based microfluidics are highly

sensitive to the volume of liquid dispensed, thus making it difficult to accurately locate boundaries of patterned cell-laden hydrogels (*102*).

We here introduce a novel hydrogel micropatterning technology, which yields agile, easy and accurate formation of hydrogel patterns with only a simple pipetting activity, aspiration. The scheme relies on the capillary holding capacity of rail-based microstructures against aspiration upon their geometry, which can be tailored to leave hydrogel precisely in desired location. Although delineated below in detail, the working principle is based on the dynamic characteristics of a solid-liquid-gas contact line that it starts to recede when the local contact angle gets smaller than the critical receding angle. By defining where the recession starts and stop with geometric parameters like aspiration port diameter and rail height, we can selectively remove hydrogel from undesired regions. Experiments using simplified structures confirm theoretical design rules. Proper design provides control over the sequence of microchannel formation, which enables the formation of multiple discrete channels with a single aspiration. A proof-of-concept device featuring four microchannels separated by hydrogel structures is shown to be able to co-culture five distinct cell types. Our rail-based open microfluidic devices are amenable to fabrication by injection

molding, thereby suggesting their great potential as an easy-to-use co-culture platform with low cost and high manufacturing scalability.

3.2. Materials and Methods

3.2.1. Fabrication of open microfluidic devices

Digital light projector (DLP) 3D Printing (perfactory mini 4, EnvisionTEC) produced the bodies of open microfluidic devices with a photo curable resin (PIC100, EnvisionTEC). Rinsing with isopropyl alcohol in an ultrasonic cleaner for 15 min followed by curing ultraviolet curing (1500 W, 2 min) thoroughly solidified the printed pieces. Vapor deposition of parylene (LAVIDA, Femto science) onto the 3D printed parts ensured device biocompatibility. Attaching the bottom side of the printed part to a pressure sensitive adhesive (PSA) film completed the open microfluidic devices. Air plasma treatment of the device (70 W, 3 min) prior to fluid injection imparted hydrophilicity to the device surface for facilitating patterning of fluids under rail structures.

3.2.2. Cell culture

Cell culture experiments utilized human umbilical vein endothelial

cells (HUVEC, Lonza) cultured to passages between 4 and 7 in endothelial growth medium (EGM-2, Lonza), and normal human lung fibroblasts (LF, Lonza) cultured up to passage 7 in fibroblast growth medium (FGM-2, Lonza). CCD-18Co, HepG2, U87MG and H1299 cells were cultured in RPMI 1640 (Thermo Fisher) supplemented with 10% of FBS, penicillin (100U/ml) and streptomycin (100U/ml). 0.25% trypsin–EDTA (HyClone) facilitated detachment of cultured cells from the culture dishes. Re-suspension with appropriate amounts of culture medium provided target cell densities before mixing the cell suspension with bovine fibrinogen solutions in ratios of 3:1.

3.2.3. Hydrogel micropatterning

3D printed rail structures consisted of HRs surrounded by LRs. HRs housed holes that served as ports for injection of fluids and air infiltration. Injection of fluid via a micropipette through a port in the HR and immediate aspiration generated micropatterned fluid under LRs. Subsequent cross-linking of the solution resulted in patterned hydrogels and adjacent microchannels. Visualization of the patterns employed a solution of bovine fibrinogen (5 mg/ml, Sigma) dissolved in water and mixed with green food dye. Mixing with 25 U/ml of thrombin (Sigma)

solution in a 30:1 ratio (v/v) at room temperature began the polymerization reaction of fibrinogen to fibrin. Exposing the loaded device to ambient conditions for 5 min resulted in fully crosslinked green dyed fibrin gel.

For microfluidic co-cultures, fibrinogen solution (10 mg/ml) mixed with cell suspension in ratios of 1:3 (v/v) yielded cellular gels with a final fibrinogen concentration of 2.5 mg/ml. Mixing with thrombin solution (25 U/ml) in a 50:1 ratio immediately before injection into the fluid ports began the polymerization reaction. Immediate patterning and incubation in a cell incubator (37°C, 5% of CO_2, 3 min) resulted in fully crosslinked fibrin gel encapsulating cells. Culture of the cellular gels involved adding EGM-2 into each well of the device, followed by incubation for five days with media changes every two days.

3.2.4. Image analysis

A digital microscope (AM4115TW, Dino-Lite) captured time-lapse images of microchannel formation and images of various microchannel designs. Image analysis using ImageJ of 3D printed bodies provided measured diameters of fluid ports. Labeling of HUVECs with a mouse monoclonal antibody specific for human CD31 (AlexaFluor®488

conjugated, BioLegend) following supplier's instruction allowed comparison of vasculogenic capacities of various cell types. Confocal microscopy (A1, Nikon) imaged labeled samples through optical z-sectioning (100 and 5 μm in depth and interval, respectively). Image analysis for vascularized area measurement utilized Z-projection and conversion to binary images using auto threshold in Fiji following the "Li" method.

3.3. Results

3.3.1. Microstructures for aspiration-mediated patterning

Our rail-based open microfluidic platform consists of a 3D printed structure of photo curable resin having rails of different heights to retain liquid with different strengths and surrounding walls, which is bonded to an underlying pressure sensitive adhesive (PSA) film (Figure 3.1a). The length of the rail, l, is 5 mm, and the width of low and high rail, w_l and w_h, is uniformly 1 mm. The heights of low and high rails are respectively h=100 mm and H=300 mm. Two through-holes at the ends of a high rail function as fluid ports for liquid injection and aspiration. Air plasma treatment activates the surface of the device by increasing hydrophilicity.

Figure 3.1b illustrates the basic working principle of the novel patterning process of hydrogel, which allows us to form hollow microchannels surrounded by precisely defined hydrogel patterns. We first inject a hydrogel precursor solution through one of the fluid ports, which fills the area under all rails and runs along the corner of the wells (the second column of Figure 3.1b). Upon aspiring through the open port, the liquid is sucked into the pipette only from the region below high rail, while the low rail strongly retains the liquid (the third column of Figure 3.1b). The result is the hollow microchannel defined by the empty region under the high rail with the hydrogel remained pinned by the low rail (the fourth column of Figure 3.1c). In the following, we delineate the physical principle behind this selective removal and controlled pinning of hydrogel patterns, which leads to various hygrogel-based channel structures and facile fabrication of cell co-culture systems.

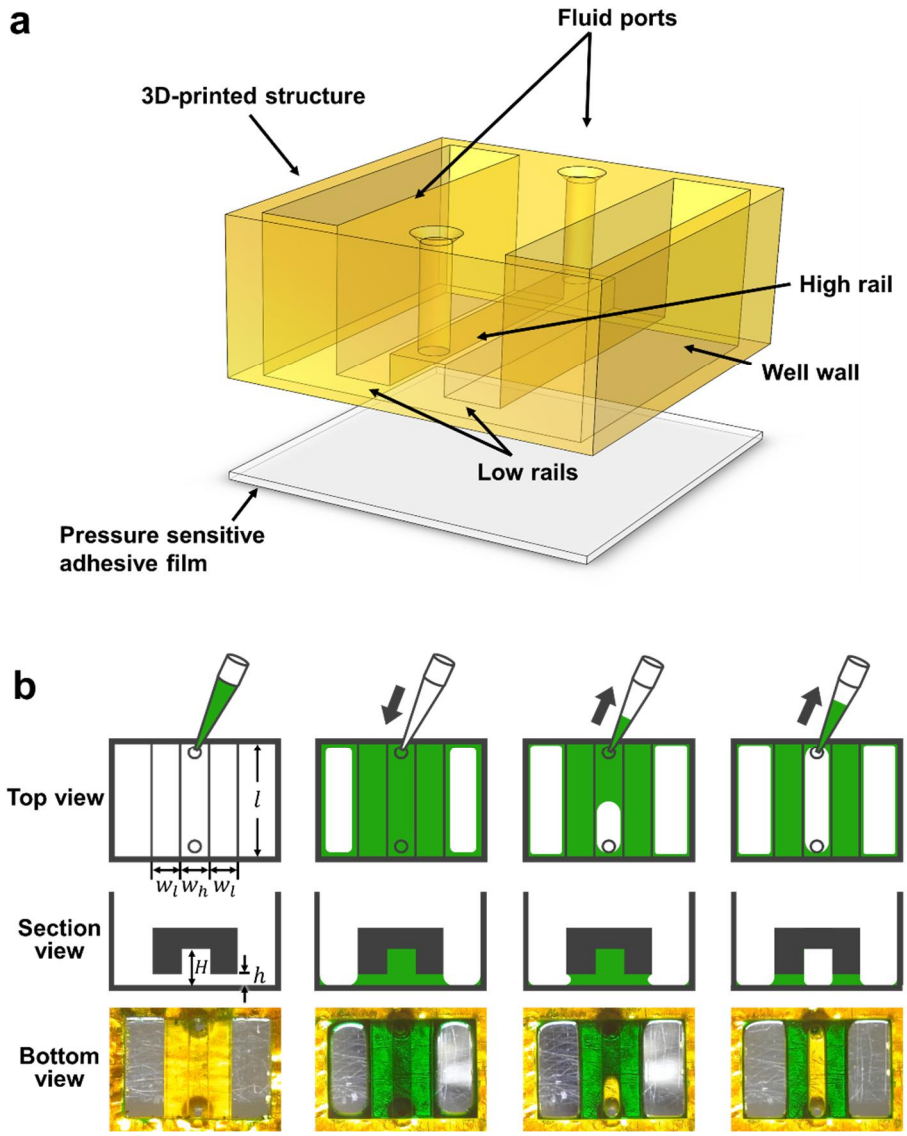

Figure 3.1. (a) Schematic exploded view of a rail-based open microfluidic device, which is designed to yield a single channel beneath the high rail. (b) Illustration of steps in the aspiration-mediated microchannel formation process. The bottom row features optical images taken through the clear PSA film from the underside of the device during filling and aspirating green dyed water.

3.3.2. Theoretical analysis of microchannel formation

As the pressure at an open port is lowered by aspiration with a micropipette, the interior pressure of the hydrogel is also lowered. The Young-Laplace equation states that the liquid-gas interface of the hydrogel originally filling the gaps caves inward, Figure 3.2, due to the pressure difference between the atmosphere (p_a) and the liquid (p_l): $\Delta p = p_a - p_l = \gamma\kappa$, where γ is the gas-liquid interfacial tension and κ is the interface curvature. The contact line where the gas-liquid interface meets the solid surface is initially immobile while resisting the pulling force because it can recede only when the contact angle is reduced below the critical receding contact angle, $\theta_{R,c}$ (*103*). We experimentally found that $\theta_{R,c}$ is nearly zero for hydrogel on the hydrophilized 3D printed part of resin and PSA film surfaces. The patterning of hydrogel that originally fills the gaps under both high rails (HRs) and low rails (LRs) critically depends on where the interface starts to recede first by reaching $\theta_{R,c}$.

For the initially hydrogel-loaded configuration, the liquid-gas interfaces arise at the open port and the side areas of liquid beneath LRs. For the open port of diameter D, the maximum pressure difference that the interface can withstand before the contact angle on the inner wall of

HRs reaches zero, Δp_o, corresponds to the pressure difference for a hemispherical interface with the maximum curvature of $4/D$: $\Delta p_o = 4\gamma/D$. The capillary pressure at the interface beneath LRs is given by $\Delta p = \gamma(2\cos\theta/h + 1/\eta)$, where θ is the instantaneous contact angle of liquid, and η is the radius of curvature on a plane parallel to the substrate. As η is scaled as l, the length of rails, we get $h \ll l$, which allows us to estimate the maximum pressure difference for the side area below LRs as $\Delta p_{\mathrm{L}} = 2\gamma/h$.

If $\Delta p_o < \Delta p_{\mathrm{L}}$, the critical liquid pressure for interface recession is reached at the open port before the side area. Once burst at the open port, the interface spontaneously bulges accompanying the decrease of interface curvature to meet the bottom substrate. Then the interface curvature is newly defined by the height (H) and width (w_H) of HR. The critical capillary pressure that can induce interface recession beneath HRs is given by $\Delta p_{\mathrm{H}} = 2\gamma(1/w_{\mathrm{H}} + 1/H)$. If $\Delta p_o > \Delta p_{\mathrm{H}}$, the liquid pressure is already low enough to ensure continuous recession of the liquid beneath HR. If $\Delta p_o < \Delta p_{\mathrm{H}} < \Delta p_{\mathrm{L}}$, further decrease of the liquid pressure upon bursting of the open port can cause the liquid to recede along a lane beneath HR. The liquid will stop upon bursting at the open port and recede beneath LRs, rather than HRs, if $\Delta p_{\mathrm{H}} > \Delta p_{\mathrm{L}}$.

Figure 3.3 displays the experimental results of hydrogel patterning for different geometries of microdevices. In the left column, Δp_{L} is greater than both Δp_o and Δp_{H}, and thus the interface recession occurs from the open port, continues beneath HR, to result in a straight empty lane flanked by the hydrogel beneath LR. In the middle column, the side areas beneath LRs burst before the open port because $\Delta p_{\mathrm{L}} < \Delta p_o$. In the right column, the open port bursts first because $\Delta p_{\mathrm{L}} > \Delta p_o$, but further decrease of the liquid pressure bursts the side areas beneath LRs before the interface from the open port starts to recede beneath HR.

Figure 3.4 displays the experimental results of microchannel formation as a function of the geometry of device, such as the port diameter and the heights of low and high rails. In Figure 3.4a, we can predict where the interface recession onsets upon aspiration, whose criterion is given by $\Delta P_L = \Delta P_o$, or $D = 2h$. For $D > 2h$, we get $\Delta P_L > \Delta P_o$, and thus the port bursts first, leading to successful channel formation in the beginning. Otherwise, the interface moves at the side area of LR before at the port, preventing the formation of the microchannel under HR. Figure 3.4b gives the condition of the height of HR to ensure that the interface formed from the open port keeps receding while the interface beneath LR remains pinned. The corresponding boundary is

given by $\Delta P_L = \Delta P_H$, or $H = h/(1-h)$. For $H > h/(1-h)$, we get $\Delta P_L > \Delta P_H$, leading to continuous recession of the interface from the open port. Otherwise, the interface under LR starts to recede, eventually merging with the interface originated from the open port. We see that our experimental results agree well with the theoretical predictions in Figure 3.4.

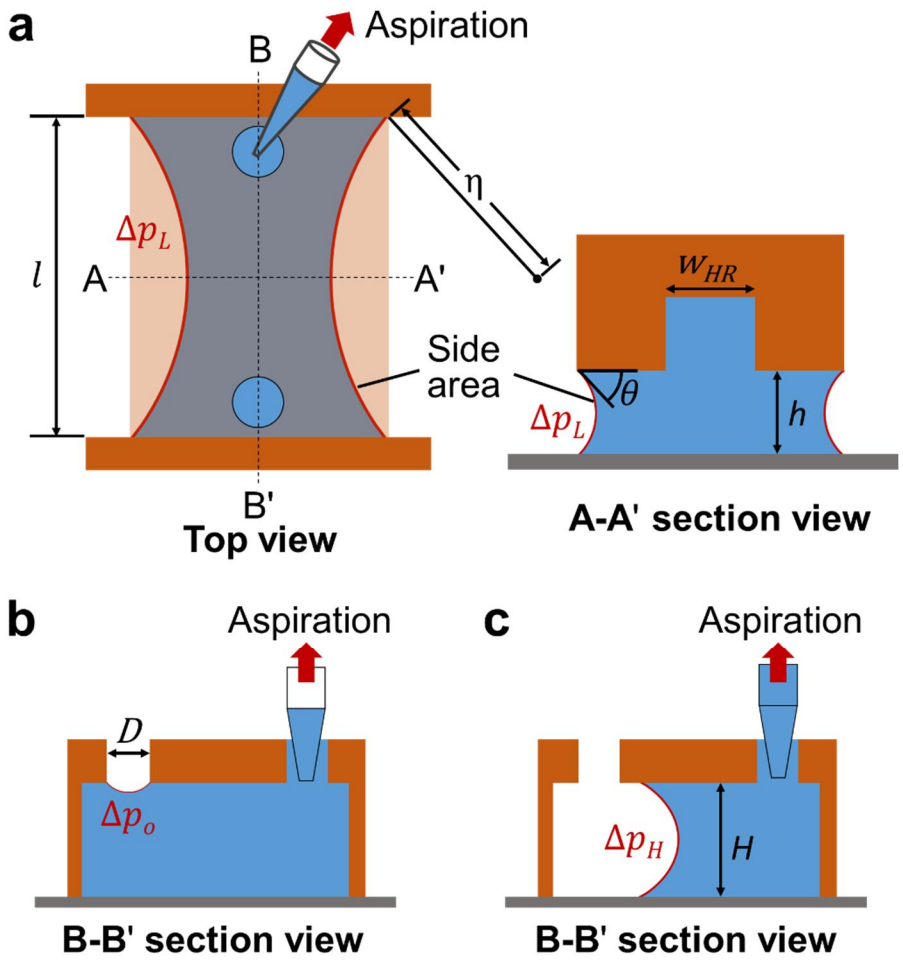

Figure 3.2. Schematic diagrams indicating key device dimensions and the Laplace pressures of menisci (a) immediately after aspiration, (b) as the port interface deforms, and (c) as the receding interface travels along HR.

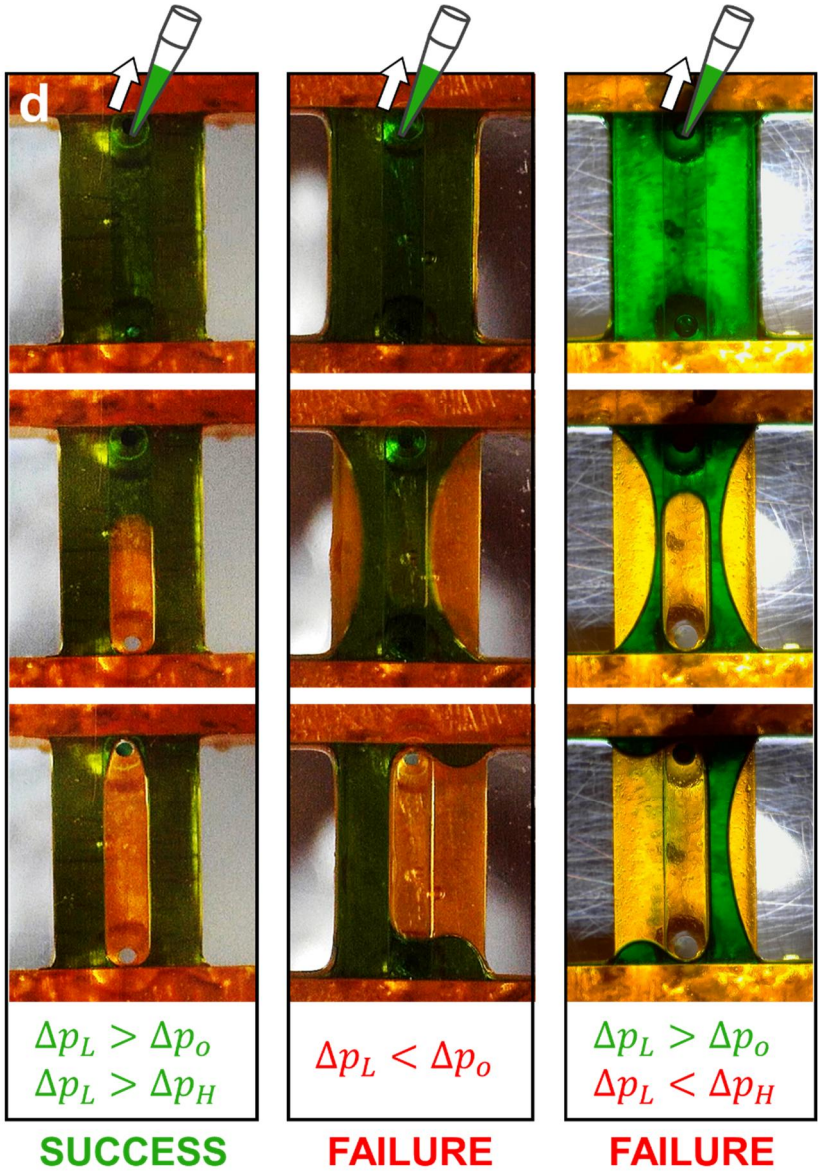

Figure 3.3. Meniscus dynamics during aspiration under three different combinations of critical capillary pressures. The dimensions of the structures are such that [*H*, *h*, *D*]=[300, 100, 300] μm, (Left column), [300, 200, 300] μm (middle column), [200, 175, 500] μm (Right column). Lengths and widths of all rails are fixed as 5 and 1 mm, respectively.

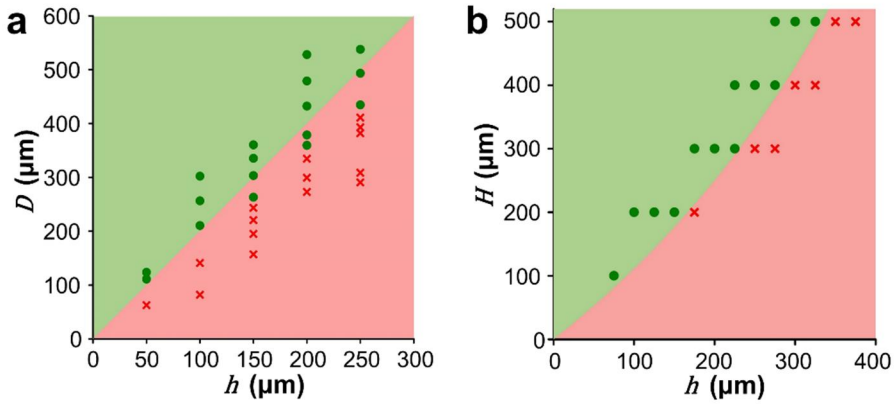

Figure 3.4. (a) Plots of the effects of port diameter and LR height on bursting at the open port. (b) Plots of the effects of HR height and LR height on formation of microchannel. Shaded regions demarcate dimensions suitable (green) and unsuitable (red) for microchannel formation based on the theoretical calculations. Markers indicate successful (green) and unsuccessful (red) microchannel formation in experiments. Lengths and widths of all rails are fixed as 5 and 1 mm, respectively.

3.3.3. Formation of multiple discrete microchannels

Studies of fluid dynamics under the basic rail structure verify that the air-liquid interface with the smallest critical capillary pressure tends to move first along the rail. Leveraging this phenomenon can provide control over the sequential formation of discrete microchannels with a single aspiration. Figure 3.5 and 3.6 exemplify multiple channel formation using various critical capillary pressures at air-liquid interface pinned at holes. In this device, a rectangular LR, 75 μm from the underlying PSA film surrounds 'S', 'N', and 'U' shaped HRs, 300 μm apart from PSA. The diameter of fluid ports decreases in the order of S1 to U1 as listed in the table in Figure 3.5 while U2 has the largest port diameter. When aspirating dyed water filling under the rail structure from the port labeled 'U2', the air-liquid interface at the largest opposing port (S1) begins traveling along the rail to form an 'S' shaped microchannel (the second panel of Figure 3.3b). As the suction continues at U2, the air-liquid interface at the next largest port (N1) now begins to recede (the third panel of Figure 3.3b). Consequently, microchannels with shapes of 'S', 'N', and 'U' form via a single aspiration process through one port as shown in Figure 3.5.

During multiple channel formation, differences in port diameter

within the same channel lead to orderly movement of the air-liquid interface. If ports of the same diameters are employed, air can infiltrate into the channel through the identical ports simultaneously, to form a thin film of liquid between the infiltrating air from the two ports, as shown in Figure 3.7. Breaking the thin film to form a continuous microchannel requires additional pressure drop since foam films have larger Laplace pressures than droplets of equal curvature, owing to the presence of two air-liquid interfaces (*103*). In the video, a continuous microchannel forms in the top right HR because it contains the port of aspiration, and thus only a single port for air infiltration. In contrast, a similar device employing asymmetrical port sizes in each HR exhibits unidirectional movement of air-liquid interfaces beneath HRs as shown in Figure 3.8.

This unique liquid patterning technique enables versatile rendering of microchannel in hydrogels. Figure 3.9a and b show devices with multiple hydrogel channels arranged in parallel lines and a lattice of squares, respectively. Figure 3.9c and d respectively highlight the ability of our scheme to generate a single circular and two concentric channels. We note that the circular designs can facilitate investigation of radial interaction between patterned cells as described earlier (*104*).

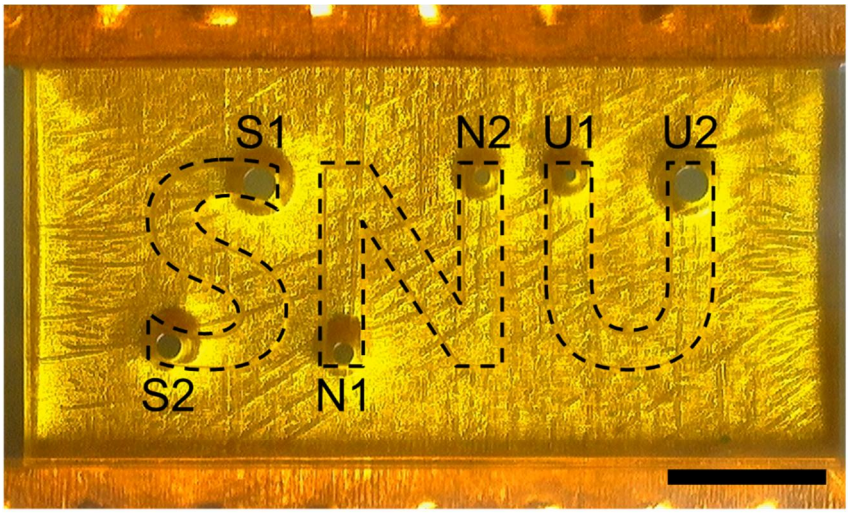

Port	Diameter (μm)	Port	Diameter (μm)
S1	400	S2	300
N1	250	N2	190
U1	140	U2	420

Figure 3.5. An open microfluidic model for rendering multiple discrete microchannels using different port sizes. An image of the underside of a device with three HRs in the shapes of 'S', 'N', and 'U', surrounded by a rectangular LR (scale bar: 2 mm). Loading and aspiration occur through port U2. Opposing port sizes decrease from S1 to U1 as indicated in the bottom table.

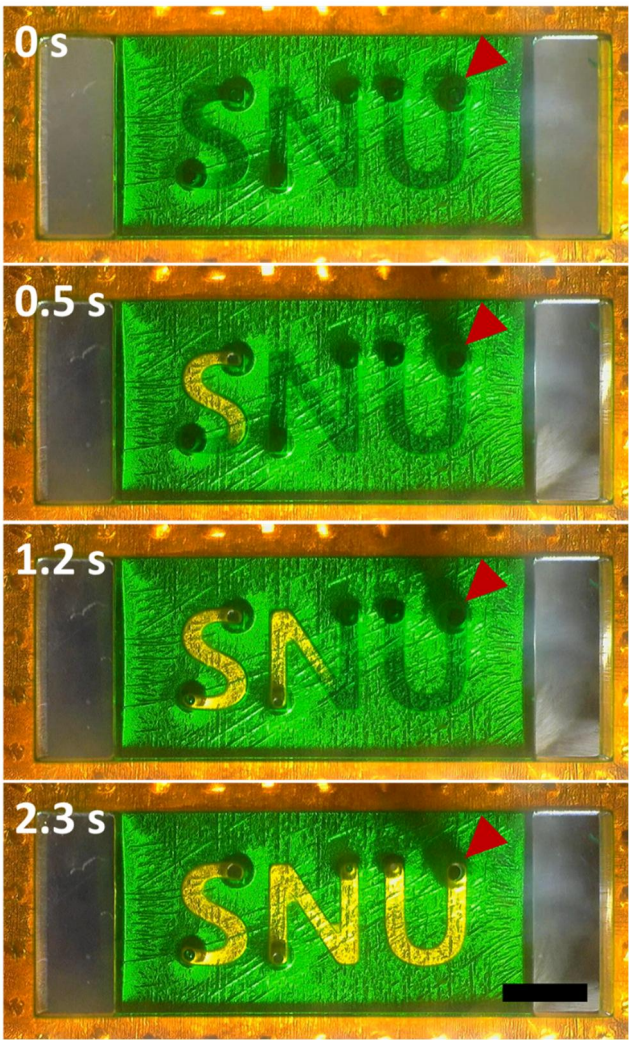

Figure 3.6. Sequential snapshots (top to bottom) viewed from the bottom of the device during aspiration. Air-liquid interfaces preferentially advance from the largest port to the smallest port. Red arrows indicate the aspirating port, U2. (Scale bar: 2 mm)

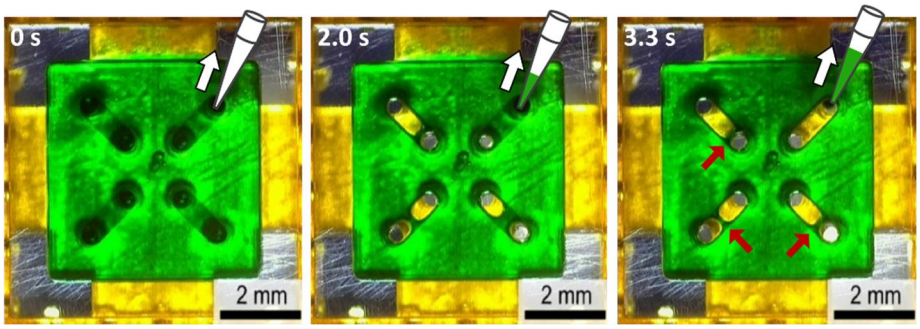

Figure 3.7. Sequential snapshots viewed from the bottom of a square-shaped device during aspiration. Air-liquid interfaces at both holes connected with a single channel burst into the area under HRs due to the identical hole size, resulting in thin film formation of liquid. Arrows indicate the thin film of liquid.

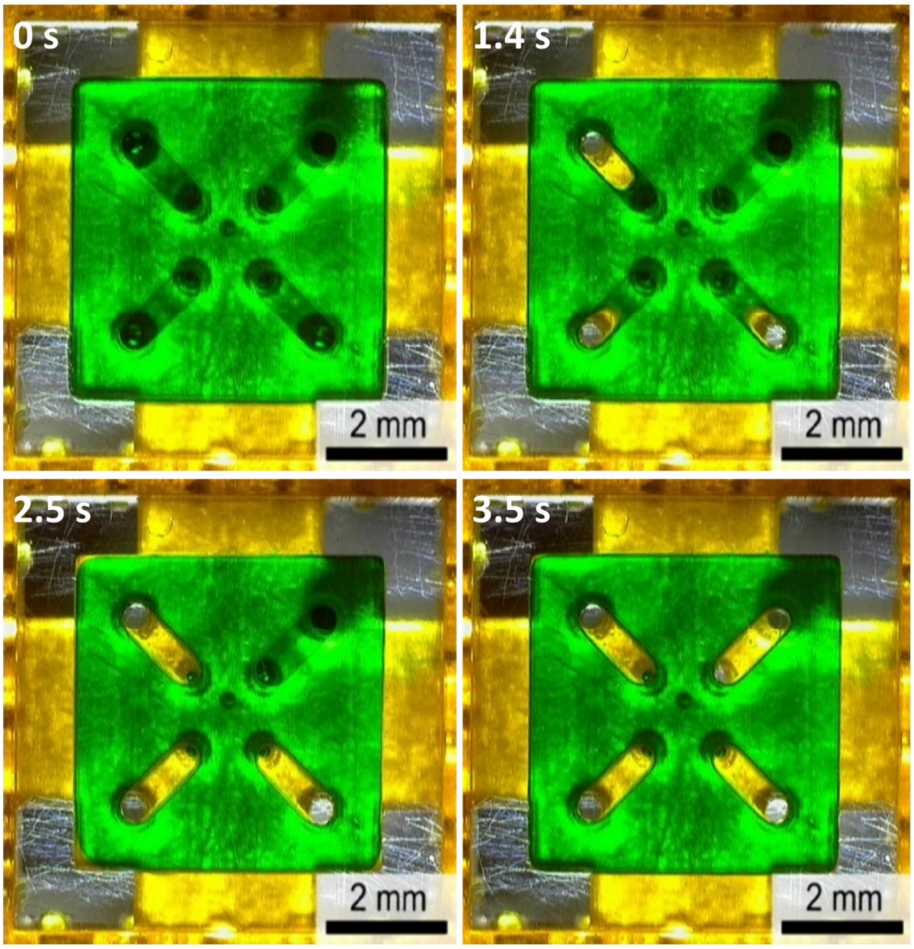

Figure 3.8. Sequential snapshots viewed from the bottom of a square-shaped device during aspiration. Air-liquid interfaces pinned at larger holes burst into the area under HRs, resulting in unidirectional movement of interfaces, resulting in formation of four channels.

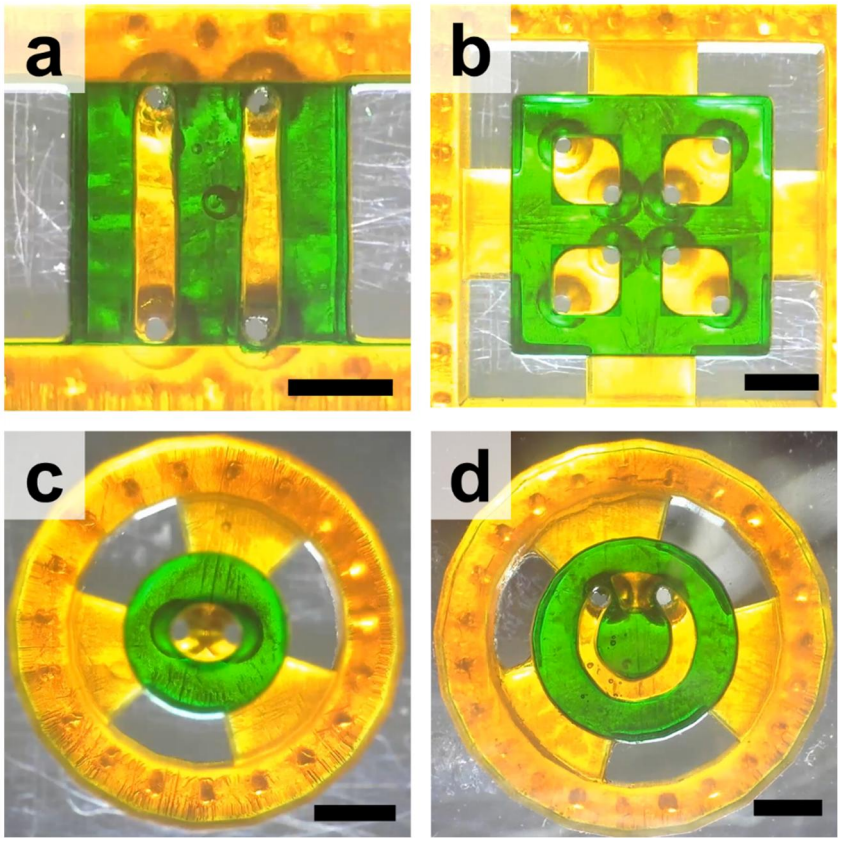

Figure 3.9. Bottom view images of devices with multiple green hydrogel channels organized into (a) parallel lines, (b) a square lattice, (c) a circle, and (d) concentric circles. Scale bar, 2 mm.

3.3.4. An application for screening vasculogenic capacities

Modification of the device in Figure 3.9b provides a platform for convenient and effective comparison of paracrine signaling induced by co-culture of five cell types. Here, the microfluidic device contains four linear HRs surrounded by a square LR (Figure 3.10a and b). Four support structures suspend the rail structures by connecting them to the well walls, which form growth medium reservoirs when bonded to a PSA film. Patterning of a fibrin hydrogel (2.5 mg/ml) containing a mixture of human umbilical vein endothelial cells (HUVEC, 4 x 10^6 cells/ml) and lung fibroblasts (LFs, 1 x 10^6 cells/ml) under the LR, and subsequent seeding of gels containing different cell types into the rendered microchannels establishes the basic experimental setup. The present studies involve eleven devices with channels containing different combinations of LFs, colon fibroblast cell line (CCD-18Co), liver cancer cell line (HepG2), glioblastoma cell line (U87MG), and lung carcinoma cell line (H1299). All gels contain cell concentrations of 5 x 10^6 cells/ml except for an acellular fibrin gel as a control. Figure 3.11a presents a confocal image of an exemplary device taken after 5 days of cultivation. Regions of interest (ROI) measuring 1 x 1.8 mm^2 in area, which is located around each HR, encompass the interfaces between the HUVEC-

LF gel and the gels containing cells of interest. Analysis of z-projected confocal images yield quantification of the vasculogenic capacities of the cells of interest (Figure 3.11 and 3.12). In alignment with previous studies (*93, 100, 105*), LFs vigorously promote formation of vasculature. Furthermore, acellular gels and gels containing LFs exhibit angiogenic sprouting into the channels. On the other hand, U87MG and H1299 gels inhibit the growth of surrounding vessels and do not provoke cancer angiogenesis. Gels containing CCD-18Co and HepG2 show no significant difference in vasculogenic capacity compared against the acellular matrix. The results of these tests corroborate the ability of the platform for screening candidates for cancer angiogenesis in vitro. Furthermore, the versatility of the channel rendering method supports facile device adaptation to study a broad range of paracrine signaling cues in various conformations.

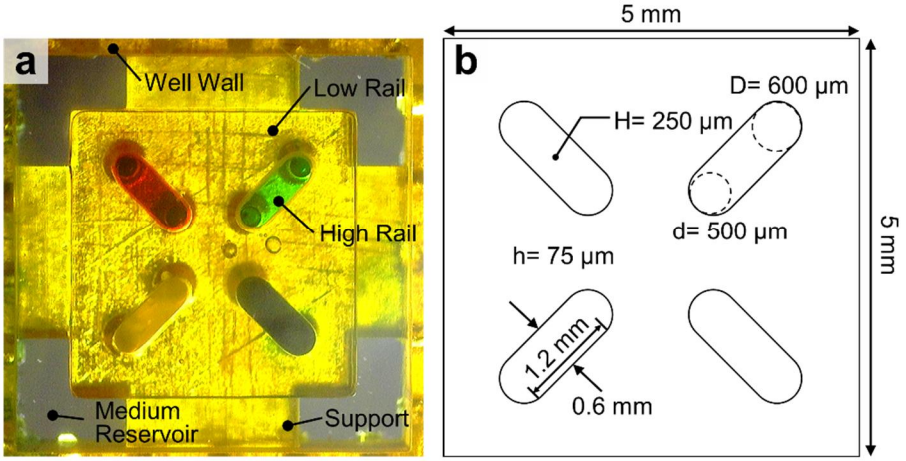

Figure 3.10. An open microfluidic design of multiple channel rendering for screening vasculogenic capacities of multiple cell types. (a) Bottom view image of microfluidic device with four channels and a square shaped LR. (b) Illustration of device dimensions.

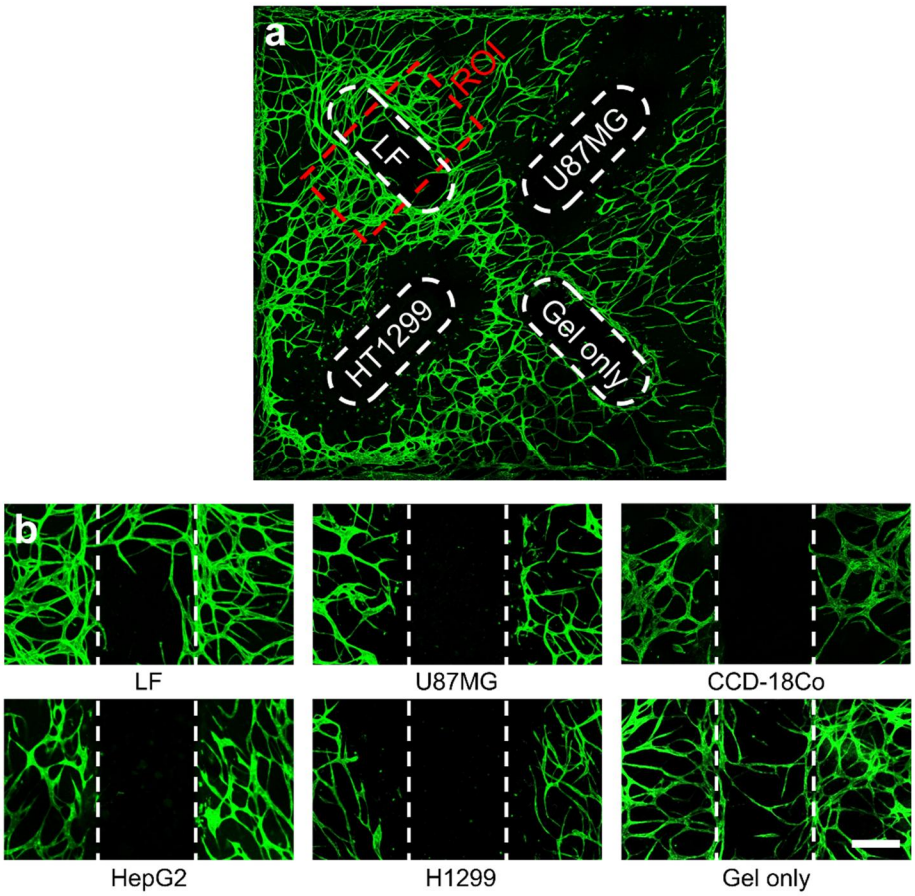

Figure 3.11. Confocal fluorescence images of the vasculogenic co-culture model showing CD31 labeled HUVECs with green fluorescence. (a) A confocal image displaying vessel network under the whole culturing area under rail structure. Red dashed box delineates an example region of interest (ROI). (b) Representative confocal micrographs of ROIs in channels containing different cell types. Scale bar, 300 μm.

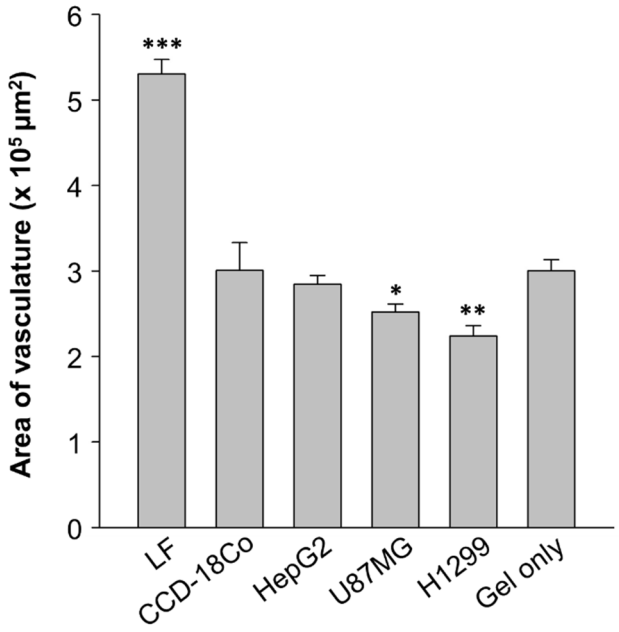

Figure 3.12. Plot of vascularized area within the ROIs for each cell line. Statistical significances (*$p < 0.05$, **$p < 0.01$, and ***$p < 0.001$) result from unpaired two-tailed Student's t-tests for comparison with the 'Gel only' condition.

3.4. Conclusions

The reported hydrogel patterning method based on interfacial capillary dynamics and associated device design strategies form the foundation of a new class of aspiration-mediated open microfluidic devices featuring versatile designs and simple operation. The rail structures in these devices, composed of different heights of rails with embedded fluid ports, embody varying critical capillary pressures at each air-liquid interface. Systematic studies corroborated by theoretical models reveal fundamental design rules based on the relationships between geometric parameters of these structures and the capillary pressures. Leveraging these insights serves the development of devices where aspiration selectively removes injected hydrogel precursor beneath high rails to leave behind precisely rendered microchannels. Furthermore, this concept extends to the generation of multiple discrete channels via aspiration from a single fluid port, enabling a wide range of patterning designs with simple fabrication. A demonstrated high-throughput co-culture model for assessing vasculogenic capacities of multiple cell types highlights the practical applications of the multiple channel formation method.

These rail-based microfluidic devices allow simple and robust

patterning based on aspiration, dramatically enhancing experimental throughput and mitigating users' error faced by conventional approaches. When using hydrogel as ECM, simplified patterning process increases the number of samples obtained from a single mixture of hydrogel precursor during cross-linking. The shortened patterning time can also enhance uniformity in properties of hydrogels between samples. Furthermore, the simple geometries of the rail structure are compatible with scalable manufacturing techniques such as injection molding. The enhanced experimental throughput and productivity offered by the outlined strategies can contribute to new high-throughput screening models and accelerate commercialization of microfluidic cell culture models.

Chapter 4. High-throughput microfluidic 3D cytotoxicity assay for cancer immunotherapy

4.1. Introduction

Adoptive transfer of *ex vivo* cultured/engineered cytotoxic lymphocytes (CLs) is arising as a promising approach to treat cancers (*106*). In particular, T cells expressing chimeric antigen receptor (or CAR-T cells) have been extremely successful in the treatment of CD19 expressing leukemia and lymphoma (*107-109*). The success has led to FDA approval of two CAR-T cell-based therapies, Kymriah (Novartis) and Yescarta (Gilead), and new CAR engineering strategies have been studied to improve the performance, reduce toxicity, and broaden applications of CAR-T therapy (*110, 111*). In addition, NK cells and γδ T cells, which exhibit low cytotoxicity and minimum graft-versus-host disease in allogeneic transfer compared with T cells, have been developed as alternatives of CAR-T cells as an off-the-shelf therapeutics. (*112, 113*) In spite of these efforts, the performance of adoptive transferred CLs against solid tumors is still limited due to complex tumor microenvironment (TME) that limit trafficking and effector functions of CLs (*114, 115*). In addition to highly immuno-suppressive

microenvironments caused by acidic and hypoxic conditions and enrichment of suppressive cells (*116-118*), fibrotic tumor stroma is an important factor limiting successes of cancer immunotherapy by acting as a physical barrier for CLs to access tumor cells (*119, 120*). Therefore, various factors comprising TME need to be considered for the development of engineered CLs for solid tumors.

Cytotoxicity assay measuring killing ability of CLs is one of the most critical assays for the development of CLs for cancer immunotherapy. Chromium or calcein release assay based on the measurement of released radioactive ^{51}Cr or fluorescence calcein from lysed cancer cells has been a standard method for assessing cell-mediated cytotoxicity (*121, 122*). These methods have been widely used because cytotoxicity can be assessed simply by co-culturing CLs with tumor cells loaded with ^{51}Cr or calcein. In addition, these assays are compatible with 96 well formats, thus can be performed in high-throughput fashions. However, in these assays, tumor cells are either adhered on flat surfaces or suspended in medium, thus complex TME in solid tumors limiting CL activity are lacking.

Microfluidic-based platforms, which allow the reconstitution of complex 3D microenvironments of human tissues in *in vitro* by

compartmentalization of multiple cell types, applying chemical and mechanical stimulations, and controlling chemical gradient (*123*), can be a powerful method for the assessment of lymphocyte cytotoxicity for solid tumors (*124*). Recently, microfluidic chips based on poly(dimethyl siloxane) (PDMS), a common material for microfluidics, were developed as preclinical models to evaluate antitumor activities of engineered T cells expressing T cell receptors specific for tumor antigens (or TCR-T cells) (*125, 126*) or engineered NK cells expressing Fc receptors (*127*) in 3D microenvironments recapitulating various aspects of TME. Specifically, microfluidic chips compartmentalized with 3D ECM gels containing tumor cells and TCR-T cell loading zones were used to assess the roles of hypoxia, inflammatory cytokines, immunosuppressive conditions induced by mTOR inhibitors, and monocytes on the cytotoxicity of TCR-T cells (*125, 126*), and microchips filled with ECM gels containing tumor cell spheroids and perfusable tubular vasculatures were used to recapitulate TME for NK cell trafficking toward solid tumors and to test combination of immuno-stimulatory biologics with NK cell therapy (*127*). However, the devices aforementioned requires labor and time intensive batch fabrication processes because the device was made of PDMS (*128*).

In this study, we introduce a 3D cytotoxicity assay using an injection molded plastic array culture (CACI-IMPACT) platform with which we can monitor both migration and cytotoxic activity of CLs in 3D microenvironment, by customizing our previous IMPACT device (*99*). We adopted extracellular matrix (ECM), which is a basic component of TME and did not exist in the standard protocols of cytotoxicity assays. ECM acted as physical barrier to restrict CLs from access cancer cells embedded in it. The limited accessibility resulted in low cytotoxicity compared with 2D assay. In addition, fibrotic ECM of TME was reconstituted by using denser collagen which lowered migration and cytotoxicity in observation of large area, but induced faster lysis process than sparser ECM. Furthermore, we improved the assay throughput compared with PDMS devices due to enhanced productivity oriented by changing material and usability mediated by rail-based microstructures. This model allowed us to test the effect of the physical properties of the 3D microenvironment on cytotoxic activity and we expect that this model can be used for high-throughput screening platform for estimating the efficacy of engineered lymphocytes in more *in vivo* like environment than conventional assays.

4.2. Materials and Methods

4.2.1. Cell culture

HeLa cells were cultured in Dulbecco's modified eagle's medium (DMEM) with 10% of fetal bovine serum (FBS) and 1% of penicillin–streptomycin (PS). NK-92 cells were cultured in minimum essential media alpha (MEM α) with 15% of FBS, 15% of horse serum (HS) and 1% of PS and other supplements, including myo-inositol (0.2 mM), 2-mercaptoethanol (0.1 mM), folic acid (0.02 mM). NK-92 cells were sub-cultured in every two days in 6 ml of the full medium and 1200 units of Interleukin-2. Sub-culture was conducted in T25 flasks with cell concentration of 10^5 cells/ml.

4.2.2. Fluorescent labeling of live and dead cells

HeLa cells were labelled with CellTrace™ CFSE Cell Proliferation Kit (Thermo fisher, C34570) by incubating the cells in serum free DMEM with 2 μM of CFSE for 30 minutes. NK-92 cells were labeled with CellTrace™ Far Red Cell Proliferation Kit (Thermo fisher, C34572) by incubating the cells in serum free MEM α with 2 μM of the reagent for 20 minutes. To detect dead cells, propidium iodide (PI) was used. For

live imaging, PI-containing medium was used from the beginning of imaging. For imaging after 24 h of NK-92/HeLa co-culture, the medium was replaced with PI-containing medium 30 min prior to imaging.

4.2.3. 3D cytotoxicity assay using gel patterned device

CFSE-labeled HeLa cells were mixed with collagen gel pre-solution, which is a mixture of rat tail oriented collagen type I (Corning, 354249) with concentration of 9 mg/ml and 150 mM HEPES buffer at 2:1 ratio (v/v). The collagen pre-solution containing HeLa cells were patterned under the low rails of a CACI-IMPACT device (Figure 4.3a) following air plasma treatment with 70W for 3 min. The device was incubated in a cell culture incubator with 37°C and 5% of CO_2 for 30 min to crosslink the collagen. The cross-linked collagen gel blocks were immersed in media and further incubated for 24 h in the cell culture incubator. NK-92 cell suspension (2×10^6 cells/ml, 2 µl) was loaded into the channel, and the device was stored in the incubator for 20 min at an angle of 90 degrees to let the NK-92 cells settle down on one side of the collagen block encapsulating HeLa cells. Then, the two medium reservoirs were filled with MEMα, and the devices were stored in the incubator for 24 h, or in a live imaging system. PI was added in the

medium, and fluorescence images were acquired to assess cytotoxicity.

4.2.4. Image analysis

Time-lapse images were acquired using an inverted microscope system (Nikon eclipse Ti-E). Endpoint images of NK-92/HeLa co-culture were acquired using a confocal microscope (Nikon Ti 2 A1) through optical z-sectioning (depth: 100 μm, interval: 4 μm). For image analysis, we used Fiji. Z-projected images were used for display and the images were converted into binary images using auto threshold ('Mean' method) in Fiji for quantitative analysis. The number of NK cells in each sub-region was estimated by dividing the total area of NK cells into the average single NK cell area. Similarly, the percentage of killed HeLa cells were estimated using HeLa cell areas. Since live HeLa cells exhibited extended morphology whereas dead HeLa cells were rounded, areas of dead HeLa cells were converted to those of equivalent number of live HeLa cells by multiplying an average ratio of single live and dead HeLa cell area. Finally, the percentage of killed HeLa cells were calculated by (converted dead HeLa cell area)/(live HeLa cell area + converted dead HeLa cell area). Five unbiased students manually selected 20 NK and HeLa cells respectively and the average areas of the

selected 100 NK and HeLa cells were used for single cell area of each cell type.

4.2.5. 2D cytotoxicity assay

CFSE-labeled HeLa cells were plated in each well of a 24 well-plate (6 x 10^4 cells/well) and cultured for 24 h. Then, various numbers of NK-92 cells were added to the well, and HeLa and NK-92 cells were co-cultured for another 24 h. PI was added to the media to have final concentration of 3 μM, and the percentage of dead HeLa cells were measured by fluorescence microscopy.

4.3. Results

4.3.1. Design and fabrication of devices

To fabricate microfluidic devices for cytotoxicity assays in 3D ECM gels, we first designed and fabricated injection molded microfluidic devices that enable facile hydrogel patterning (Figure 4.1). To efficiently observe cytotoxic activity of CLs through fluorescence microscopes equipped in typical biology labs, the device was designed to have the same dimension as a standard microscope slide (3″ x 1″), and

rail-based microstructures under which cytotoxicity assays would be conducted were embedded in 2 x 6 rectangular array of wells with the same pitches as the conventional 96 well-plate (Figure 4.1a). The rail-based microstructures for hydrogel patterning is composed of two primary patterning rails (low rail, or LR), which are 100 μm apart from the bottom surface, and one secondary patterning rail (high rail, or HR), 500 μm apart from the bottom surface (Figure 4.1b). The rail-based microstructures allowed spatially compartmented hydrogel patterning to be performed by a simple and fast patterning process (Figure 4.2). First, the surfaces of the device are hydrophilically modified via air plasma treatment. Next, hydrogel pre-solution was injected through an injection hole to fill the entire microstructures (Figure 4.2a), and subsequently aspirated away by pipetting. Due to the hydrophilicity of the surfaces, only hydrogel pre-solution underneath LR regions remained (Figure 4.2b). Importantly, this process can be performed for 12 wells in a slide within 30 s. After crosslinking the hydrogel underneath LR regions, the second solution was loaded underneath the HR region to form two separate compartments (Figure 4.2c). Compared with the PDMS devices widely used in microfluidics that requires tedious batch processes for fabrication, this injection molding-based device can substantially

enhance throughput of the assay because the devices can be massively produced. In addition, hydrophilic rail-based microstructures permit hydrogel patterning to be conducted by simple pipetting, thus entire devices can be readily fabricated without requiring any sophisticated equipment/techniques.

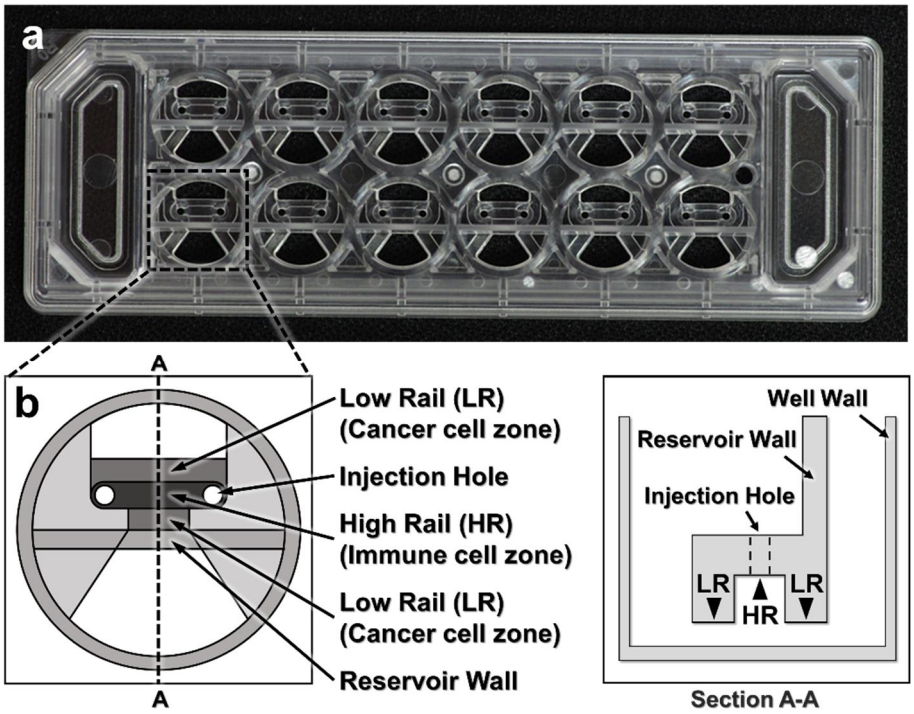

Figure 4.1. A CACI-IMPACT platform and its working process. (a) Rail-based microstructures are embedded in microwells with 96 well plate format and the structures are integrated in a 2 x 6 rectangular array. Water tanks are allocated in both sides to maintain humidity in samples. (b) Schematic top and section view of a single well. The microstructure in a single well consists of two low rails (LRs) for primary hydrogel patterning and one high rail (HR) to form a channel for secondary fluid patterning after hydrogel cross-linking.

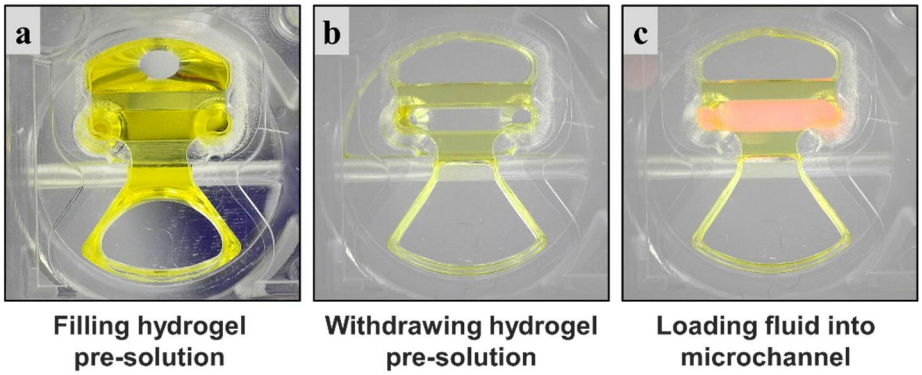

Figure 4.2. Procedure of using the device. Once a hydrogel pre-solution is filled and withdrawn through an injection hole, the solution remains only underneath LRs. When the hydrogel is cross-linked, a microfluidic channel is formed where another fluid can be loaded.

4.3.2. Cytotoxicity assay in 3D ECM environment

Using the hydrogel patterning technique, we first fabricated collagen gels encapsulating HeLa cells underneath LR regions (Figure 4.3a Day 0), and cultured for one day. Then, NK-92 cell suspension was loaded next to the collagen gel, and the device was tilted to 90o for 20 min to accumulate NK-92 cells on one side of the collagen gel by sedimentation (Figure 4.3a Day 1). NK-92 cells attached on the collagen gel surfaces penetrated into collagen gel blocks and migrated toward HeLa cells to exert cytotoxicity. Figure 4.3b shows the initial state of the assay on Day 1.

HeLa cells and NK-92 cells were labeled with two distinct fluorophores, and propidium iodide (PI), a fluorescence dye labeling dead cells, was added in the media to visualize dead cells. In this way, we can simultaneously observe NK-92 cell migration and cytotoxicity along the collagen matrix containing HeLa cells by live imaging (Figure 4.4 and 4.5). NK-92 cells uniformly deposited on collagen block at the beginning of imaging penetrated and migrated into collagen matrix as shown in time-lapse images acquired with a low magnification objective lens (Figure 4.4). As NK-92 cells propagated into collagen gels, PI-stained HeLa cells near NK-92 cells increased, meaning NK-92 cells

exerted cytotoxicity against HeLa cells in collagen gels. Detailed procedures in CL-mediated cytotoxicity of cancer cells, rounding by detachment and subsequent membrane permeabilization allowing PI incorporation (*129*), can be visualized by time-lapse images using a high magnification objective lens: CFSE-labeled HeLa cells turned round after they made contact with NK-92 cells, followed by PI uptake (Figure 4.5).

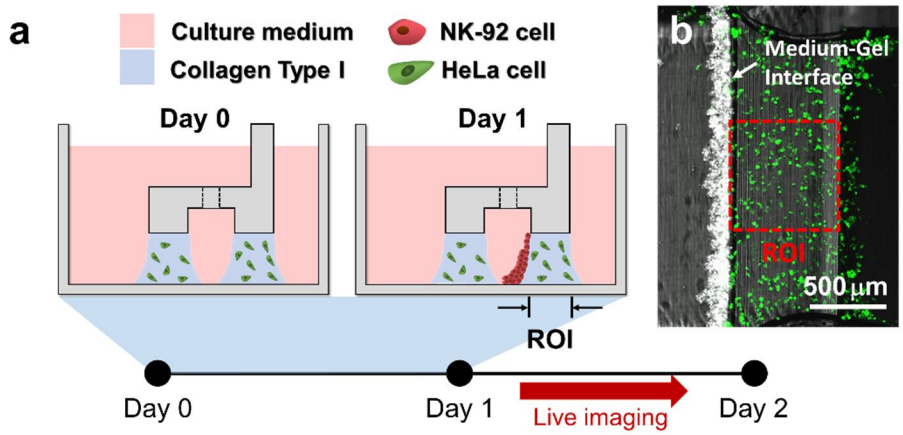

Figure 4.3. Procedure of 3D cytotoxicity assay and its outputs. (a) Schematic process of the assay. HeLa cells embedded in collagen were patterned under low rails (Day 0). After 24 hours of cultivation, NK-92 cells were loaded into a microchannel formed by the hydrogel. By tilting the device at an angle of 90 degrees, NK-92 cells were deposited on a collagen block (Day 1) and cultured for additional 24 hours to observe migration and cytotoxic activity of NK cells. (b) Initial state of the assay (Day 1).

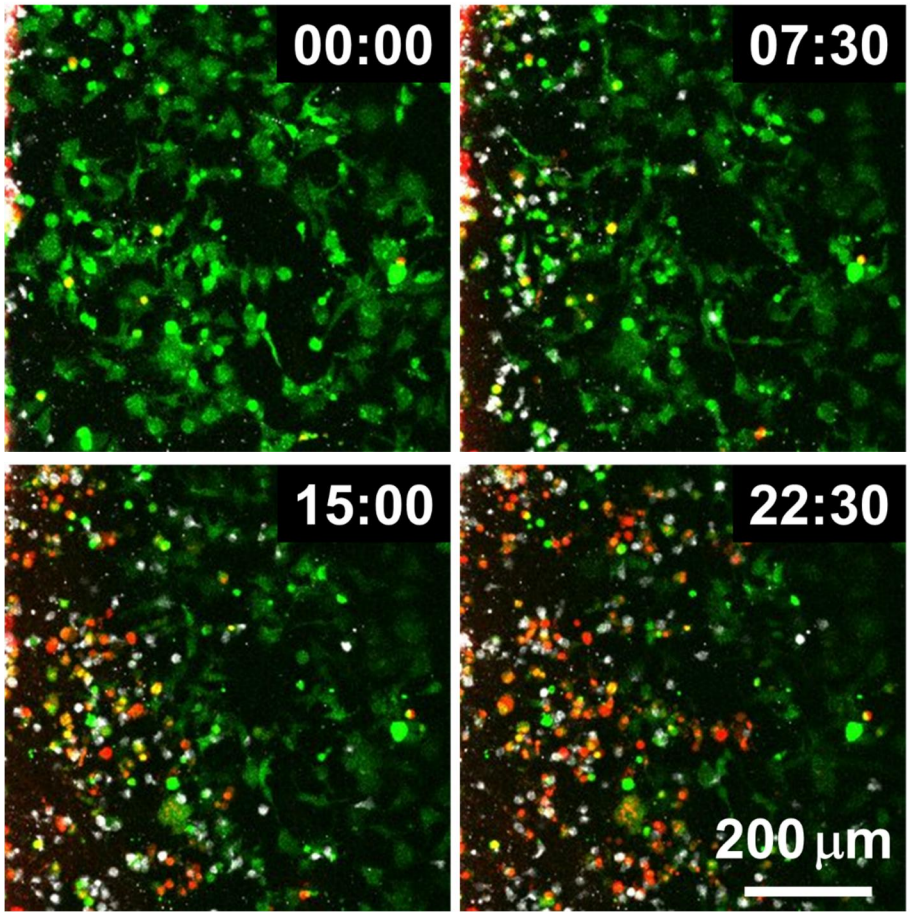

Figure 4.4. Live monitoring of migration and cytotoxic activity of NK-92 cells with 10X objective lens. NK-92 cells (white) penetrate into collagen matrix where HeLa cells are encapsulated. Propidium iodide (Red) displays dead cells. Time is indicated in HH:MM in the top right corner of each image.

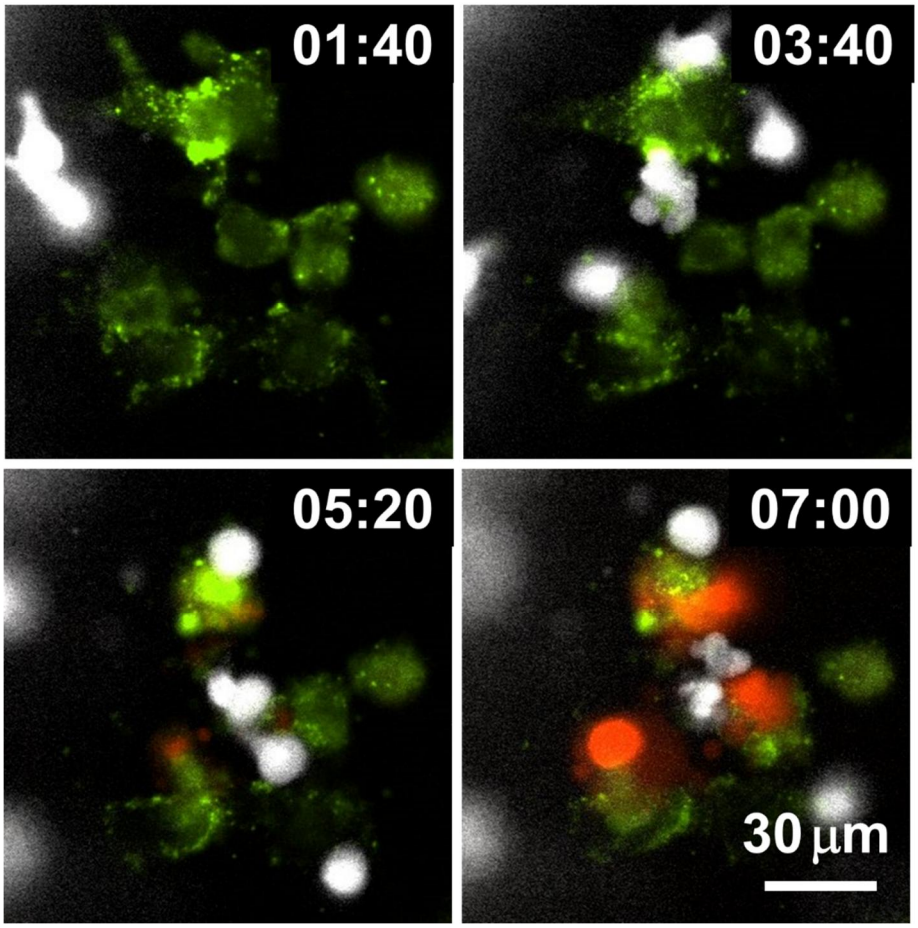

Figure 4.5. Live monitoring of migration and cytotoxic activity of NK-92 cells with 20X objective lens. NK-92 cells (white) penetrate into collagen matrix where HeLa cells are encapsulated. Propidium iodide (Red) displays dead cells. Time is indicated in HH:MM in the top right corner of each image.

4.3.3. 3D ECM reduce cytotoxicity

With this experimental setting, we first investigated how the presence of ECM and the density of cancer cells influenced NK cell cytotoxicity. HeLa cells in two different cell densities (0.8 x 10^6 cells/ml and 3.2 x 10^6 cells/ml) were encapsulated in collagen gels (3 mg/ml) while the NK-92 cell density added in the media was fixed (2.0 x 10^6 cells/ml), thus effectively total NK-92:HeLa were 5:1 and 20:1, typical ratio used for conventional cytotoxicity assays. Fluorescence images of square region of interest (ROI) with a side length of 700 μm, which is the dimension of the low rail width under which NK cells interact with HeLa cells, were acquired using a motorized stage 24 h after NK-92 cell seeding. The ROI was divided into seven sub-regions with a width of 100 μm, R0 to R6 (Figure 4.6). The number of NK cells penetrated into the collagen gels and the percentage of killed HeLa cells, or PI-labeled HeLa cells, in each sub-region were measured and plotted (Figure 4.7a and 4.7b). R0 and R6 were not considered because they were located near the interface between collagen gel and liquid media where capillary force-mediated meniscus formed (Figure 4.6), thus boundaries were not clearly defined in some cases.

NK-92 cell number was the highest in R1, and gradually decreased

as the sub-region became deeper (Figure 4.7a). NK-92 cells exhibited significantly higher cell numbers in all sub-regions for the lower HeLa cell density, or 20:1, than the case of 5:1 except for R1 (Figure 4.7a). Similar trends were observed for HeLa cell killing, as HeLa cell killing requires close proximity of NK-92 cells and HeLa cells (Figure 4.7b). These results indicate that HeLa cells in collagen gels hold NK-92 cells nearby by forming dynamic immunological synapses (*130*), thus NK-92 cell migration toward deeper sub-regions gets delayed until they kill substantial fraction of HeLa cells. Percentages of killed HeLa cells in entire sub-regions R1-R5 were measured and compared with 2D cytotoxicity assays performed with equivalent NK-92:HeLa ratio. In 2D, NK-92 cells killed ~ 90% of HeLa cells regardless of the ratio, whereas significantly lower percentage of HeLa cells were killed in 3D, and the higher HeLa cell killing occurred with the NK-92:HeLa ratio of 20:1. These results indicate that accessibility of cancer cells is a limiting factor, and migration of CLs is a rate limiting step in cytotoxicity in 3D ECM microenvironments.

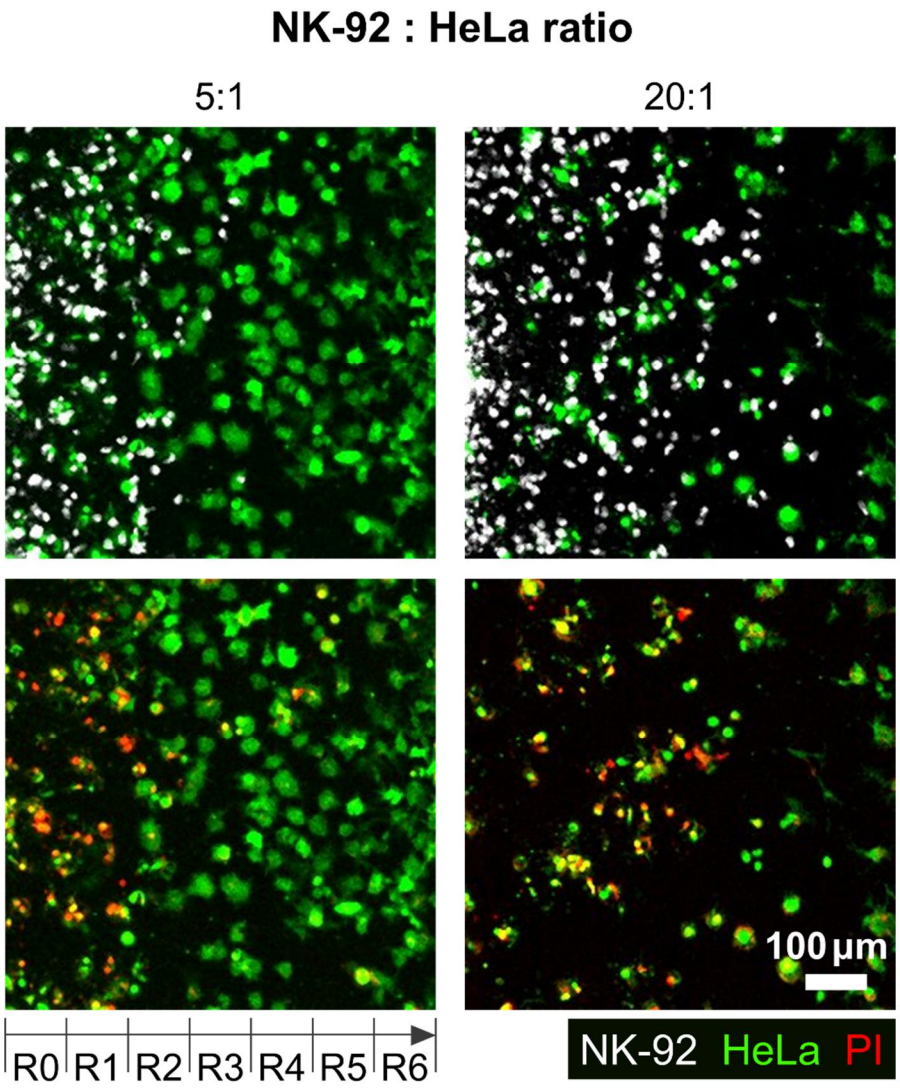

Figure 4.6. Images taken after 24 hours of interaction of NK cells and HeLa cells in two NK-92:HeLa ratios. HeLa cells (green) and NK-92 cells (white) are displayed in upper images and lower images show live/dead HeLa cells at the same moment with the upper images.

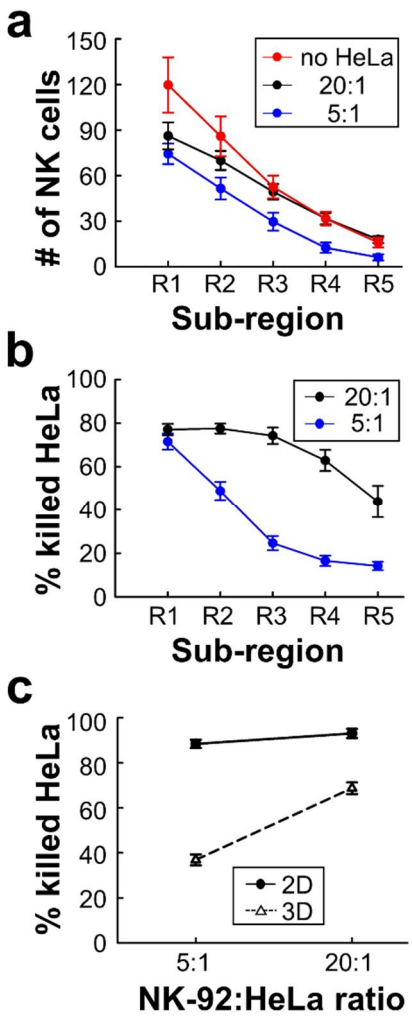

Figure 4.7. 3D ECM reduces cytotoxicity by limiting cancer cell accessibility. (a) The numbers of NK cells and (b) the percentage of killed HeLa cells within the ROI sub-regions in the two NK-92:HeLa ratios ($n \geq 18$). (c) The percentage of killed HeLa cells within the whole ROI from R1 to R5 in the two NK-92:HeLa ratios. ($n = 3$ for 2D assay, $n \geq 18$ for 3D assay). Dot plots in (b)-(d) show mean ± SEM.

4.3.4. Dense ECM impede migration of CLs

In many solid tumors, fibrosis characterized by dense and stiff ECM generation occurs surrounding areas of tumor cells. Fibrosis not only affects cancer cells by triggering various mechanotransduction pathways by stiffening ECM (*131*), but also influences immunotherapy efficacy by limiting CL infiltration into tumors (*114, 132*). We sought to investigate the role of ECM density, a key component of fibrosis, on lymphocyte cytotoxicity in 3D by using the device patterned with various concentrations of collagen (2, 3, 4 mg/ml). Effective NK-92:HeLa ratio was fixed to 5:1. Representative still images of the patterned collagen gels with various collagen concentrations 24 h after NK-92 cell seeding are shown in Figure 4.8. NK-92 cells distributed throughout the collagen gels in 2 mg/ml of collagen gel, whereas few NK-92 cells were observed in R4-R6 in 4 mg/ml of collagen gel. Overall, NK cell number was the highest in R1 and gradually decreased as the sub-region became deeper for all collagen concentrations (Figure 4.9a), and NK cell number was the highest for the lowest collagen concentration and gradually decreased as the collagen concentration increased for all sub-regions (Figure 4.9a). Similar trends in the percentage of killed HeLa cells were observed (Figure 4.9b). These results indicate that ECM density plays an important

role in NK cell migration in collagen gels, and consequently affects NK cell cytotoxicity.

Next, we investigated detailed interactions between NK-92 cells and HeLa cells encapsulated in different concentrations of collagen. By performing time-lapse imaging, we directly visualized NK-92 cell-HeLa cell interactions at a single cell level (Figure 4.10), and assessed how much time is needed for each NK-92 cell to successfully kill HeLa cells. Time for killing, which measures time from initial NK-92/HeLa contact to PI uptake in HeLa cells, was measured for each NK-92 cell successfully killed NK-92 cell and plotted for NK-92 cells in collagen gels with 2 and 4 mg/ml (Figure 4.11). Interestingly, time for killing of NK-92 cells in 4 mg/ml collagen gels was significantly lower than that of NK-92 cells in 2 mg/ml collagen gels. This result indicates that cytotoxicity of individual NK-92 cells is higher in higher concentration of collagen gels. Taken together, ECM density can influence both migration and cytotoxicity of CLs.

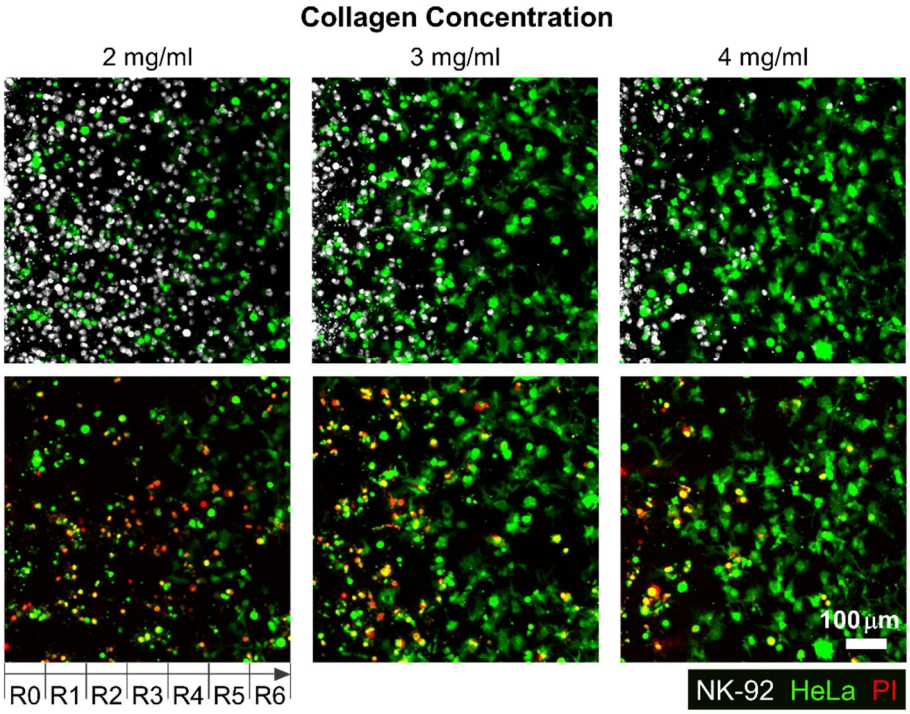

Figure 4.8. Images taken after 24 hours of interaction of NK cells and HeLa cells in three collagen concentrations. HeLa cells (green) and NK-92 cells (white) are displayed in upper images and lower images show live/dead HeLa cells at the same moment with upper images.

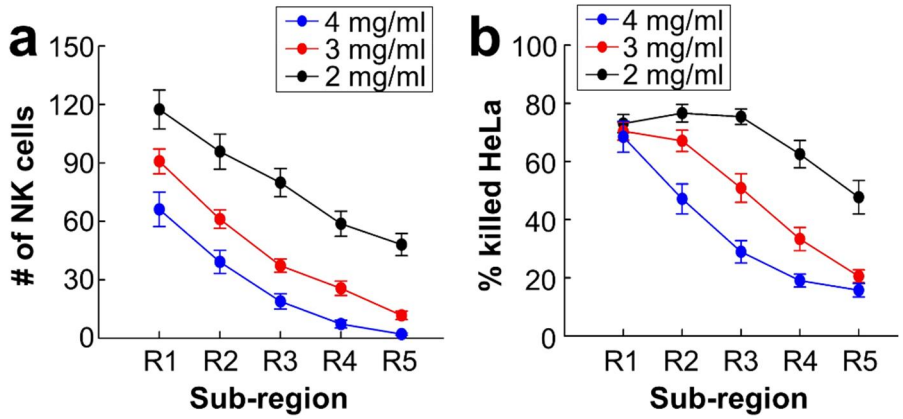

Figure 4.9. Dense ECM impedes cytotoxic activity of NK cells. (a) The numbers of NK cells and (b) the percentage of killed HeLa cells within the ROI sub-regions ($n \geq 16$).

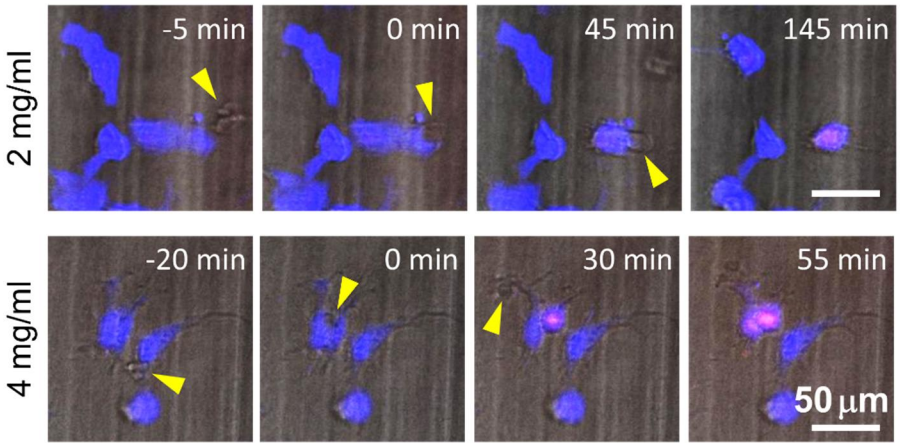

Figure 4.10. Live monitoring of cytotoxic activities of NK-92 cells (Yellow arrows) against HeLa cells (Blue). Propidium iodide (Red) shows the death of HeLa cells.

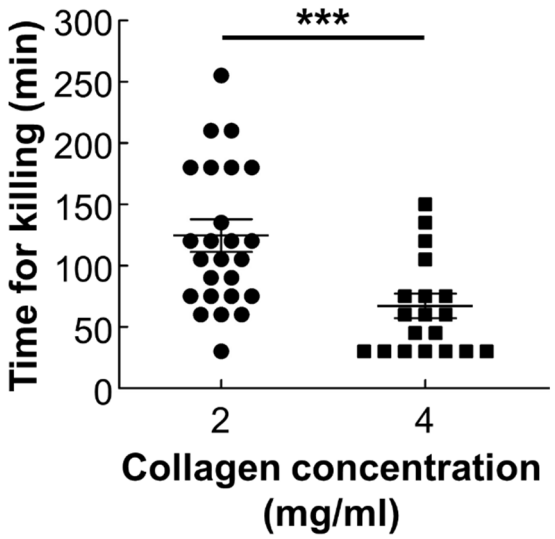

Figure 4.11. PI uptake time from the moment that NK-92 cells made a contact with HeLa cells in 2 and 4 mg/ml of collagens. Each dot was obtained from a single HeLa cell killed by a single NK-92 cell. For statistical comparison, unpaired two-tailed Student's t-test was performed, and the statistical significance was displayed as follows; *$p < 0.05$, **$p < 0.01$, ***$p < 0.001$.

4.4. Conclusions

Traditional *in vitro* 2D cytotoxicity assays against cancer cells have been widely used to evaluate *ex vivo* engineered or cultured CLs due to simplicity in assays, but the assay results may not be consistent with *in vivo* results due to the absence of 3D tumor microenvironment (TME). PDMS-based microfluidic devices recapitulating various aspects of TME, including hypoxia, inflammatory cytokines, immunosuppressive conditions, and vasculatures, have been developed to evaluate CLs in 3D (*125-127*).

However, PDMS-based devices require labor and time intensive batch fabrication processes, thus device fabrication limits experimental throughputs (*128*). To overcome this limitation, the CACI-IMPACT devices used in this study were massively produced using injection molding with polystyrene (PS) by customizing the design of the IMPACT device (*99*), which was previously developed by our group for 3D compartmentalized cell culture. In our experience of conducting the same 3D cytotoxicity assays using our PDMS-based co-culture device (*93*), approximately two days of serial processes, including casting (7 h), punching (1 h), bonding (10 m), and surface hydrophobicity restoration (> 1 d), were required. The series of manual processes can cause defects,

resulting in lower yields or lower uniformity of the final devices to be used in experiments. Furthermore, pressure sensitive loading process in PDMS device reduces usability and experimental throughput. In sharp contrast, CACI-IMPACT device requires less than 10 minutes for device preparation including 3 min of hydrophilic surface modification. In case that the device was packed after plasma treatment, no preparation is required except opening the packaging. Rail-based microstructures with hydrophilic surfaces further facilitated experiments by enabling simple and fast hydrogel patterning to be performed, and multi-well format further enhanced experimental throughputs by allowing multiple experiments to be performed simultaneously in a single device. In addition to improved device fabrication and experimental throughputs, long term monitoring of CL-cancer cell interactions is possible, as media change can be readily performed by aspirating media in the media reservoir and filling new media without perturbing hydrogels containing cells.

Using the injection molded devices, we performed 3D cytotoxicity assays with various density of cancer cells and various collagen concentrations. First, we found the presence of ECM and cancer cells could significantly reduce cytotoxicity of CLs by impeding

migration and limiting accessibility of cancer cells compared with 2D cytotoxicity assays (Figure 4.7). Presence of cancer cells in ECM may play dual role in cytotoxicity: it may impede infiltration of CL by interacting with CLs as we have shown, but at the same time, cancer cells can promote CL migration by producing chemokines such as CXCL9, 10, and 11 (*133*). As shown in Figure 4.7a, NK-92 cell distribution in collagen gels lacking HeLa cells (no HeLa) was comparable to that in collagen gels with low density of HeLa cells (20:1) except for entry regions, where NK-92 cell numbers were slightly higher for collagen gels lacking HeLa cells, indicating chemotaxis-mediated NK-92 cell migration was minimal in our system. Second, we found ECM density played an important role in 3D cytotoxicity by independently regulating migration-mediated cancer cell contact and direct cancer cell killing (Figure 4.9). Indeed, collagen density can influence various physical properties of collagen gels such as pore size and stiffness (*134*). When collagen concentration was increased, NK cell infiltration into collagen gels was substantially reduced presumably due to reduced pore size that limits amoeboid-mode immune cell migration (*135*). Indeed, increased ECM density observed in fibrotic tumors reduced activity of T cells by limiting physical access of tumor cells (*119*), indicating our device may

be a good model system to evaluate *ex vivo* engineered CLs for fibrotic tumors. Interestingly, cytotoxicity of individual NK cells were significantly enhanced when collagen concentration was increased (Figure 4.11). While detailed mechanisms for enhanced cytotoxicity in collagen-dense environments need to be determined, it is possible that stiff ECM environments in high concentration of collagen facilitate tumor cell lysis by increasing tumor cell tension, which enhances perforin-mediated pore formation on tumor cell membrane (*136*).

Our preliminary 3D cytotoxicity assay using human primary NK cells revealed that CACI-IMPACT platform can be used for primary lymphocytes, while detailed assay conditions need to be adjusted depending on cell types (Figure 4.12). Primary NK cells exhibited much higher motility and cytotoxicity compared with NK-92 cells: they uniformly distributed in entire collagen gels (Figure 4.12b) and killed the majority of HeLa cells (Figure 4.12c) within 12 h in dense ECM (4mg/ml of collagen), in which NK-92 cells killed only ~ 40% of HeLa cells for 24 h (Figure 4.9b). Superior cytotoxicity of primary NK cells in our assay is partly due to smaller size of primary NK cells (diameter ~ 8 μm) compared with that of NK-92 cells (diameter ~ 14 μm), which plays important role in cell migration in dense ECM (*134*), further confirming

importance of lymphocyte motility in 3D cytotoxicity.

To sum up, we introduced an injection molded microfluidic device for assessing cytotoxicity of CLs in 3D environment. The proposed device is characterized by (i) enhanced productivity via injection molding, (ii) enhanced experimental throughput mediated by multi-well format of the device, and (iii) hydrophilic rail-based microstructures facilitating hydrogel patterning with simple pipetting. Using the device, we found 3D ECM significantly reduce cytotoxicity of CLs by impeding migration and access to tumor cells compared with traditional 2D assays. We also found denser ECM impede migration of CLs but enable effective killing once CLs contact with tumor cells. The results show how important the presence of ECM is for accessing cytotoxicity of CLs against solid tumors. We think this injection molded 3D culture platform could be used to evaluate cytotoxicity of CLs in 3D environment and to identify new therapeutic approaches mediated by adoptive transferred CLs against solid tumors.

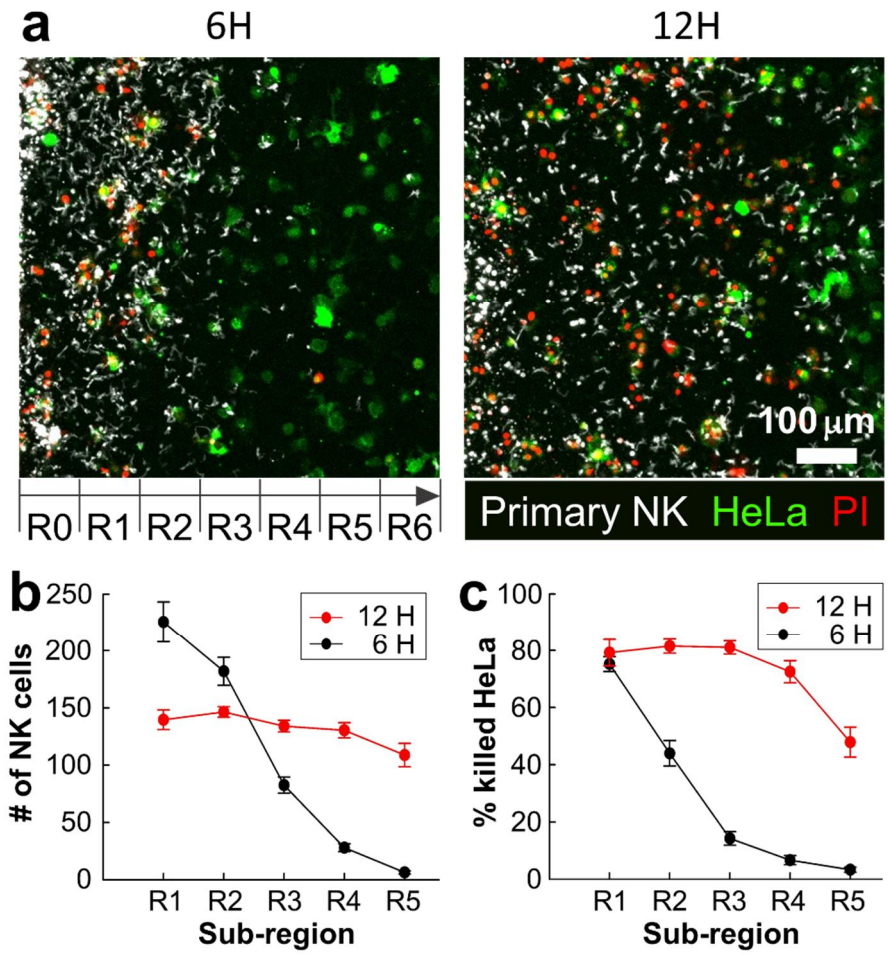

Figure 4.12. 3D cytotoxicity assay performed with primary NK cells against HeLa cells. (A) Representative images taken after 6H (left) and 12H (right) of primary NK/HeLa cells co-culture. (B) The number of primary NK cells and (C) the percentage of killed HeLa cells within the ROI sub-regions after 6H (black) and 12H (red) of primary NK/HeLa cells co-culture.

Chapter 5. Concluding Remarks

In this thesis, we suggested two CGP methods by integrating microstructures with conventional cell culturewares. In chapter 2, micropillar array embossed on petri-dish enabled multiscale liquid patterning by sweeping bulk liquid over the surface. The patterning mechanism on a basic form of a 2 × 2 rectangular array of circular pillars is analyzed theoretically and verified with experiments. Nanoliter-to-microliter volumes of liquids are patterned into various shapes by arranging the pillars based on the analysis. Furthermore, an array of geometrically modified pillars can capture approximately 8000 droplets on a large substrate (55 mm × 55 mm) in one step. Given the simplistic method of wipe patterning, the proposed platform can be utilized in both manual benchtop and automated settings. We will provide proof of concept experiments of single colony isolation using nanoliter-scale liquid patterning and of human angiogenic vessel formation using sequential patterning of microliter-scale liquids.

In chapter 3, rail-based microstructure was introduced to guide air-liquid interface retrieved by aspiration, resulting in remaining hydrogels only under low rails. We provide a design rule for the device structure

and the capillary pressure condition upon verifying a theoretical model to explain the physical principle. We demonstrate formation of multiple hollow channels or hydrogel islands with a single aspiration. Then we test vasculogenic capacity of various cell types using a microfluidic co-culture system obtained by our technology, to illustrate its capabilities as a viable micro-manufacturing scheme for high-throughput cellular co-culture.

In chapter 4, we introduced a 3D cytotoxicity assay to assess cytotoxicity of lymphocytes in 3D microenvironment in high-throughput fashions. Rail-based microfluidic design described in chapter 3 was integrated within a single 96-well and the wells were rectangularly arrayed in 2 × 6 to enhance the experimental throughput. The rail-based microstructures facilitate hydrogel patterning with simple pipetting so that hydrogel pre-solution aspirated with 10 μl pipette can be patterned in 12 wells within 30 s. To demonstrate 3D cytotoxicity assay, we patterned HeLa cells encapsulated by collagen gel and observed infiltration, migration and cytotoxic activity of NK-92 cells against HeLa cells in the collagen matrix. We found that 3D ECM significantly reduced migration of cytotoxic lymphocytes and access to cancer cells, resulting in lower cytotoxicity compared with 2D assays.

Compared with traditional closed microfluidic devices made with PDMS, the open microfluidic platforms utilizing CGP methods (i) are scalable, (ii) have enhanced experimental throughput, (iii) are compatible with automated liquid dispenser or imaging systems due to their standardized format, and (iv) are highly accessible to the cultured tissue. We expect open microfluidic devices introduced so far can address limitations that impede commercialization of organs-on-chips and help organs-on-chips to be used in industry such as pre-clinical drug screening and developmental process of drugs or cosmetics.

Bibliography

1. C. D. Chin, V. Linder, S. K. Sia, Commercialization of microfluidic point-of-care diagnostic devices. *Lab Chip* **12**, 2118-2134 (2012).
2. S. Kim, H. J. Kim, N. L. Jeon, Biological applications of microfluidic gradient devices. *Integr Biol (Camb)* **2**, 584-603 (2010).
3. P. Shrimal, G. Jadeja, S. Patel, A review on novel methodologies for drug nanoparticle preparation: Microfluidic approach. *Chemical Engineering Research and Design* **153**, 728-756 (2020).
4. P. Sajeesh, A. K. Sen, Particle separation and sorting in microfluidic devices: a review. *Microfluidics and Nanofluidics* **17**, 1-52 (2013).
5. S. Halldorsson, E. Lucumi, R. Gomez-Sjoberg, R. M. T. Fleming, Advantages and challenges of microfluidic cell culture in polydimethylsiloxane devices. *Biosens Bioelectron* **63**, 218-231 (2015).
6. D. Di Carlo, L. P. Lee, Dynamic single-cell analysis for quantitative biology. *Analytical chemistry* **78**, 7918-7925 (2006).
7. J. Fu *et al.*, Mechanical regulation of cell function with geometrically modulated elastomeric substrates. *Nat Methods* **7**, 733-736 (2010).
8. D. Huh *et al.*, Reconstituting organ-level lung functions on a chip. *Science* **328**, 1662-1668 (2010).
9. H. Cho, H. Y. Kim, J. Y. Kang, T. S. Kim, How the capillary burst microvalve works. *J Colloid Interface Sci* **306**, 379-385 (2007).
10. T. E. Park *et al.*, Hypoxia-enhanced Blood-Brain Barrier Chip recapitulates human barrier function and shuttling of drugs and antibodies. *Nat Commun* **10**, 2621 (2019).
11. H. J. Kim, D. Huh, G. Hamilton, D. E. Ingber, Human gut-on-a-chip inhabited by microbial flora that experiences intestinal peristalsis-like motions and flow. *Lab Chip* **12**, 2165-2174 (2012).
12. N. Jusoh, S. Oh, S. Kim, J. Kim, N. L. Jeon, Microfluidic vascularized bone tissue model with hydroxyapatite-incorporated extracellular matrix. *Lab Chip* **15**, 3984-3988 (2015).

13. K. H. Benam *et al.*, Small airway-on-a-chip enables analysis of human lung inflammation and drug responses in vitro. *Nat Methods* **13**, 151-157 (2016).
14. K. J. Jang *et al.*, Human kidney proximal tubule-on-a-chip for drug transport and nephrotoxicity assessment. *Integr Biol (Camb)* **5**, 1119-1129 (2013).
15. C. D. Edington *et al.*, Interconnected Microphysiological Systems for Quantitative Biology and Pharmacology Studies. *Sci Rep* **8**, 4530 (2018).
16. I. Maschmeyer *et al.*, A four-organ-chip for interconnected long-term co-culture of human intestine, liver, skin and kidney equivalents. *Lab Chip* **15**, 2688-2699 (2015).
17. J. Vriend *et al.*, Flow stimulates drug transport in a human kidney proximal tubule-on-a-chip independent of primary cilia. *Biochim Biophys Acta Gen Subj* **1864**, 129433 (2020).
18. N. R. Wevers *et al.*, A perfused human blood-brain barrier on-a-chip for high-throughput assessment of barrier function and antibody transport. *Fluids Barriers CNS* **15**, 23 (2018).
19. C. Beaurivage *et al.*, Development of a Gut-On-A-Chip Model for High Throughput Disease Modeling and Drug Discovery. *Int J Mol Sci* **20**, (2019).
20. A. Petrosyan *et al.*, A glomerulus-on-a-chip to recapitulate the human glomerular filtration barrier. *Nat Commun* **10**, 3656 (2019).
21. M. B. Chen *et al.*, On-chip human microvasculature assay for visualization and quantification of tumor cell extravasation dynamics. *Nat Protoc* **12**, 865-880 (2017).
22. D. Huh *et al.*, Microfabrication of human organs-on-chips. *Nat Protoc* **8**, 2135-2157 (2013).
23. C. P. Huang *et al.*, Engineering microscale cellular niches for three-dimensional multicellular co-cultures. *Lab Chip* **9**, 1740-1748 (2009).
24. P. Vulto *et al.*, Phaseguides: a paradigm shift in microfluidic priming and emptying. *Lab Chip* **11**, 1596-1602 (2011).
25. H. van Heeren, R. Tantra, P. Salomon, Microfluidic devices: a road forward by standardization of interconnects and classification. *Microfluidics and Nanofluidics* **19**, 1203-1207 (2015).
26. S. B. Berry *et al.*, Upgrading well plates using open microfluidic patterning. *Lab*

Chip **17**, 4253-4264 (2017).

27. A. R. Aref *et al.*, 3D microfluidic ex vivo culture of organotypic tumor spheroids to model immune checkpoint blockade. *Lab on a chip* **18**, 3129-3143 (2018).
28. D. T. Le *et al.*, PD-1 Blockade in Tumors with Mismatch-Repair Deficiency. *N Engl J Med* **372**, 2509-2520 (2015).
29. J. Kaiser, Too much of a good thing? *Science* **359**, 1346-1347 (2018).
30. P. S. Hegde, D. S. Chen, Top 10 Challenges in Cancer Immunotherapy. *Immunity* **52**, 17-35 (2020).
31. A. Zloza *et al.*, Workshop on challenges, insights, and future directions for mouse and humanized models in cancer immunology and immunotherapy: a report from the associated programs of the 2016 annual meeting for the Society for Immunotherapy of cancer. *J Immunother Cancer* **5**, 77 (2017).
32. S. N. Bailey, D. M. Sabatini, B. R. Stockwell, Microarrays of small molecules embedded in biodegradable polymers for use in mammalian cell-based screens. *Proceedings of the National Academy of Sciences of the United States of America* **101**, 16144-16149 (2004).
33. J. E. Bradner *et al.*, A robust small-molecule microarray platform for screening cell lysates. *Chem Biol* **13**, 493-504 (2006).
34. R. A. Lindquist *et al.*, Genome-scale RNAi on living-cell microarrays identifies novel regulators of Drosophila melanogaster TORC1-S6K pathway signaling. *Genome Res* **21**, 433-446 (2011).
35. D. J. Siegwart *et al.*, Combinatorial synthesis of chemically diverse core-shell nanoparticles for intracellular delivery. *Proceedings of the National Academy of Sciences of the United States of America* **108**, 12996-13001 (2011).
36. J. Ziauddin, D. M. Sabatini, Microarrays of cells expressing defined cDNAs. *Nature* **411**, 107-110 (2001).
37. C. J. Flaim, S. Chien, S. N. Bhatia, An extracellular matrix microarray for probing cellular differentiation. *Nature methods* **2**, 119-125 (2005).
38. A. Huebner *et al.*, Quantitative detection of protein expression in single cells using droplet microfluidics. *Chem Commun (Camb)*, 1218-1220 (2007).
39. V. Chokkalingam *et al.*, Probing cellular heterogeneity in cytokine-secreting immune cells using droplet-based microfluidics. *Lab on a chip* **13**, 4740-4744

(2013).

40. S. L. Sjostrom *et al.*, High-throughput screening for industrial enzyme production hosts by droplet microfluidics. *Lab on a chip* **14**, 806-813 (2014).
41. H. F. Chan, Y. Zhang, K. W. Leong, Efficient One-Step Production of Microencapsulated Hepatocyte Spheroids with Enhanced Functions. *Small* **12**, 2720-2730 (2016).
42. Q. Chen *et al.*, Controlled assembly of heterotypic cells in a core-shell scaffold: organ in a droplet. *Lab on a chip* **16**, 1346-1349 (2016).
43. J. C. Baret *et al.*, Fluorescence-activated droplet sorting (FADS): efficient microfluidic cell sorting based on enzymatic activity. *Lab on a chip* **9**, 1850-1858 (2009).
44. M. T. Guo, A. Rotem, J. A. Heyman, D. A. Weitz, Droplet microfluidics for high-throughput biological assays. *Lab on a chip* **12**, 2146-2155 (2012).
45. E. Ueda, F. L. Geyer, V. Nedashkivska, P. A. Levkin, DropletMicroarray: facile formation of arrays of microdroplets and hydrogel micropads for cell screening applications. *Lab on a chip* **12**, 5218-5224 (2012).
46. A. N. Efremov, E. Stanganello, A. Welle, S. Scholpp, P. A. Levkin, Micropatterned superhydrophobic structures for the simultaneous culture of multiple cell types and the study of cell-cell communication. *Biomaterials* **34**, 1757-1763 (2013).
47. A. A. Popova *et al.*, Droplet-Array (DA) Sandwich Chip: A Versatile Platform for High-Throughput Cell Screening Based on Superhydrophobic-Superhydrophilic Micropatterning. *Adv Mater* **27**, 5217-5222 (2015).
48. A. I. Neto *et al.*, Fabrication of Hydrogel Particles of Defined Shapes Using Superhydrophobic-Hydrophilic Micropatterns. *Adv Mater* **28**, 7613-7619 (2016).
49. E. Kim, Y. N. Xia, X. M. Zhao, G. M. Whitesides, Solvent-assisted microcontact molding: A convenient method for fabricating three-dimensional structures on surfaces of polymers. *Adv Mater* **9**, 651-654 (1997).
50. J. Bico, U. Thiele, D. Quéré, Wetting of textured surfaces. *Colloids and Surfaces A: Physicochemical and Engineering Aspects* **206**, 41-46 (2002).
51. C. Semprebon, P. Forsberg, C. Priest, M. Brinkmann, Pinning and wicking in regular pillar arrays. *Soft Matter* **10**, 5739-5748 (2014).
52. S. J. Kim *et al.*, Liquid spreading on superhydrophilic micropillar arrays. *Journal*

of Fluid Mechanics **680**, 477-487 (2011).

53. S. J. Kim, J. Kim, M.-W. Moon, K.-R. Lee, H.-Y. Kim, Experimental study of drop spreading on textured superhydrophilic surfaces. *Physics of Fluids* **25**, 092110 (2013).
54. T. Podgorski, J. M. Flesselles, L. Limat, Corners, cusps, and pearls in running drops. *Physical review letters* **87**, 036102 (2001).
55. S. Ni, J. Leemann, I. Buttinoni, L. Isa, H. Wolf, Programmable colloidal molecules from sequential capillarity-assisted particle assembly. *Sci Adv* **2**, e1501779 (2016).
56. F. Brochard-Wyart, P. G. de Gennes, Dynamics of partial wetting. *Advances in Colloid and Interface Science* **39**, 1-11 (1992).
57. H.-Y. Kim, On Thermocapillary Propulsion of Microliquid Slug. *Nanoscale and Microscale Thermophysical Engineering* **11**, 351-362 (2007).
58. J. C. Love, J. L. Ronan, G. M. Grotenbreg, A. G. van der Veen, H. L. Ploegh, A microengraving method for rapid selection of single cells producing antigen-specific antibodies. *Nat Biotechnol* **24**, 703-707 (2006).
59. S. M. Park *et al.*, Molecular profiling of single circulating tumor cells from lung cancer patients. *Proceedings of the National Academy of Sciences of the United States of America* **113**, E8379-E8386 (2016).
60. D. K. Wood, D. M. Weingeist, S. N. Bhatia, B. P. Engelward, Single cell trapping and DNA damage analysis using microwell arrays. *Proceedings of the National Academy of Sciences of the United States of America* **107**, 10008-10013 (2010).
61. J. Gole *et al.*, Massively parallel polymerase cloning and genome sequencing of single cells using nanoliter microwells. *Nat Biotechnol* **31**, 1126-1132 (2013).
62. G. F. Christopher, S. L. Anna, Microfluidic methods for generating continuous droplet streams. *Journal of Physics D: Applied Physics* **40**, R319-R336 (2007).
63. A. V. Lemmo, J. T. Fisher, H. M. Geysen, D. J. Rose, Characterization of an inkjet chemical microdispenser for combinatorial library synthesis. *Analytical chemistry* **69**, 543-551 (1997).
64. T. B. Jones, M. Gunji, M. Washizu, M. J. Feldman, Dielectrophoretic liquid actuation and nanodroplet formation. *Journal of Applied Physics* **89**, 1441-1448 (2001).
65. S. Lindstrom, H. Andersson-Svahn, Overview of single-cell analyses:

microdevices and applications. *Lab on a chip* **10**, 3363-3372 (2010).

66. T. P. Lagus, J. F. Edd, A review of the theory, methods and recent applications of high-throughput single-cell droplet microfluidics. *Journal of Physics D: Applied Physics* **46**, 114005 (2013).
67. D. Hummer, F. Kurth, N. Naredi-Rainer, P. S. Dittrich, Single cells in confined volumes: microchambers and microdroplets. *Lab on a chip* **16**, 447-458 (2016).
68. J. R. Kovac, J. Voldman, Intuitive, image-based cell sorting using optofluidic cell sorting. *Analytical chemistry* **79**, 9321-9330 (2007).
69. W. H. Tan, S. Takeuchi, A trap-and-release integrated microfluidic system for dynamic microarray applications. *Proceedings of the National Academy of Sciences of the United States of America* **104**, 1146-1151 (2007).
70. W. H. Tan, S. Takeuchi, Dynamic microarray system with gentle retrieval mechanism for cell-encapsulating hydrogel beads. *Lab on a chip* **8**, 259-266 (2008).
71. Z. Zhu, O. Frey, D. S. Ottoz, F. Rudolf, A. Hierlemann, Microfluidic single-cell cultivation chip with controllable immobilization and selective release of yeast cells. *Lab on a chip* **12**, 906-915 (2012).
72. A. Morimoto *et al.*, High-Density Dielectrophoretic Microwell Array for Detection, Capture, and Single-Cell Analysis of Rare Tumor Cells in Peripheral Blood. *PloS one* **10**, e0130418 (2015).
73. H. S. Kim, T. P. Devarenne, A. Han, A high-throughput microfluidic single-cell screening platform capable of selective cell extraction. *Lab on a chip* **15**, 2467-2475 (2015).
74. D. J. Collins, A. Neild, A. deMello, A. Q. Liu, Y. Ai, The Poisson distribution and beyond: methods for microfluidic droplet production and single cell encapsulation. *Lab on a chip* **15**, 3439-3459 (2015).
75. T. C. Chang *et al.*, Microwell arrays reveal cellular heterogeneity during the clonal expansion of transformed human cells. *Technology (Singap World Sci)* **3**, 163-171 (2015).
76. L. I. Lin, S. H. Chao, D. R. Meldrum, Practical, microfabrication-free device for single-cell isolation. *PloS one* **4**, e6710 (2009).
77. H. Kaji, G. Camci-Unal, R. Langer, A. Khademhosseini, Engineering systems for

the generation of patterned co-cultures for controlling cell-cell interactions. *Biochim Biophys Acta* **1810**, 239-250 (2011).

78. W. F. Liu, C. S. Chen, Cellular and multicellular form and function. *Adv Drug Deliv Rev* **59**, 1319-1328 (2007).
79. A. Khademhosseini, R. Langer, J. Borenstein, J. P. Vacanti, Microscale technologies for tissue engineering and biology. *Proceedings of the National Academy of Sciences of the United States of America* **103**, 2480-2487 (2006).
80. J. Fukuda *et al.*, Micropatterned cell co-cultures using layer-by-layer deposition of extracellular matrix components. *Biomaterials* **27**, 1479-1486 (2006).
81. J. Tien, C. M. Nelson, C. S. Chen, Fabrication of aligned microstructures with a single elastomeric stamp. *Proceedings of the National Academy of Sciences of the United States of America* **99**, 1758-1762 (2002).
82. S. Takayama *et al.*, Patterning cells and their environments using multiple laminar fluid flows in capillary networks. *Proceedings of the National Academy of Sciences of the United States of America* **96**, 5545-5548 (1999).
83. M. Suzuki, T. Yasukawa, H. Shiku, T. Matsue, Negative dielectrophoretic patterning with different cell types. *Biosens Bioelectron* **24**, 1049-1053 (2008).
84. S. N. Bhatia, U. J. Balis, M. L. Yarmush, M. Toner, Microfabrication of hepatocyte/fibroblast co-cultures: role of homotypic cell interactions. *Biotechnology progress* **14**, 378-387 (1998).
85. F. Pampaloni, E. G. Reynaud, E. H. K. Stelzer, The third dimension bridges the gap between cell culture and live tissue. *Nat Rev Mol Cell Bio* **8**, 839-845 (2007).
86. S. Kim, H. Lee, M. Chung, N. L. Jeon, Engineering of functional, perfusable 3D microvascular networks on a chip. *Lab on a chip* **13**, 1489-1500 (2013).
87. Y. Du, E. Lo, S. Ali, A. Khademhosseini, Directed assembly of cell-laden microgels for fabrication of 3D tissue constructs. *Proceedings of the National Academy of Sciences of the United States of America* **105**, 9522-9527 (2008).
88. M. Kang *et al.*, Capillarity Guided Patterning of Microliquids. *Small* **11**, 2789-2797 (2015).
89. W. F. Liu, C. S. Chen, Cellular and multicellular form and function. *Adv Drug Deliver Rev* **59**, 1319-1328 (2007).
90. D. Huh, G. A. Hamilton, D. E. Ingber, From 3D cell culture to organs-on-chips.

Trends Cell Biol **21**, 745-754 (2011).

91. K. Yum, S. G. Hong, K. E. Healy, L. P. Lee, Physiologically relevant organs on chips. *Biotechnol J* **9**, 16-27 (2014).
92. C. Moraes, G. Mehta, S. C. Lesher-Perez, S. Takayama, Organs-on-a-chip: a focus on compartmentalized microdevices. *Ann Biomed Eng* **40**, 1211-1227 (2012).
93. S. Kim, H. Lee, M. Chung, N. L. Jeon, Engineering of functional, perfusable 3D microvascular networks on a chip. *Lab on a Chip* **13**, (2013).
94. S.-R. Lee *et al.*, Modeling neural circuit, blood–brain barrier, and myelination on a microfluidic 96 well plate. *Biofabrication* **11**, (2019).
95. M. Campisi *et al.*, 3D self-organized microvascular model of the human blood-brain barrier with endothelial cells, pericytes and astrocytes. *Biomaterials* **180**, 117-129 (2018).
96. J. S. Jeon *et al.*, Human 3D vascularized organotypic microfluidic assays to study breast cancer cell extravasation. *Proc Natl Acad Sci U S A* **112**, 214-219 (2015).
97. S. H. Lee *et al.*, Capillary based patterning of cellular communities in laterally open channels. *Anal Chem* **82**, 2900-2906 (2010).
98. B. P. Casavant *et al.*, Suspended microfluidics. *Proceedings of the National Academy of Sciences of the United States of America* **110**, 10111-10116 (2013).
99. Y. Lee *et al.*, Microfluidics within a well: an injection-molded plastic array 3D culture platform. *Lab Chip* **18**, 2433-2440 (2018).
100. S. Lee *et al.*, Engineering tumor vasculature on an injection-molded plastic array 3D culture (IMPACT) platform. *Lab Chip* **19**, 2071-2080 (2019).
101. J. Berthier, K. A. Brakke, E. Berthier, *Open microfluidics*. (John Wiley & Sons, 2016).
102. J. Ko *et al.*, Tumor spheroid-on-a-chip: a standardized microfluidic culture platform for investigating tumor angiogenesis. *Lab Chip* **19**, 2822-2833 (2019).
103. P.-G. De Gennes, F. Brochard-Wyart, D. Quéré, *Capillarity and wetting phenomena: drops, bubbles, pearls, waves*. (Springer Science & Business Media, 2013).
104. J. Ko, Y. Lee, S. Lee, S. R. Lee, N. L. Jeon, Human Ocular Angiogenesis-Inspired Vascular Models on an Injection-Molded Microfluidic Chip. *Adv Healthc Mater* **8**, e1900328 (2019).

105. X. Wang *et al.*, Engineering anastomosis between living capillary networks and endothelial cell-lined microfluidic channels. *Lab Chip* **16**, 282-290 (2016).
106. S. A. Rosenberg, N. P. Restifo, Adoptive cell transfer as personalized immunotherapy for human cancer. *Science* **348**, 62-68 (2015).
107. S. L. Maude *et al.*, Chimeric antigen receptor T cells for sustained remissions in leukemia. *N Engl J Med* **371**, 1507-1517 (2014).
108. D. L. Porter, B. L. Levine, M. Kalos, A. Bagg, C. H. June, Chimeric antigen receptor–modified T cells in chronic lymphoid leukemia. *New England Journal of Medicine* **365**, 725-733 (2011).
109. J. N. Kochenderfer *et al.*, Eradication of B-lineage cells and regression of lymphoma in a patient treated with autologous T cells genetically engineered to recognize CD19. *Blood* **116**, 4099-4102 (2010).
110. C. H. June, R. S. O'Connor, O. U. Kawalekar, S. Ghassemi, M. C. Milone, CAR T cell immunotherapy for human cancer. *Science* **359**, 1361-1365 (2018).
111. W. A. Lim, C. H. June, The Principles of Engineering Immune Cells to Treat Cancer. *Cell* **168**, 724-740 (2017).
112. C. Guillerey, N. D. Huntington, M. J. Smyth, Targeting natural killer cells in cancer immunotherapy. *Nat Immunol* **17**, 1025-1036 (2016).
113. R. Handgretinger, K. Schilbach, The potential role of gammadelta T cells after allogeneic HCT for leukemia. *Blood* **131**, 1063-1072 (2018).
114. J. A. Joyce, D. T. Fearon, T cell exclusion, immune privilege, and the tumor microenvironment. *Science* **348**, 74-80 (2015).
115. M. M. D'Aloia, I. G. Zizzari, B. Sacchetti, L. Pierelli, M. Alimandi, CAR-T cells: the long and winding road to solid tumors. *Cell Death Dis* **9**, 282 (2018).
116. M. Binnewies *et al.*, Understanding the tumor immune microenvironment (TIME) for effective therapy. *Nat Med* **24**, 541-550 (2018).
117. K. G. Anderson, I. M. Stromnes, P. D. Greenberg, Obstacles Posed by the Tumor Microenvironment to T cell Activity: A Case for Synergistic Therapies. *Cancer Cell* **31**, 311-325 (2017).
118. D. E. Speiser, P. C. Ho, G. Verdeil, Regulatory circuits of T cell function in cancer. *Nat Rev Immunol* **16**, 599-611 (2016).
119. H. Salmon *et al.*, Matrix architecture defines the preferential localization and

migration of T cells into the stroma of human lung tumors. *J Clin Invest* **122**, 899-910 (2012).

120. K. Ganesh, J. Massague, TGF-beta Inhibition and Immunotherapy: Checkmate. *Immunity* **48**, 626-628 (2018).
121. R. Lichtenfels, W. E. Biddison, H. Schulz, A. B. Vogt, R. Martin, CARE-LASS (calcein-release-assay), an improved fluorescence-based test system to measure cytotoxic T lymphocyte activity. *J Immunol Methods* **172**, 227-239 (1994).
122. K. Brunner, J. Mauel, J.-C. Cerottini, B. Chapuis, Quantitative assay of the lytic action of immune lymphoid cells of 51Cr-labelled allogeneic target cells in vitro; inhibition by isoantibody and by drugs. *Immunology* **14**, 181 (1968).
123. W. J. Polacheck, R. Li, S. G. Uzel, R. D. Kamm, Microfluidic platforms for mechanobiology. *Lab Chip* **13**, 2252-2267 (2013).
124. G. Adriani *et al.*, Microfluidic models for adoptive cell-mediated cancer immunotherapies. *Drug Discov Today* **21**, 1472-1478 (2016).
125. A. Pavesi *et al.*, A 3D microfluidic model for preclinical evaluation of TCR-engineered T cells against solid tumors. *JCI Insight* **2**, (2017).
126. S. W. L. Lee *et al.*, Characterizing the Role of Monocytes in T Cell Cancer Immunotherapy Using a 3D Microfluidic Model. *Front Immunol* **9**, 416 (2018).
127. J. M. Ayuso *et al.*, Evaluating natural killer cell cytotoxicity against solid tumors using a microfluidic model. *OncoImmunology*, 1-11 (2018).
128. Y. Shin *et al.*, Microfluidic assay for simultaneous culture of multiple cell types on surfaces or within hydrogels. *Nat Protoc* **7**, 1247-1259 (2012).
129. N. J. Waterhouse *et al.*, Cytotoxic T lymphocyte-induced killing in the absence of granzymes A and B is unique and distinct from both apoptosis and perforin-dependent lysis. *J Cell Biol* **173**, 133-144 (2006).
130. J. Deguine, B. Breart, F. Lemaitre, J. P. Di Santo, P. Bousso, Intravital imaging reveals distinct dynamics for natural killer and CD8(+) T cells during tumor regression. *Immunity* **33**, 632-644 (2010).
131. J. J. Northey, L. Przybyla, V. M. Weaver, Tissue Force Programs Cell Fate and Tumor Aggression. *Cancer Discov* **7**, 1224-1237 (2017).
132. H. Jiang, S. Hegde, D. G. DeNardo, Tumor-associated fibrosis as a regulator of tumor immunity and response to immunotherapy. *Cancer Immunol Immunother*

66, 1037-1048 (2017).

133. N. Nagarsheth, M. S. Wicha, W. Zou, Chemokines in the cancer microenvironment and their relevance in cancer immunotherapy. *Nat Rev Immunol* **17**, 559-572 (2017).
134. K. Wolf *et al.*, Collagen-based cell migration models in vitro and in vivo. *Semin Cell Dev Biol* **20**, 931-941 (2009).
135. K. Wolf *et al.*, Physical limits of cell migration: control by ECM space and nuclear deformation and tuning by proteolysis and traction force. *J Cell Biol* **201**, 1069-1084 (2013).
136. R. Basu *et al.*, Cytotoxic T Cells Use Mechanical Force to Potentiate Target Cell Killing. *Cell* **165**, 100-110 (2016).

초록

장기모사칩은 2000년대 초부터 마이크로 공정 기술이 생물학적 연구에 활용됨에 따라 인간 장기 기능을 모사하기 위해 개발되었다. 구체적으로, polydimethylsiloxane (PDMS) 기반 미세유체 장치는 공간적으로 구분된 세포 패터닝을 가능케 함으로써 생체와 유사한 구조로 세포를 배양할 수 있게 해주었다. 이러한 세포 패터닝은 페트리 디쉬, 플라스크, 혹은 웰플레이트와 같은 기존의 세포 배양 도구에서는 수행하기 어려운 삼차원 세포 배양과 그 안에서의 시공간적 분석을 가능하게 하였다. 하지만, 종래의 장기모사칩은 PDMS에 기반한 닫힌 형태의 채널 설계로 인해 낮은 생산성, 낮은 실험 효율, 낮은 장비 호환성을 갖는다. 따라서, 본 연구는 대중적인 세포 배양 장치들에 마이크로 구조물을 통합한 두가지 모세관 현상 기반의 패터닝 방법을 제시한다. 첫번째 방법은 페트리 디쉬나 polystyrene (PS) 필름과 같이 개방된 PS 표면에 마이크로 기둥 어레이를 제작하여 그 위에서 액체가 쓸려 지나갈 때 기둥 구조물들 사이에 액체를 포획하는 방식이다. 마이크로 기둥 어레이의 배치에 따라 나노리터부터 마이크로리터에 이르는 액체를 빠르게 패터닝할 수 있게 한다. 이러한 기둥 구조를 활용하면 다양한 세포의 배치 및 배양이 가능하여, 본 연구에서는 삼차원 환경에서의 단일세포 배양과 다세포 공배양 플랫폼으로의 활용 가능성을 제시하였다. 두번째 방법은 마이크로 레일 형태의 마이크로구조물을 표준화된 마이크로 플레이트의 웰과

통합하여 고효율 삼차원 배양 플랫폼을 제시한다. 레일 구조의 아래에 주입된 액체가 빨아들여질 때 구조물에 의해 형성된 액체-기체 계면들의 순차적 이동을 활용하여 특정 레일의 아래에만 액체를 남기는 기술을 개발하였다. 이 두가지 모세관 현상 기반 패터닝 방법을 위한 장치들은 사출성형으로 대량생산이 가능하고 우수한 실험 효율을 갖는다. 이 중 레일 구조를 활용한 흡인 기반의 패터닝 방법을 이용하여 면역세포치료제의 성능 평가를 위한 사출 성형된 플라스틱 어레이 배양 장치(CACI-IMPACT)를 개발하였다. 흡인 기반 패터닝 덕분에 20 μl 파이펫으로 빨아들인 하이드로젤 용액을 30 초 이내에 12개의 웰에 패터닝 할 수 있었다. 면역세포치료제의 기능적 평가를 위해, 콜라겐 젤에 포함된 HeLa 세포를 패터닝하고 NK-92 세포의 콜라겐 매트릭스 내부로의 침투, 매트릭스 내부에서의 이동 및 암세포 살해 활동을 관찰하였다. 이를 통해 세포외기질이 세포 독성 림프구의 이동 및 세포 독성에 상당히 영향을 미친다는 것을 확인할 수 있었다. 따라서, 암세포와 세포 독성 림프구의 고효율 삼차원 공동 배양을 가능하게 하는 본 플랫폼은 고형 종양에 대한 면역 치료를 위해 개발된 세포 독성 림프구의 전임상 평가에 사용될 가능성이 있으며, 본 연구에서 개발 및 사용된 모세관 현상 기반 패터닝 기술들은 장기모사칩의 상용화를 가속화시킬 것으로 기대한다.

공학박사학위논문

모세관 현상 기반의 패터닝 기법을 활용한 고효율 삼차원 면역세포 항암효능 평가 플랫폼

Capillarity Guided Patterning Based High-throughput 3D Immune Cell Cytotoxicity Assay

2020 년 8 월

서울대학교 대학원
기계공학부
박 도 현

모세관 현상 기반의 패터닝 기법을 활용한 고효율 삼차원 면역세포 항암효능 평가 플랫폼

Capillarity Guided Patterning Based High-throughput 3D Immune Cell Cytotoxicity Assay

지도교수 전 누 리

이 논문을 공학박사 학위논문으로 제출함
2020 년 4 월

서울대학교 대학원
기계공학부
박 도 현

박도현의 공학박사 학위논문을 인준함
2020 년 6 월

위 원 장 김 호 영 (인)

부위원장 전 누 리 (인)

위 원 신 용 대 (인)

위 원 도 준 상 (인)

위 원 조 덕 (인)

Abstract

Organs-on-chips have been developed for recapitulating human organ functions in *in vitro* as microfabrication techniques meet biology since the early 2000s. Specifically, polydimethylsiloxane (PDMS) based microfluidic devices enabled to mimic organ functions by providing spatially compartmented cell patterning for culturing cells with *in vivo* like layout. The selective cell patterning enabled 3D cell culture and spatiotemporal analysis which were challenging to conduct with conventional cell culturewares such as petri-dishes, flasks, and well-plates. However, traditional organs-on-chips have limitations in salability, experimental throughput, and absence of standard due to their closed channel designs based on PDMS. Here, we introduce two capillarity guided patterning (CGP) methods by integrating microstructures with conventional cell culturewares. First, we fabricated micropillar arrays on open polystyrene (PS) surfaces and the micropillars can capture liquids swept over the surface. Using the devices, we demonstrated 3D culture applications, single cell capturing and retrieval and multiple cell co-culture. Second, we integrated rail-structures with microplate. Beneath a rail-structure, hydrogel precursors can selectively remain according to meniscus dynamics when the pre-loaded precursors are aspirated. These two CGP methods can be produced with injection

molding and provide enhanced experimental throughput. Using the rail-based CGP method, we developed a 3D cytotoxicity assay for cancer immunotherapy based on an injection molded plastic culture (CACI-IMPACT) device to assess killing abilities of cytotoxic lymphocytes in 3D microenvironment through a spatiotemporal analysis of the lymphocytes and cancer cells embedded in 3D extra cellular matrix (ECM). Owing to the aspiration-mediated patterning, hydrogel precursors can be patterned in 12 wells within 30 s. For functional evaluation of the cytotoxic lymphocytes engineered for cancer immunotherapy, HeLa cells encapsulated by collagen matrix were patterned beneath low rails and NK-92 cells were loaded into the channel formed by the collagen matrix. We observed infiltration, migration and killing activity of NK-92 cells against HeLa cells in collagen matrix. Through image-based analysis, we found ECM significantly influences migration and cytotoxicity of lymphocytes. Hence, the CACI-IMPACT platform has the potential to be used for pre-clinical evaluation of *ex vivo* engineered cytotoxic lymphocytes for cancer immunotherapy against solid tumors, and the CGP methods are expected to accelerate the commercialization of organs-on-chips.

Keyword : organ-on-a-chip, high-throughput screening, liquid patterning, open microfluidics, cancer immunotherapy, 3D cytotoxicity assay

Student Number : 2015-20697

Table of Contents

List of Figures

Chapter 1. Introduction

1.1. History of organs-on-chips

Since the advent of polydimethylsiloxane (PDMS), a number of microfluidic devices have been introduced in biological and chemical research field such as diagnostic devices (*1*), chemical gradient generators (*2*), nanoparticle synthesis (*3*), and particle separators (*4*). Especially, PDMS-based devices brought great improve in cell biology due to its characteristics favorable for cell culture. Gas permeability of PDMS enables long term cell culture and transparency of PDMS facilitates observation of cultured cells within the PDMS-based devices (*5*). Most of all, molding microstructures with PDMS revolutionized cell-based studies that were challenging with conventional labwares. For example, microwell devices facilitated studies of heterogeneity of cells and deformation of micropillar array enabled analyzing distribution of forces applied by a single cell (*6, 7*).

Organ-on-a-chip is one of the most successful applications utilizing the characteristics of PDMS advantageous for cell-based studies. Huh et al. opened the era of organ-on-a-chip as they recapitulate organ-level function by utilizing the characteristics mentioned so far (*8*).

Furthermore, hydrophobicity of PDMS enables micro-pores to work as capillary bursting valves that facilitate to arrange cells into physiologically relevant layouts (*9*). Along with the hydrophobicity, elasticity of PDMS allows to apply mechanical stimulation to the cultured tissue so that the device can mimic stretching and relaxation of the lung. Since the lung chip has shown the possibility of recapitulating organ-level function in microfluidic devices, a number of microfluidic devices have been developed, mimicking diverse organ functions such as blood-brain barrier (*10*), gut (*11*), bones (*12*), airways (*13*), and kidney (*14*). Following the development of organ units, there were trials to integrate of the organ chips. In 2014, NIH funded 11 institutions to do the work and DARPA entered into cooperative agreements with NIH award recipients to develop platforms capable of integrating 10 or more organ systems. As a result of the projects, Edington et al. reported interconnected microphysiological systems (MPS), or organs-on-chips, by integrating 4, 7, and 10 MPSs for pharmacological testing (*15*). Although they showed the possibility to connect multiple organ chips and to analyze drug response, they discussed that quantitative analysis is challenging as the number of interconnected MPSs increases. Furthermore, diverse cell sources, culture medium, control of flow rate

make the multi-MPS system difficult to be realized and used by researcher other than the developers. The hurdles in developing multi-organ chip systems has led the trend of organ chip research to develop disease models that are specific applications with a single organ chip. In 2016, NCATS announced a funding opportunity as part of the tissue chips for disease modeling and 13 institutions were funded to develop disease models such as Parkinson's disease, inflammation in muscle, vascular malformations, etc.

Along with the change of research trend and technical improvement in organ chip field over a decade, the field has been matured to commercialization. Emulate spun out from Wyss institute supports kidney, liver, and intestine chips and hardware for manipulating the chips efficiently. They also provide services to execute studies utilizing the chips as customer wants such as toxicity test and drug efficacy test. As their devices are made with PDMS which is challenging to make scalable, they are developing manufacturing systems and enhancing experimental throughput by utilizing hardware. Tissuse is a german company where has profound experience in multi-organ chip devices. Their four-organ (intestine, liver, skin, and kidney) chip demonstrated long-term co-culture of the organs for up to 28 days (*16*).

Instead of using gravity driven flow, they utilize a built in micropump driven by an external pneumatic controller. For the pneumatic control, their device utilizes a thin PDMS film. To address limitations in manufacturing of microfluidic devices using PDMS, some companies develop plastic-based microfluidic chips. Mimetas is a representative company developing well-plate formatted devices produced with thermal plastic. Using their multi-lane devices several research groups reported organ models such as kidney proximal tubule (*17*), blood-brain barrier (*18*), gut (*19*), and glomerular filtration barrier (*20*). Unlike premature era of microfluidics when most of the articles were reported by inventors, recent articles using devices from Mimetas show that commercialized microfluidic devices are widely used by biological researchers.

1.2. Challenges in current organs-on-chips

As commercialized organ chips are used by biologists, pharmaceutic companies, and medical researchers, their usefulness should be verified for prosperity of the market. In order to be used for screening systems in development process of drugs or cosmetic products,

not to be a single time use for novelty in research, some challenges remain to be addressed.

First, improvement in manufacturing process is needed. Making devices with PDMS is time consuming and requires intensive labor. Normally, the fabrication process consisting of PDMS molding, cutting, punching, and plasma bonding takes 1-2 hours and recovering hydrophobic surface after plasma bonding requires one or more days if the device utilizes the hydrophobic surface for cell patterning (*21, 22*). Hence, many organ chip companies produce their products with thermal plastics which are scalable via injection molding.

The second problem is low experimental throughput. Even though they changed material, most of the devices keep using cell patterning methods that utilize capillary bursting pressure between narrow gaps formed by micropillars or microbumps (*23, 24*). As critical capillary pressure at narrow gaps depends on the hydrophibicity of the surface, thermal plastics have smaller critical capillary pressure than PDMS. The lowered critical capillary pressure in plastic devices induces larger patterning failure rate as users can easily exceed the pressure if they are not sufficiently trained. Even though they are skillful for the

patterning process, sophisticated pressure control is required which limits automation of the loading process.

For the last, absence of standard in size and shape causes inefficiency in maintenance and analysis (*25*). Even though a number of organ chip devices have been developed for a decade, there is no standard for their sizes and formats. It means that each device requires customized setup for cell culture and analysis. Furthermore, the variety in designs is not familiar with researchers who do not have experience in microfluidics so that it hinders introducing organ chips to potential users. Berry et al. reported inserts for well-plates generating rail-structure that can work as microfluidic channel (*26*). The article showed the possibility for microfluidics to be combined with conventional cell-culture products which are widely used and compatible with automated equipment. However, commercialized microfluidic devices still have their own formats and the companies develop equipment for handling the microfluidic devices.

It is believed that the limitations are originated from closed channel designs based on PDMS-glass bonding whose opening exist only at inlet/outlet ports. Even though Aim biotech produces microfluidic devices with injection molding (*27*), its experimental

throughput varies with users' skills due to lower hydrophobicity of plastic compared with PDMS. Hence, to address all the limitations, a new approach in design, material selection, fabrication method, and patterning method is required.

1.3. Models for cancer immunotherapy

Cancer immunotherapy is a new approach to treat cancers by increasing cytotoxic capability of patient's immune system against cancer cells. Programmed death-ligand 1/programmed death-1 (PD-L1/PD-1) blockade is one of the most representative therapies of cancer immunotherapy. The blockade enhances recognition of cancer cells by T cells as non-self, inducing cytotoxic activity of T cells against cancer cells. This approach significantly enhanced long-term survival rate compared with conventional therapies such as targeted therapy and chemotherapy (*28*). The great success of immune checkpoint inhibitors led the inventors, Tasuku Honjo and James Allison, to receive the 2018 Novel prize in physiology or medicine.

As the efficacy of immune checkpoint inhibitor is verified and the market share is growing, a number of immunotherapy drugs are developed and are under clinical trials (*29*). The intensive development

of immunotherapy drugs has increased the demand for screening models in the preclinical stage (*30*). Mouse models takes the major position in preclinical studies, however, the immune system reconstituted in mice cannot elucidate the one in the human body even though human immune cells are transplanted (*31*). Furthermore, tumor-immune microenvironment (TIME) consisting of cancer cells, fibroblasts, lymphocytes, and macrophages, is hardly maintained in mouse models. Hence, a need for pre-clinical model recapitulating anti-tumor immune system exists.

1.4. Purpose of Research

In previous chapters, limitations in commercialized organ chip devices and demand for preclinical models screening immunotherapy drugs are introduced. In this thesis, we will introduce two capillarity guided patterning (CGP) methods to address the aforementioned limitations of conventional organs-on-chips. Using CGP, we will introduce a 3D cytotoxicity assay platform for evaluating cell-based cancer immunotherapy. For the CGP methods, microstructures will be integrated with conventional cell culturewares, petri-dish and well-plate, which provide open culture environment. To enhance productivity, we

utilized plastics which can be mass produced via injection molding. In order to enhance experimental throughput, we developed automated patterning system (chapter 2) or simple patterning process (chapter 2 and 3). Lastly, as we utilize standardized culturewares, petri-dish and well-plate, the platforms are compatible with conventional automated equipment such as automated dispensers or automated imaging systems. We believe overall improvement in production, usability, and standardization will maximize the versatility of organ chips, which will lead organ chips to success in the market, not just in the research stage.

In chapter 2, we introduce a fast multiscale microliquid-patterning method on an open surface using embossed microstructures without surface modification for the first CGP method. Arrays of micropillars can trap microliquids when a bulk drop is swept by an elastic sweeper on polystyrene (PS) substrates such as petri-dishes. In chapter 3, we present a swift and robust hydrogel patterning technology, where preloaded liquid in a microfluidic device is aspirated while leaving the only desired section of liquid for the second CGP method. The device is designed such that differing critical suction pressure conditions are established over the interfaces of the loaded gel, which leads to controlled removal of the liquid as negative gage pressure is applied.

In chapter 4, we present a high-throughput 3D cytotoxicity assay platform using the design introduced in the chapter 3. Rail-based microfluidic design was integrated within a single 96-well and the wells were rectangularly arrayed in 2 × 6 to enhance the experimental throughput. The 3D cytotoxicity assay for cancer immunotherapy using an injection molded plastic array culture (CACI-IMPACT) device can assess killing abilities of cytotoxic lymphocytes in 3D microenvironment through a spatiotemporal analysis of the lymphocytes and cancer cells embedded in 3D extra cellular matrix (ECM).

Chapter 2. Microstructure-guided multi-scale liquid patterning on open surface

2.1. Introduction

Cell-based screening is an important aspect of research in a variety of fields. Many miniaturized cell-based assays have been introduced since the development of microliquid manipulation techniques. Robotic printing of microdroplets enabled fabrication of cellular microarrays for high-throughput screening of small molecules (*32, 33*), genomic libraries (*34-36*) and have aided in the study of extra cellular matrices (ECM) to cellular differentiation (*37*). Although cellular microarrays have reduced the resource requirements of screening, this method is limited to screening of adherent cells in a 2D environment, and requires complicated fabrication processes. Droplet microfluidics-based technologies seek to address the limitations of earlier 2D cellular microarray techniques. Droplets containing cells are produced with ultra-fast frequency up to kHz when cell suspension and oil meet at a T-junction of a microfluidic channel. High-throughput screening (HTS) utilizing encapsulated droplets are capable of both single cell based

screening (*38-40*), and multi cellular spheroid screening (*41, 42*). However, droplet encapsulation requires sophisticated instrumentation to control the two immiscible liquids precisely. Moreover, additional observation and control systems are required for the separation of discrete droplets, and sample recovery from separated droplets is more difficult due to rinsing steps (*43, 44*).

Recently, a one-step droplet patterning method, droplet array plate was proposed for cell-based studies (*45*). Partition of hydrophobic and hydrophilic surface regions induces separation of droplets from a bulk drop. The droplet microarray device was applied to a study of cell-cell interaction (*46*), 2D co-culture (*47*), and fabrication of cell-laden hydrogel particles (*48*). Although these platforms are capable of quickly and easily patterning droplets in a single step, the utilization of super-hydrophobic and super-hydrophilic materials necessitates a more difficult and expensive production process for the plate itself in comparison to single substrate platform proposed here.

In this study, we introduce a new liquid-patterning method, which utilizes simple micropatterned pillar arrays on a flat substrate. The microstructures enhance shear force applied to a liquid drop. When driven by an elastic sweeper, bulk liquids are trapped and retained as

small droplets inside area cornered by microstructures. A succeed of liquid patterning was determined by dimensionless parameters and they were validated experimentally. The subsequently derived designs were then applied to single cell screening and 3D co-culturing experiments. This liquid patterning method is: (i) simple and fast, (ii) easily accessible to sample, (iii) able to capture microliquids with high aspect ratios, and (iv) adaptable to various wettability of substrates.

2.2. Materials and Methods

2.2.1. Fabrication of the microstructured PS surface

To fabricate microstructures on polystyrene surfaces, solvent-assisted molding was used as shown in Figure 2.1 (*49*). A negatively micropatterned polydimethylsiloxane (PDMS) mold replica, fabricated with conventional soft lithography, was used as a template. First, the solvent (AZ 1500 Thinner, AZ Electronic Material, Germany) was applied to the micropatterned base of the PDMS mold via immersion. The solvent-wetted PDMS mold was then carefully applied to a PS substrate surface in a reverse peeling motion. Once the solvent-wetted PDMS mold was applied to the

PS surface, the assembly was placed on a 65℃ hotplate for 30 minutes to evaporate the volatile solvent and to cure the molded PS substrate. At this time, the solvent on the PDMS mold surface dissolved the PS surface and rearranged the dissolved PS solution inside the micropatterned grooves of the mold. Upon evaporation, the solvent deposited the dissolved PS in the shape of the negative PDMS micropatterns, leaving a positively structured PS surface. After curing, the PDMS mold is detached from the now embossed substrate. For the cell culture, the newly patterned PS surface was ventilated for three days in room conditions to remove any residual solvent.

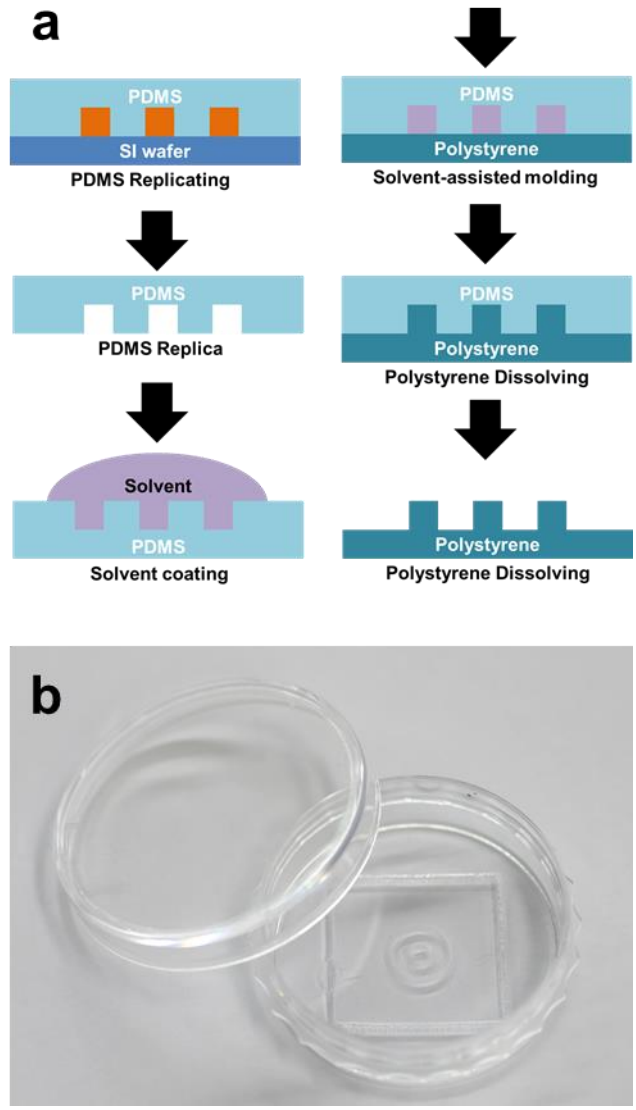

Figure 2.1. (a) Schematic diagram of solvent-assisted molding. (b) A petri-dish with microstructures molded via solvent-assisted molding. Micropillars are molded with concentric doughnut-shapes on a conventional 35 mm diameter petri-dish. *In vitro* blood vessel vasculogenesis was demonstrated with this device.

2.2.2. Single cell isolation and retrieval of single colony

A wild-type CC-124 strain and a mutant strain with the GFP gene CC-4488 (D1blic::D1bLIC-GFP, Chlamydomonas center) were prepared at a concentration of 0.7 x 10^6 cells/ml. The two cell suspensions were mixed at a 1:1 ratio and the mixture was then mixed with a 4% alginic acid sodium salt (Sigma) solution at a 1:1 ratio again. A cell suspension with a density of 0.35 x 10^6 cells/ml in the 2% alginic acid sodium salt solution was formed as a result. The cell suspension was patterned on an embossed dish for a single-cell analysis and polymerized with a 2% $CaCl_2$ solution. After 10 seconds of polymerization, the solution was replaced with TAP medium. The patterned cells were then cultured for two days.

For recovery of the colonies, the medium was drained and 2 μl of a 0.2 M EDTA solution was introduced above the patterned alginate gel. After 10 seconds, the mixture of the degraded alginate gel and the EDTA solution was retrieved with a micropipette and applied onto an agar plate with a TAP+N medium. The colony was cultured for seven days again to increase its population, and it was genetically verified whether the strain was the mutant or the wild type. The CrGFP plasmid, CC-4488 (D1blic::D1bLIC-GFP) strain

and CC-124 (137c mt–) strain were from CC-124 (137c mt–)r, and the genomic DNA of these strains was extracted by the traditional PCI (Phenol : Chloroform : Isoamyl alcohol (25:24:1 v/v)) method. Subsequently, 20 ng of each sample was amplified by i-Taq with Maxime PCR PreMix Kits (iNtRON Biotechnology, Cat. No.: 25035) using 10 pmole of GFP gene-specific primer pairs, a forward primer (5'-GACGGCAACTACAAGACCC-3') and the corresponding reverse primer (5'-TGTACACGTTGTGGGAGTTG-3'), with 40 cycles at 95℃ for 20 seconds, at 56℃ for 20 seconds, and at 68℃ for 25 seconds. The PCR product of 148 nts was separated by 2.0% agarose gel electrophoresis.

2.2.3. *In vitro* vasculogenesis

Human umbilical vein endothelial cells (HUVECs, Lonza) were cultured in an endothelial growth medium (EGM-2, Lonza) and passaged from 4 to 7. Normal human lung fibroblasts (LFs, Lonza) were cultured in a fibroblast growth medium (FGM-2, Lonza) and passaged from 6 to 9. All cell types were maintained at 37°C in 5% CO_2 in a humidified incubator. The HUVECs and LFs

were then detached from the culture dishes, centrifuged for two minutes at 1100 rpm and suspended at a concentration of 6.67 x 10^6 cells/mL in EGM-2. Fibrinogen powder from bovine plasma (F8630, Sigma-Aldrich) was dissolved in phosphate-buffered saline (PBS, Hyclone) and with 0.45 U/ml of aprotinin (A1153, Sigma-Aldrich) added to create a fibrinogen solution with a concentration of 10 mg/ml. The prepared fibrinogen solution and cell suspension were then mixed at a 1:3 ratio, finally creating solutions of HUVECs and LFs with fibrinogen concentrations of 2.5 mg/ml and cell densities of 5 x 10^6 cells/ml. The mixture of HUVECs was then mixed with thrombin at 50 U/ml (T4648, Sigma-Aldrich) at a volume ratio of 50:1 and quickly dropped uniformly on a patterned petri dish as soon as the mixing was done. The mixture was gently swept with a PDMS block to ensure that the gel solution was evenly dispersed and to have the pillar arrays trap the gel with cells. After three minutes for the gel to be polymerized, the mixture of LFs was introduced to fill the area guided by the previously patterned gel. EGM-2 was applied to fill the petri dish again after three minutes. The samples were cultured in a humidified incubator at 37℃ with 5% CO_2 for five days. The

medium was replaced with fresh medium on the third day by gently suctioning the old medium from the edge of the dish while not touching the microstructures where the gel was trapped.

2.2.4. Visualization of *in vitro* blood vessel

After fixing the samples with 4% paraformaldehyde buffered in PBS for 15 minutes, they were treated for 20 minutes with 0.15% Triton X-100 (Sigma) for permeabilization and one hour with bovine serum albumin (BSA, Sigma) to block nonspecific binding. To visualize the blood vessel networks, the samples were incubated with a mouse monoclonal antibody specific for human CD31 (AlexaFluor®488 conjugated, BioLegend) overnight at 4˚C. DNA was stained using Hoechst 33342 (Molecular Probes) for one hour at room temperature. For the z-projection of the 3D blood vessels, stained samples were imaged with an Olympus FV1000 confocal microscope using a 10x objective lenses. To display the vessel network patterned in large areas, the images from each field of view were captured and stitched using software.

2.3. Results and Discussion

2.3.1. Liquid patterning process

Liquid patterning process can be divided into two steps, infiltration and retention, as shown in Figure 2.2. First, liquid should infiltrate into the area cornered by the pillars. Physical conditions to determine whether infiltration would occur spontaneously on arrays of micropillars were studied on the basis of thermodynamic arguments (*50, 51*). Theoretical studies of the dynamics of infiltration process were reported (*52, 53*). If infiltration is not energetically favored, however, the structure will pin the meniscus and form an air pocket as illustrated in Figure 2.3a. Even in such a case, liquid can still be squeezed into the gap by applying additional pressure. In this study, the additional pressure is applied as a bulk liquid is swept by a PDMS block.

Retention corresponds to the separation of a targeted volume of liquid from a bulk liquid. The shear force acting on the liquid by the surrounding solid structures induces deformation and eventual separation (*54*). The critical speed of separation is known to decrease by using microstructures (*55*) and hydrophilic chemical treatments (*45*).

In this work, micropillars on PS plates formed by solvent-

assisted microcontact molding enhance the shear force to break up the liquid into tiny droplets. A minimal unit of the pattern is a 2X2 rectangular array of circular pillars. We sweep the liquid by moving the substrate with a velocity of U=30 mm/s relative to an elastic sweeper, using a prototype of automatic patterning system (Figure 2.4). We investigate whether the patterning scheme works as geometric parameters of the microstructures are changed: the height of pillars, h, ranges from 50 to 200 μm, and center-to-center distance, l, ranges from 130 to 410 μm. In addition, we test with various liquids of different viscosity, μ, and surface tension coefficient, γ. The physical properties of the liquids with critical advancing and receding contact angles, θ_{A} and θ_{R}, on the PS plate were measured with Smartdrop (FEMTOBIOMED.inc, Korea) as listed in Table 1.

We now consider the mechanical condition to cause infiltration of the liquid into the area cornered by the four pillars of diameter, d=100 μm, as shown in Figure 2.3a. For the liquid to replace the air pocket, an interface straddling the pillars spaced by l should meet the neighboring interface. When the interfaces advancing into the empty area with the advancing contact angle θ_{A} touch each other, the curvature is calculated to be $\kappa = 2\sin(\theta_{\mathrm{A}} - \pi/4)/\left(\sqrt{2}l - d\right)$. Then the Laplace pressure of

the given configuration is given by $\gamma\kappa$. The pressure of the liquid relative to the atmospheric gas pressure, which is scaled as $\sim\gamma/L$ with L being the characteristic thickness of the bulk being swept, should be strong enough to generated the foregoing Laplace pressure to enable the merging of the interfaces. Therefore, the dimensionless parameter that determines whether the liquid fills the area cornered by the pillars is given by the ratio of the two relative pressures, γ/L and $\gamma\kappa$:

$$\Pi_{\text{infiltration}} \sim \frac{(\sqrt{2}l-d)}{2L\sin\left(\theta_{\text{A}}-\frac{\pi}{4}\right)} \qquad (1)$$

This consideration only holds for the advancing contact angle higher than 45°. Otherwise, the liquid spontaneously fills the volume between the microstructures because of the concave curvature of liquid-air interface. If the center-to-center distance between the pillars, l, is large, the liquid easily fills the patterning area. Our experimental results with the thickness of bulk liquid fixed at $L \approx 2.6\,\text{mm}$ are plotted in Figure 2.3b, which clearly shows that whether the infiltration succeeds or fails is determined by the value of $\Pi_{\text{infiltration}}$.

To achieve successful retention, the bulk liquid should shed a tiny droplet as retained by the pillars (Figure 2.3a). If the liquid that used

to fill the patterning area is dragged with the bulk, the patterned area is re-occupied by the air. Since the retention behavior is critically dependent on whether the viscous shear force exerted by the sweeper exceeds the capillary force that tends to keep the drop intact, we introduce the ratio of the viscous force to capillary force, the Capillary number, $\mathrm{Ca} = \mu U/\gamma$. The viscous force in the liquid consists of the forces acting at the bulk and near the contact line (*56*). For a liquid trapped in the space cornered by the pillars with the aspect ratio $h/(l-d) \sim 1$, the viscous force near the contact line dominates that in the bulk (*57*). Integrating the shear stress in the wedge-shaped region near the contact line with the receding contact angle θ_{R}, we obtain the scaling estimate of the shear force as $\sim \mu U(l-d+2h)\cot\theta_{\mathrm{R}}$. This estimate is valid for $\theta_{\mathrm{R}} < 90^{\circ}$, which is the case for most surfaces except for superhydrophobic ones. The capillary force that resists the shearing is scale as $\gamma(l-d)$. Therefore, the boundary whether the liquid that has filled the patterning area would be retained is given by the ratio of the foregoing forces:

$$\Pi_{\mathrm{retention}} \sim \left(1 + \frac{2h}{l-d}\right) \mathrm{Ca}\cot\theta_{\mathrm{R}} \qquad (2)$$

Denser and higher pillars lead to higher $\Pi_{\text{retention}}$, which facilitates the retention of the droplets in the patterned area. Figure 2.3b shows that the experimental conditions having the value of $\Pi_{\text{retention}}$ higher than a critical value lead to successful retention while those with lower values fail.

We also verified the patterning regime with lower values of surface tension and contact angle by mixing surfactant (TX 100) that result in larger dimensionless numbers. As we expected, small droplets were separated from bulk drop in all cases (Figure 2.5). However, the microliquids were not pinned as the initial shape in higher density of surfactant. This may allow the adjacent droplets to merge, but the merging of droplets cannot happen in applications for cell-based assay because the PS surface and water-based solutions have larger contact angles and surface tension coefficients.

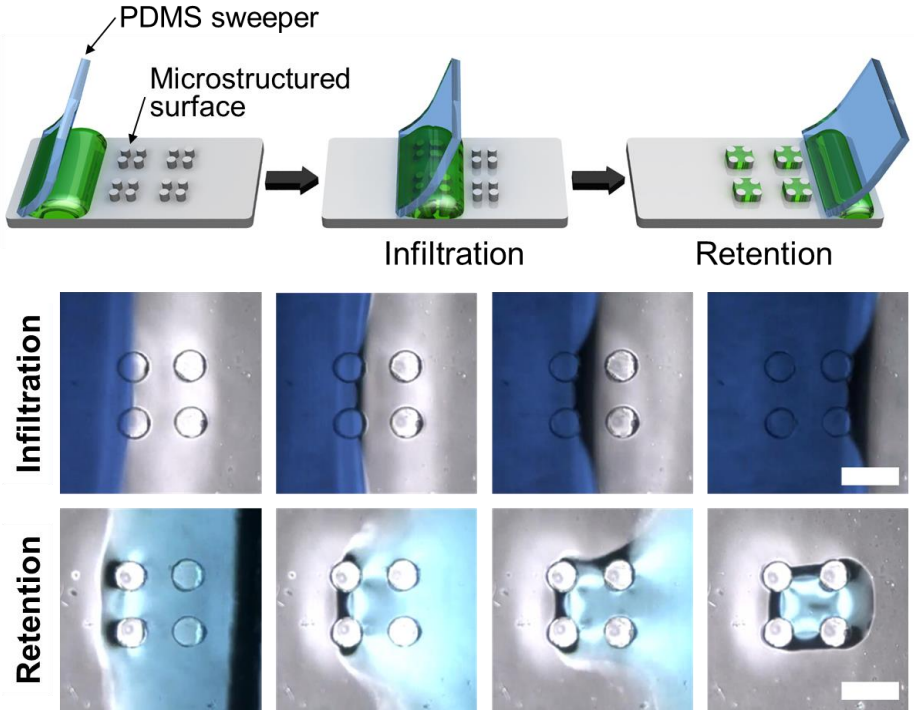

Figure 2.2. Process of the microstructure-mediated liquid patterning on a positively structured surface. A bulk drop, swept by an elastic sweeper, leaves small droplets in the patterning area cornered by the microstructures. The liquid patterning process consists of two steps: infiltration and retention. Scale bar: 200 μm.

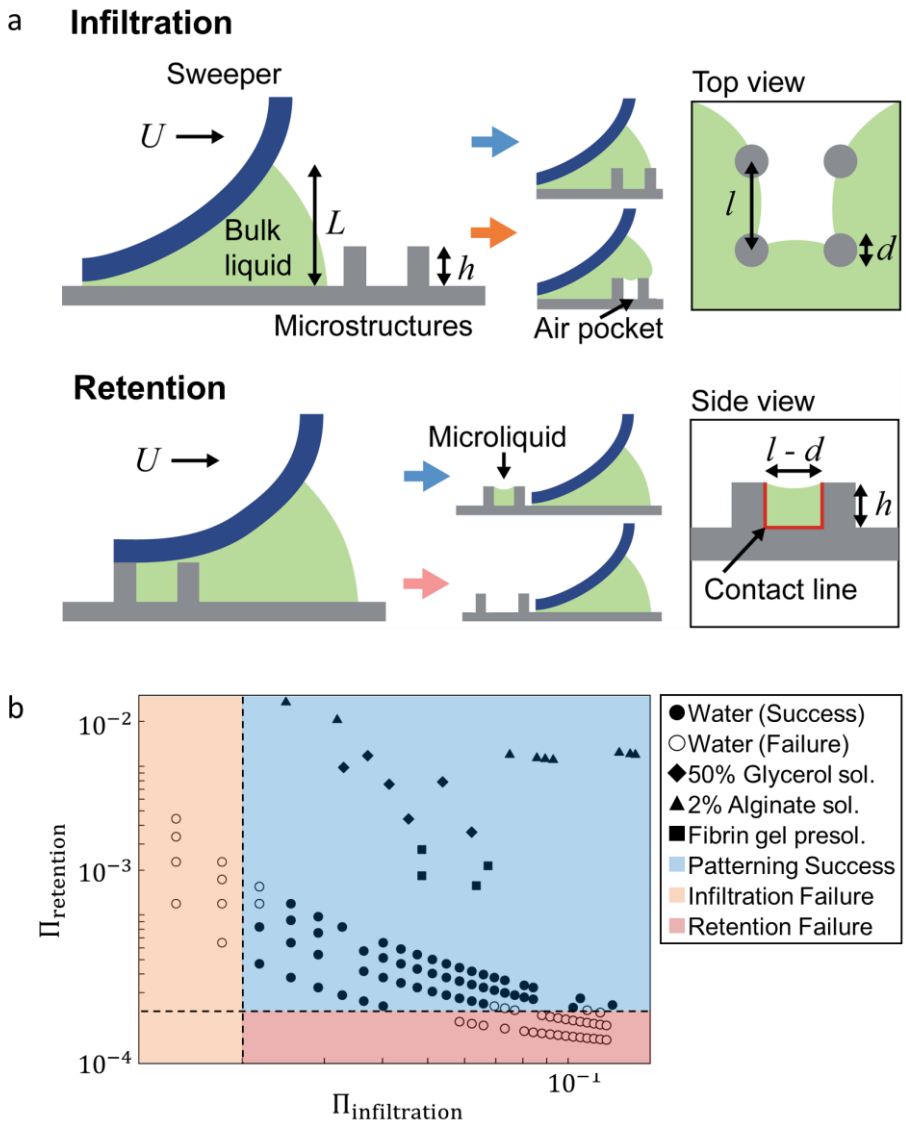

Figure 2.3. The effect of liquid properties and geometries to the liquid patterning process. (a) A schematic demonstration of the success and failure of the two patterning processes. (b) Results obtained from the dimensional analysis are plotted on a graph with axes of dimensionless numbers. To succeed, both of the dimensionless numbers $\Pi_{infiltration}$ and $\Pi_{retention}$ must exceed the value of the boundaries.

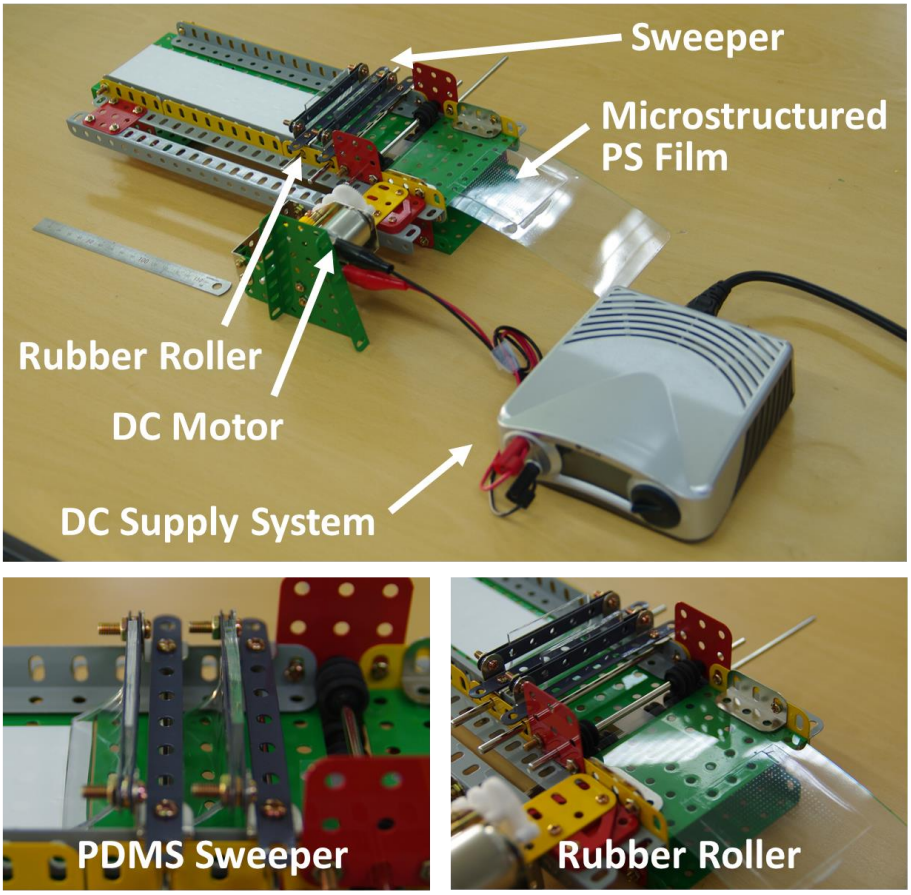

Figure 2.4. A prototype of automatic sweeping system. The rubber roller transports a micropatterned PS film under a fixed PDMS sweeper. This system provides stable sweeping speed and uniform contact between the sweeper and the film.

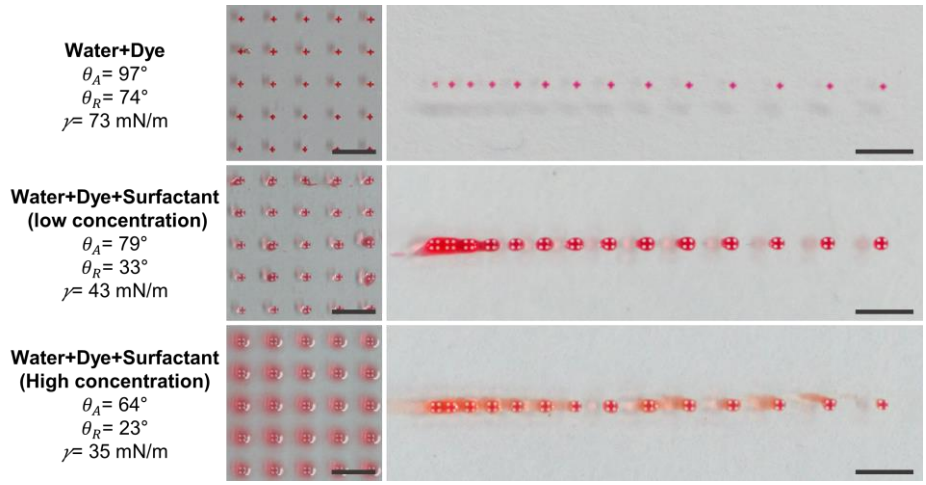

Figure 2.5. Result of droplet patterning with liquids having various contact angles on PS surfaces and surface tension coefficient. The droplets deform to lower surface energy after retention. In the right figures, the patterning spots are arrayed with spacing ranging from 300 μm to 1500 μm. Closely patterned droplets merged when the liquid has low contact angle and surface tension coefficient. Triton X 100 was added to dyed water as surfactant with volume ratio of 0.008% and 0.02% for low and high concentration condition, respectively. The height of pillars is 100 μm and scale bar is 2 mm.

Liquid	Surface tension [mN/m]	Viscosity [mPa·s]	Advancing/receding contact angle [°]
Water	72.9	0.853	92.8/72.9
50% aqueous glycerol solution	57.0	4.66	85.8/51.3
2% alginate solution	58.0	26.8	94.4/61.0
Fibrin gel pre-solution	57.2	1.33	91.4/37.2

Table 1. Physical properties of the liquids used in the experiments

2.3.2. Comparison of microliquid trapping with a micropillar array and microwells

Microwell devices are similar to micropillar arrays in that both mechanisms utilize surface microstructures. Microwells are one of the most widely used platforms for single cell studies such as selection of hydrodoma (*58*), screening of circulating tumor cells (*59*), DNA damage analysis (*60*), and genome sequencing of single cells (*61*). The popularity of microwell devices is due to the compactness of the experimental platform with thousands of trapping wells in a substrate no larger than a glass microscope slide. Filling liquids in a microwell requires that the free surface of the liquid makes contact with the bottom of the well substrate, and failure to make contact results in a large rate of unsuccessful capture. To mitigate patterning failures, many microwell devices require hydrophilic surface treatment. In comparison, micropillar arrays have more accessible faces for fluid entry, translating to more opportunities for fluid capture. In this chapter, we will compare the patterning efficiency of both structures through dimensional studies and suggest suitable cases for each patterning method.

For a quantitative comparison of patterning with micropillar arrays and microwells, we fabricated micropillar arrays and microwells

to capture square-shaped liquids with side lengths, *w*, of 100, 300, and 500 μm, respectively. For pillar arrays, 100 μm by 100 μm square pillars were arranged at center-to-center intervals of 200 μm, which was confirmed to succeed the patterning in the previous section. Figure 2.6 shows the liquid patterning schemes on both structures and the results of the patterning by changing the height of pillars and the depth of wells from 10 μm to 200 μm. For the micropillar array, the patterning efficiency increased as the height was increased while the efficiency on the microwell decreased as the depth was increased.

The results show that micropillars are capable of capturing microliquids at higher aspect ratios than microwells. However, the positive pillar array requires long distance between each patterning area to make the patterned liquid separated perfectly. Hence, microwell devices can be used for the case that large number of samples, imaged in a single focal plane, are required while micropillar array is suitable for screening the development of cells in a 3D microenvironment as will be further discussed in this paper.

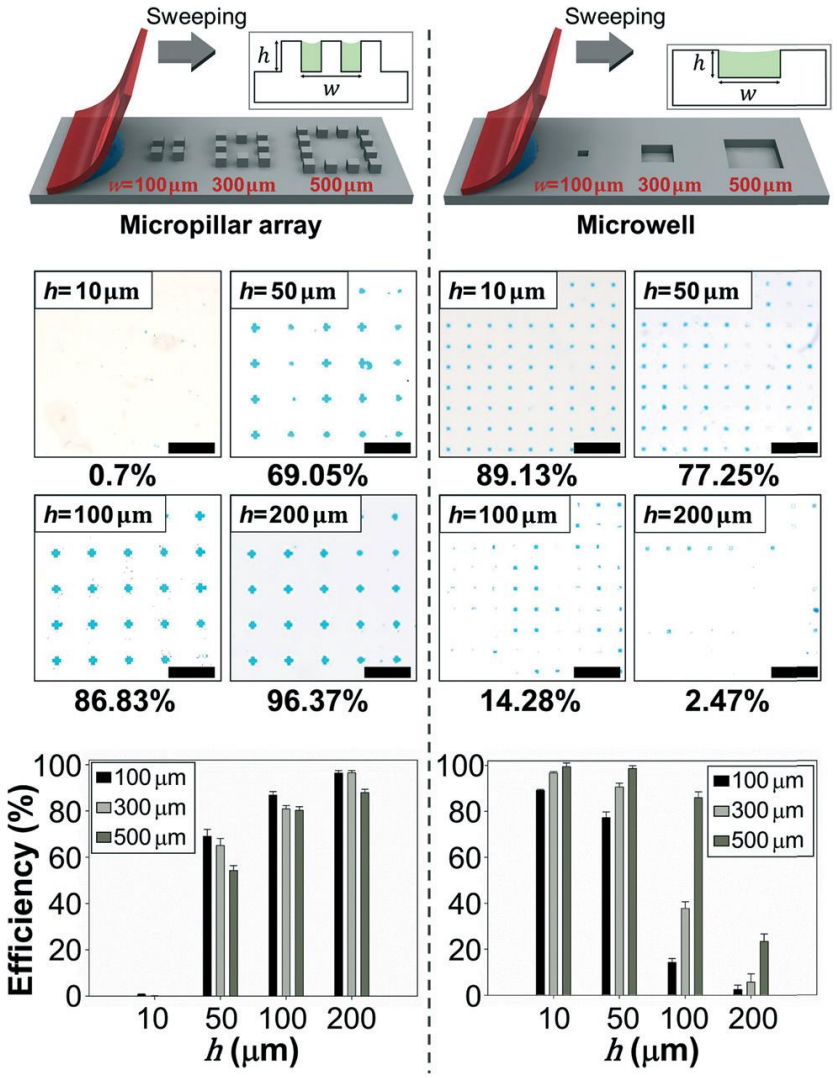

Figure 2.6. Comparison of the liquid-capturing efficiency between positive and negative structures on PS substrates without hydrophilization. The blue dyed water was swept over square pillar arrays whose center-tocenter gap is 200 μm and over microwells whose one side length is 100 μm. Taller micropillars increase the number of trapped droplets while deeper microwells decrease the number. The graphs show the same tendency when the patterning area has longer sides. Scale bar: 1 mm.

2.3.3. Arrangement of micropillars for controlling volume and shape of patterned liquids

The shape and volume of liquid can be controlled by arranging pillars in patterned arrays as shown in Figure 2.7a-e. First, the height, spacing, and number of pillars can be adjusted to control the volume of the patterned liquid. By arranging pillars at a height of 100 μm on a 2X2 array at intervals of 100 μm, water droplets can be patterned with approximate volumes of 5.5 nl. To pattern a larger volume, pillars are placed in the boundary and added inside to guide liquids. Therefore, liquids can be patterned on various scales from nanoliters to microliters. Furthermore, the patterned shape of the liquid can be determined by the arrangement of the pillars. Two rows of pillars were arranged in a curve, and it was possible to trap liquids in the designed shapes on the surface. In the case of patterning lquids in a pattern containing an acute angle, there is potential for off target liquid trapping to occur on the interior of the angle outside of the post boundaries due to the proximity of guiding posts on either side of the patterning array. Such off target liquid patterning can be avoided by incorporating a design which specifically arranges the interior arrays outside of the patterned areas to have lower values than the critical dimensionless numbers described in the chapter

2.3.1.

The shape of the micropillars itself can also be designed to control the patterning efficiency or the uniformity of patterned liquids. A patterned surface with arrays comprising of two bilaterally symmetrically facing “C” shape micropillars was compared to a surface with cylindrical four pillar arrays. It was determined that patterned arrays with a greater number of open faces, such as the 2X2 pillar configuration, resulted in a higher fluid infiltration rate while arrays with a larger contact area between captured liquids and the substrate, such as the C shape arrangements, resulted in greater uniformity of the patterned fluids. (Figure 2.7f) The method measuring volumes of the patterned liquids is described in supplementary information.

Although the basic form of 2X2 pillar array showed volume variation of 10% (CV%), the expanded forms (Figure 2.7b-d) showed smaller variation (2-5%) because most of the variation comes from the boundary of patterning area. As a whole, the proposed microstructure guided patterning mechanism resulted in droplets with a variability of volumes (<10%) comparable to other microfluid patterning techniques at the nanoliter scale: droplet microfluidics (1-3%) (*62*), inkjet printing (<3%) (*63*), electro wetting (12-17%) (*64*). Further improvements in

droplet uniformity can be achieved by controlling for environmental humidity and by refining the uniformity of the sweeping mechanism.

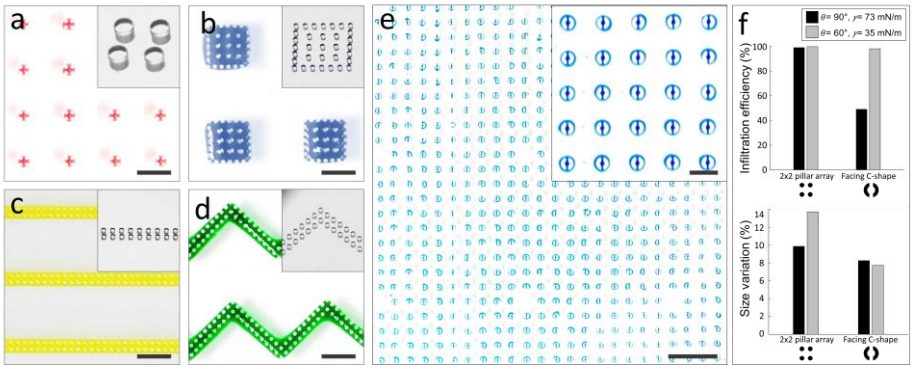

Figure 2.7. Various multi-scale liquid patterns ranging from nanoliter to microliter scale, formed on microstructure-embossed surfaces. (a–d) All pillars have heights and diameters of 100 μm and scale bars represent 1 mm. The approximate volume of each pattern is as follows: (a) 5.5 nl, (b) 140 nl, (c) 850 nl, and (d) 1.3 μl. (e) A 55 mm × 55 mm array of C-shaped pillars captured approximately 8000 droplets within a second of sweeping. Scale bar: 500 μm (magnified image), 2 mm (large area). (f) Effect of the geometry of the pillars on the patterning quality. Facing C-shaped microstructures result in a lower infiltration rate, while they enhance the uniformity of trapped liquids. The black column is DI water and the grey column is DI water with Triton X 100 (0.008%, v/v).

2.3.4. Single Cell Culture & Recovery Platform

Along with the development of microfabrication methods, a number of single-cell analysis platforms have been developed (*65-67*). However, only a few platforms enabled both of spatiotemporal analysis and retrieval of a specific cell from the isolated samples. Infrared laser mediated release of single cells trapped in microwells was introduced (*68*). A separate microchannel based device integrating single particle trap and its release using bubbles generated by IR laser was also developed (*69, 70*). These platforms require perfect alignment between the device and the laser system, and the heat generated by the laser can lower the viability of handled cells. Dielectrophoretic (DEP) force mediated single cell trap methods can capture single cells with a high success rate, but they require a complex and expensive multilayered chip with integrated electrodes and off chip circuitry (*71, 72*). Recently, a microfluidic chip for single-cell trap and selective release using pressure actuated microfluidic OR logic gate was proposed (*73*). Although this platform had high efficiency of extraction, sophisticated controls were necessary for the OR logic gate and backflow. In this chapter, we are introducing a simple single cell analysis platform on which single cells can be patterned, cultured, and retrieved without cross-contamination

between nearby colonies.

We used 2X2 rectangular arrays of circular pillars (d= 100 μm, l= 200 μm, and h= 100 μm). An array of trapping spots was molded on a petri dish with a diameter of 60 mm. Each patterning spot has a coordinate and an indicator to enable efficient screening and recovery. Alginate gel containing microalgae was patterned through a simple sweeping motion as described in the experimental section. After two days of cultivation, single colonies grown from a single microalga was retrieved, following the process of Figure 2.8a. We experimentally found the cell concentration in alginic acid solution that maximizes the portion of patterned spots having single cells. Figure 2.8b shows the distribution of cells in trapping spots according to the cell density. The portion of spots with a single cell was maximized at 32.8% when the density was 0.35×10^6 cells/ml. After two days of cultivation, the single cells grew to form colonies with a top view area of 1.31×10^{-3} mm^2 on average (n=7) (Figure 2.8c). To demonstrate the retrieval of a single colony, we patterned two types of microalgae: CC-4488, a mutant strain with green fluorescence and CC-124, a wild type. The coordinates of patterning spots possessing a single cell were recorded, and after two days, cell types were distinguished according to the presence of green fluorescence

(Figure 2.8d). Using an EDTA solution to dissolve the alginate gel, we retrieved the single colonies of both CC-124 and CC-4488 with a micropipette and the naked eye with the help of the coordinates and indicators. To verify the absence of cross-contamination during retrieval process, a genetic analysis was conducted. The extracted colonies were cultured on agar plates with the TAP+N medium for one week to obtain sufficient populations for gene amplification. Through GFP gene amplification and electrophoresis, as shown in Figure 2.8e, the GFP gene was not found in the sample without green fluorescence. This means that this patterning platform can isolate only one cell from a sample mixed with various strains and provide a chance to retrieve colonies consisting of a single strain.

Even though the maximized single cell throughput of this platform is smaller than that of other platforms using external forces, on the scale of single cells, the throughput of this platform (32.8%) was similar to those of other platforms following Poisson statistics: Droplet microfluidics (<36%) (*74*), microwells (32%) (*75*), and oil-covered cell array (32%) (*76*). The density of the patterning area is limited due to the positive pillar array, however, the device can be easily and cheaply fabricated with more patterning areas in a larger PS substrate using one

step of solvent molding or injection molding. We expect to obtain thousands of single cell samples in a device whose price is just one dollar.

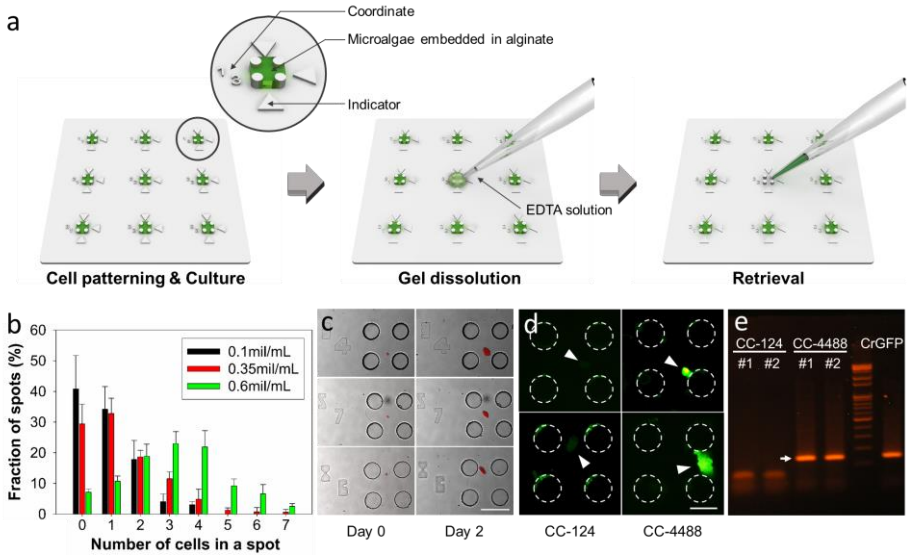

Figure 2.8. Single-cell patterning and retrieval platform. (a) The schematic process of retrieval of a single colony. The platform contains x- and y-coordinates and position indicators to provide precise positions of samples. C. reinhardtii samples embedded in alginate gel were cultured for two days, and the samples of interest were retrieved by gel dissolution using an EDTA solution by simple pipetting. (b) Distribution of captured cells in a single patterning spot according to various cell concentrations. (c) Microscopic images of single microalgae samples captured in single patterning areas (red: autofluorescence of a chloroplast, scale bar: 200 μm). (d) Fluorescence images of the wild-type (CC-124) and mutant strains (CC-4488) after two days of cultivation (scale bar: 100 μm). (e) Verification of the absence of cross-contamination during the retrieval process through gene amplification and electrophoresis. The arrow indicates a GFP gene with a length of 148 bp.

2.3.5. Sequential patterning for co-culture in 3D microenvironment

In our body, cells lie in cellular microenvironment composed of multiple cell types, extracellular matrix (ECM), and soluble factors. To understand the interactions between the composition, there have been a number of trials to control the cellular microenvironment (*77-79*). Spatially defined co-culture platforms using soft lithograph (*80-82*), negative dielectrophoresis (n-DEP) (*83*), and selective cell adhesion to ECM (*84*) were introduced, however, they remained in 2D culture or monolayer culture on ECM. Recently, as the importance of 3D microenvironment is emphasized in *in vitro* cell culture (*85*), 3D co-culture platforms were also developed such as microfluidic chip enabling hydrogel confinement (*86*) and hydrogel directed assembly (*87*). The microfluidic chip for 3D co-culture successfully patterns hydrogels with different type of cells, respectively, but further studies by retrieving the cells are challenging. The hydrogel assembly is soaked in medium so that it is difficult to observe a target assembly and two times of UV exposure for aggregation lower the cell viability. In this chapter, we are introducing a 3D co-culture platform on open surface.

Owing to the open surface, a shell-shaped liquid is patternable,

which was impossible in our previous research, microstructure mediated liquid patterning in microchannels (*88*). Figure 2.9 shows schematic process of sequential patterning using a shell-shaped liquid pattern. Pillars are arrayed to form two doughnut-shaped patterns when the liquid is swept over structures. By patterning the doughnut-shaped areas with a hydrogel, the inner area becomes another patterning area guided by walls of hydrogel. We demonstrated the reconstitution of an *in vitro* vascular network on a designed surface. Fibrinogen solutions with HUVECs was swept first to divide the inner areas into two loading zones. The core was filled with acellular fibrin matrix so that the vasculature, developed from the ECs in the inner doughnut-shaped area, can sprout into the core. The other space guided by the two fibrin walls was filled with fibrin matrix containing LFs. After five days of cultivation, the HUVECs grew, forming vascular networks with the designed shape.

This 3D microenvironment with high aspect ratio provides enough space for ECs to grow into tubular vessel network. This spatial patterning of ECs and stromal cells enables self-formation of 3D vessel network, which is difficult to accomplish in 2D platforms. Furthermore, the vessel network was formed on an open surface in contrast to on-chip vasculogenesis.[55] Thus, it is expected to enhance accessibility to samples

for further biomolecular analyses, such as western blotting. We also expect this multi-layer patterning tool can also be used for a cancer angiogenesis platform if adding cancer cells in fibrin matrix loaded in the core.

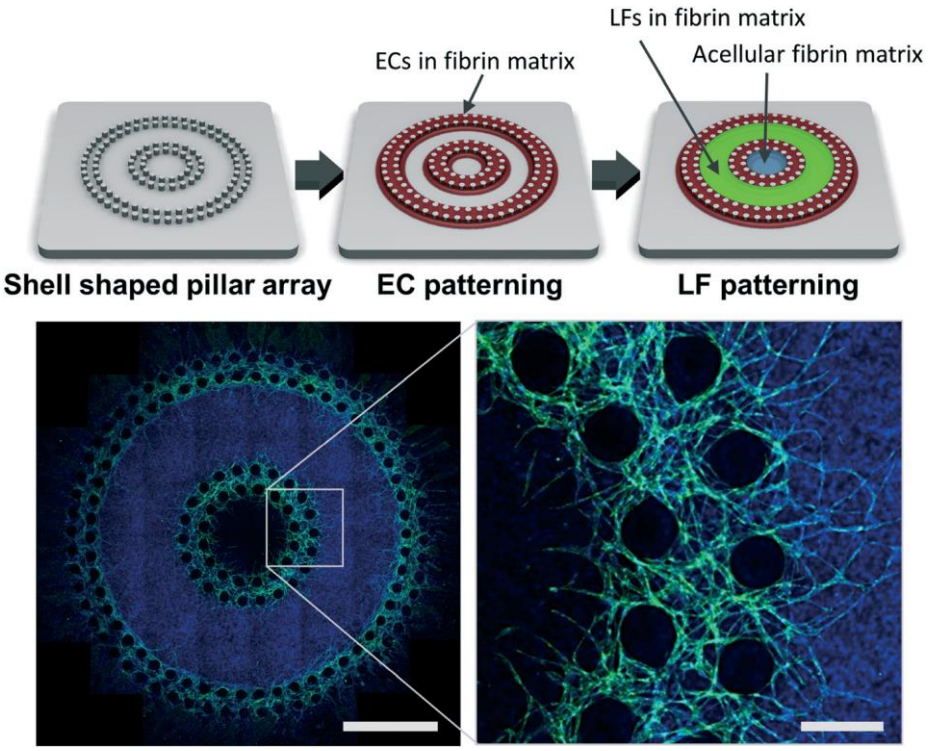

Figure 2.9. In vitro model of vasculogenesis. Endothelial cells (ECs) and lung fibroblasts (LFs) mixed with fibrinogen solution were patterned sequentially. A fibrin matrix containing ECs was initially trapped in two doughnut-shaped regions through a single sweeping motion and a fibrin matrix containing LFs was loaded into the area between the formerly patterned hydrogels. Acellular fibrinogen solution was loaded into the core region. The ECs formed vessel networks after five days of culture. Scale bar: 2 mm (left), 300 μm (right).

2.4. Conclusions

In summary, we have developed a novel liquid-patterning technique using a simple sweeping motion over a microstructured PS substrate. When the microstructures are strategically positioned on a flat substrate, a swept bulk drop over the surface leaves small droplets inside the areas cornered by the microstructures. Due to the niches between the structures, liquid can infiltrate into the structures with high aspect ratios without surface modifications. We demonstrated a single-cell screening platform and a 3D co-culture platform with capabilities of controlling the shape and volume of patterned liquids. This multi-scale liquid-patterning technique can be used for cell-based high-throughput screening and for other biological experiments.

Chapter 3. Aspiration-mediated microliquid patterning using rail-based open microfluidics

3.1. Introduction

Proper understanding of interactions between various cell types is essential in tissue engineering and design of in vitro organ models (*77, 89*). Microfluidic co-culture platforms embedding multiple cell types suspended in hydrogels can recapitulate specific organ functions and thus provide insights into complex physiological systems (*90, 91*). Microstructures within these platforms facilitate the arrangement of cells into physiologically relevant layouts (*92*). For example, porous membranes may provide permeable scaffolding to reconstitute cellular interfaces, such as the alveolar-capillary interface and the gut microenvironment (*8, 11*). Micropillars or bumps can mediate meniscus-pinning for precisely segregating co-cultures in hydrogels to model vasculature (*93*), blood-brain-barrier (*94, 95*), tumor extravasation dynamics (*96*), and glomerular filtration barrier (*20*). Ease of studying responses to mechanical and chemical stimuli using various laboratory imaging instruments complement the broad application space of these

culture systems.

Selective patterning of cell-loaded hydrogels commonly guides the gel into the desired area either by confining with surrounding pillar structures (*8, 11, 20, 93-96*) or by spontaneous capillary wicking in wettable channels (*26, 97-102*). The hydrogel loading guided by surrounding microstructures and wettability patterns fails when the hydrogel pressure exceeds a limit, or capillary-bursting pressure, causing the gel to invade the undesired region (*9, 23*). Thus, a great care should be taken to limit the injection pressure, resulting in yield variation depending on the operator's pipetting skill and low throughput associated with short available time of hydrogel precursor (*21*). Furthermore, the complex microscale features of such devices, achieved typically through soft lithography, preclude application of scalable manufacturing processes like injection molding (*21, 22*). Open microfluidic devices that utilize spontaneous capillary flow along rail structures present an alternative avenue for gel patterning without relying on the capillary-burst valve (*26, 97-102*). Here, rails denote long hydrophilic plates between which liquids are confined owing to capillary forces, while the side areas are exposed to surrounding fluids (*101*). In general, the air-liquid interfaces in rail-based microfluidics are highly

sensitive to the volume of liquid dispensed, thus making it difficult to accurately locate boundaries of patterned cell-laden hydrogels (*102*).

We here introduce a novel hydrogel micropatterning technology, which yields agile, easy and accurate formation of hydrogel patterns with only a simple pipetting activity, aspiration. The scheme relies on the capillary holding capacity of rail-based microstructures against aspiration upon their geometry, which can be tailored to leave hydrogel precisely in desired location. Although delineated below in detail, the working principle is based on the dynamic characteristics of a solid-liquid-gas contact line that it starts to recede when the local contact angle gets smaller than the critical receding angle. By defining where the recession starts and stop with geometric parameters like aspiration port diameter and rail height, we can selectively remove hydrogel from undesired regions. Experiments using simplified structures confirm theoretical design rules. Proper design provides control over the sequence of microchannel formation, which enables the formation of multiple discrete channels with a single aspiration. A proof-of-concept device featuring four microchannels separated by hydrogel structures is shown to be able to co-culture five distinct cell types. Our rail-based open microfluidic devices are amenable to fabrication by injection

molding, thereby suggesting their great potential as an easy-to-use co-culture platform with low cost and high manufacturing scalability.

3.2. Materials and Methods

3.2.1. Fabrication of open microfluidic devices

Digital light projector (DLP) 3D Printing (perfactory mini 4, EnvisionTEC) produced the bodies of open microfluidic devices with a photo curable resin (PIC100, EnvisionTEC). Rinsing with isopropyl alcohol in an ultrasonic cleaner for 15 min followed by curing ultraviolet curing (1500 W, 2 min) thoroughly solidified the printed pieces. Vapor deposition of parylene (LAVIDA, Femto science) onto the 3D printed parts ensured device biocompatibility. Attaching the bottom side of the printed part to a pressure sensitive adhesive (PSA) film completed the open microfluidic devices. Air plasma treatment of the device (70 W, 3 min) prior to fluid injection imparted hydrophilicity to the device surface for facilitating patterning of fluids under rail structures.

3.2.2. Cell culture

Cell culture experiments utilized human umbilical vein endothelial

cells (HUVEC, Lonza) cultured to passages between 4 and 7 in endothelial growth medium (EGM-2, Lonza), and normal human lung fibroblasts (LF, Lonza) cultured up to passage 7 in fibroblast growth medium (FGM-2, Lonza). CCD-18Co, HepG2, U87MG and H1299 cells were cultured in RPMI 1640 (Thermo Fisher) supplemented with 10% of FBS, penicillin (100U/ml) and streptomycin (100U/ml). 0.25% trypsin–EDTA (HyClone) facilitated detachment of cultured cells from the culture dishes. Re-suspension with appropriate amounts of culture medium provided target cell densities before mixing the cell suspension with bovine fibrinogen solutions in ratios of 3:1.

3.2.3. Hydrogel micropatterning

3D printed rail structures consisted of HRs surrounded by LRs. HRs housed holes that served as ports for injection of fluids and air infiltration. Injection of fluid via a micropipette through a port in the HR and immediate aspiration generated micropatterned fluid under LRs. Subsequent cross-linking of the solution resulted in patterned hydrogels and adjacent microchannels. Visualization of the patterns employed a solution of bovine fibrinogen (5 mg/ml, Sigma) dissolved in water and mixed with green food dye. Mixing with 25 U/ml of thrombin (Sigma)

solution in a 30:1 ratio (v/v) at room temperature began the polymerization reaction of fibrinogen to fibrin. Exposing the loaded device to ambient conditions for 5 min resulted in fully crosslinked green dyed fibrin gel.

For microfluidic co-cultures, fibrinogen solution (10 mg/ml) mixed with cell suspension in ratios of 1:3 (v/v) yielded cellular gels with a final fibrinogen concentration of 2.5 mg/ml. Mixing with thrombin solution (25 U/ml) in a 50:1 ratio immediately before injection into the fluid ports began the polymerization reaction. Immediate patterning and incubation in a cell incubator (37°C, 5% of CO_2, 3 min) resulted in fully crosslinked fibrin gel encapsulating cells. Culture of the cellular gels involved adding EGM-2 into each well of the device, followed by incubation for five days with media changes every two days.

3.2.4. Image analysis

A digital microscope (AM4115TW, Dino-Lite) captured time-lapse images of microchannel formation and images of various microchannel designs. Image analysis using ImageJ of 3D printed bodies provided measured diameters of fluid ports. Labeling of HUVECs with a mouse monoclonal antibody specific for human CD31 (AlexaFluor®488

conjugated, BioLegend) following supplier's instruction allowed comparison of vasculogenic capacities of various cell types. Confocal microscopy (A1, Nikon) imaged labeled samples through optical z-sectioning (100 and 5 μm in depth and interval, respectively). Image analysis for vascularized area measurement utilized Z-projection and conversion to binary images using auto threshold in Fiji following the "Li" method.

3.3. Results

3.3.1. Microstructures for aspiration-mediated patterning

Our rail-based open microfluidic platform consists of a 3D printed structure of photo curable resin having rails of different heights to retain liquid with different strengths and surrounding walls, which is bonded to an underlying pressure sensitive adhesive (PSA) film (Figure 3.1a). The length of the rail, l, is 5 mm, and the width of low and high rail, w_l and w_h, is uniformly 1 mm. The heights of low and high rails are respectively h=100 mm and H=300 mm. Two through-holes at the ends of a high rail function as fluid ports for liquid injection and aspiration. Air plasma treatment activates the surface of the device by increasing hydrophilicity.

Figure 3.1b illustrates the basic working principle of the novel patterning process of hydrogel, which allows us to form hollow microchannels surrounded by precisely defined hydrogel patterns. We first inject a hydrogel precursor solution through one of the fluid ports, which fills the area under all rails and runs along the corner of the wells (the second column of Figure 3.1b). Upon aspiring through the open port, the liquid is sucked into the pipette only from the region below high rail, while the low rail strongly retains the liquid (the third column of Figure 3.1b). The result is the hollow microchannel defined by the empty region under the high rail with the hydrogel remained pinned by the low rail (the fourth column of Figure 3.1c). In the following, we delineate the physical principle behind this selective removal and controlled pinning of hydrogel patterns, which leads to various hygrogel-based channel structures and facile fabrication of cell co-culture systems.

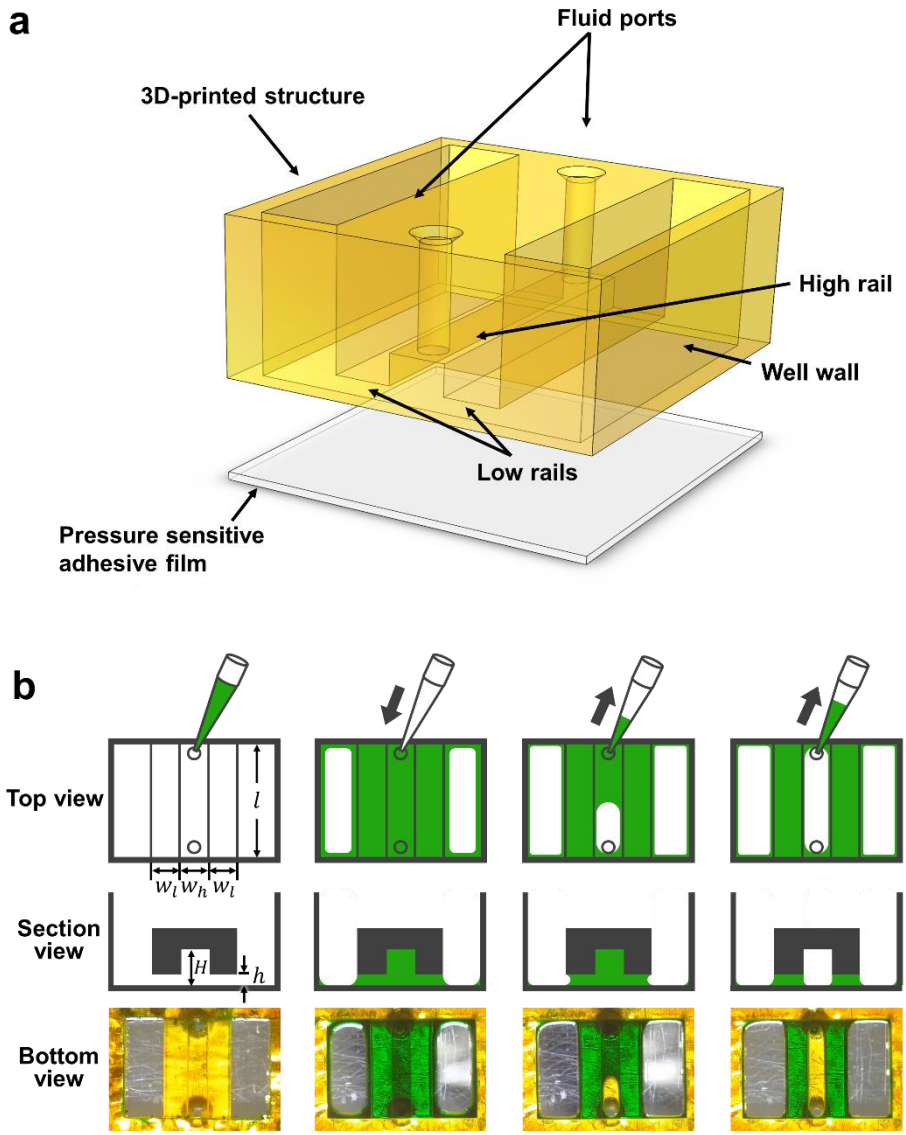

Figure 3.1. (a) Schematic exploded view of a rail-based open microfluidic device, which is designed to yield a single channel beneath the high rail. (b) Illustration of steps in the aspiration-mediated microchannel formation process. The bottom row features optical images taken through the clear PSA film from the underside of the device during filling and aspirating green dyed water.

3.3.2. Theoretical analysis of microchannel formation

As the pressure at an open port is lowered by aspiration with a micropipette, the interior pressure of the hydrogel is also lowered. The Young-Laplace equation states that the liquid-gas interface of the hydrogel originally filling the gaps caves inward, Figure 3.2, due to the pressure difference between the atmosphere (p_a) and the liquid (p_l): $\Delta p = p_a - p_l = \gamma\kappa$, where γ is the gas-liquid interfacial tension and κ is the interface curvature. The contact line where the gas-liquid interface meets the solid surface is initially immobile while resisting the pulling force because it can recede only when the contact angle is reduced below the critical receding contact angle, $\theta_{R,c}$ (*103*). We experimentally found that $\theta_{R,c}$ is nearly zero for hydrogel on the hydrophilized 3D printed part of resin and PSA film surfaces. The patterning of hydrogel that originally fills the gaps under both high rails (HRs) and low rails (LRs) critically depends on where the interface starts to recede first by reaching $\theta_{R,c}$.

For the initially hydrogel-loaded configuration, the liquid-gas interfaces arise at the open port and the side areas of liquid beneath LRs. For the open port of diameter D, the maximum pressure difference that the interface can withstand before the contact angle on the inner wall of

HRs reaches zero, Δp_o, corresponds to the pressure difference for a hemispherical interface with the maximum curvature of $4/D$: $\Delta p_o = 4\gamma/D$. The capillary pressure at the interface beneath LRs is given by $\Delta p = \gamma(2\cos\theta/h + 1/\eta)$, where θ is the instantaneous contact angle of liquid, and η is the radius of curvature on a plane parallel to the substrate. As η is scaled as l, the length of rails, we get $h \ll l$, which allows us to estimate the maximum pressure difference for the side area below LRs as $\Delta p_{\mathrm{L}} = 2\gamma/h$.

If $\Delta p_o < \Delta p_{\mathrm{L}}$, the critical liquid pressure for interface recession is reached at the open port before the side area. Once burst at the open port, the interface spontaneously bulges accompanying the decrease of interface curvature to meet the bottom substrate. Then the interface curvature is newly defined by the height (H) and width (w_H) of HR. The critical capillary pressure that can induce interface recession beneath HRs is given by $\Delta p_{\mathrm{H}} = 2\gamma(1/w_{\mathrm{H}} + 1/H)$. If $\Delta p_o > \Delta p_{\mathrm{H}}$, the liquid pressure is already low enough to ensure continuous recession of the liquid beneath HR. If $\Delta p_o < \Delta p_{\mathrm{H}} < \Delta p_{\mathrm{L}}$, further decrease of the liquid pressure upon bursting of the open port can cause the liquid to recede along a lane beneath HR. The liquid will stop upon bursting at the open port and recede beneath LRs, rather than HRs, if $\Delta p_{\mathrm{H}} > \Delta p_{\mathrm{L}}$.

Figure 3.3 displays the experimental results of hydrogel patterning for different geometries of microdevices. In the left column, Δp_{L} is greater than both Δp_o and Δp_{H}, and thus the interface recession occurs from the open port, continues beneath HR, to result in a straight empty lane flanked by the hydrogel beneath LR. In the middle column, the side areas beneath LRs burst before the open port because $\Delta p_{\mathrm{L}} < \Delta p_o$. In the right column, the open port bursts first because $\Delta p_{\mathrm{L}} > \Delta p_o$, but further decrease of the liquid pressure bursts the side areas beneath LRs before the interface from the open port starts to recede beneath HR.

Figure 3.4 displays the experimental results of microchannel formation as a function of the geometry of device, such as the port diameter and the heights of low and high rails. In Figure 3.4a, we can predict where the interface recession onsets upon aspiration, whose criterion is given by $\Delta P_L = \Delta P_o$, or $D = 2h$. For $D > 2h$, we get $\Delta P_L > \Delta P_o$, and thus the port bursts first, leading to successful channel formation in the beginning. Otherwise, the interface moves at the side area of LR before at the port, preventing the formation of the microchannel under HR. Figure 3.4b gives the condition of the height of HR to ensure that the interface formed from the open port keeps receding while the interface beneath LR remains pinned. The corresponding boundary is

given by $\Delta P_L = \Delta P_H$, or $H = h/(1-h)$. For $H > h/(1-h)$, we get $\Delta P_L > \Delta P_H$, leading to continuous recession of the interface from the open port. Otherwise, the interface under LR starts to recede, eventually merging with the interface originated from the open port. We see that our experimental results agree well with the theoretical predictions in Figure 3.4.

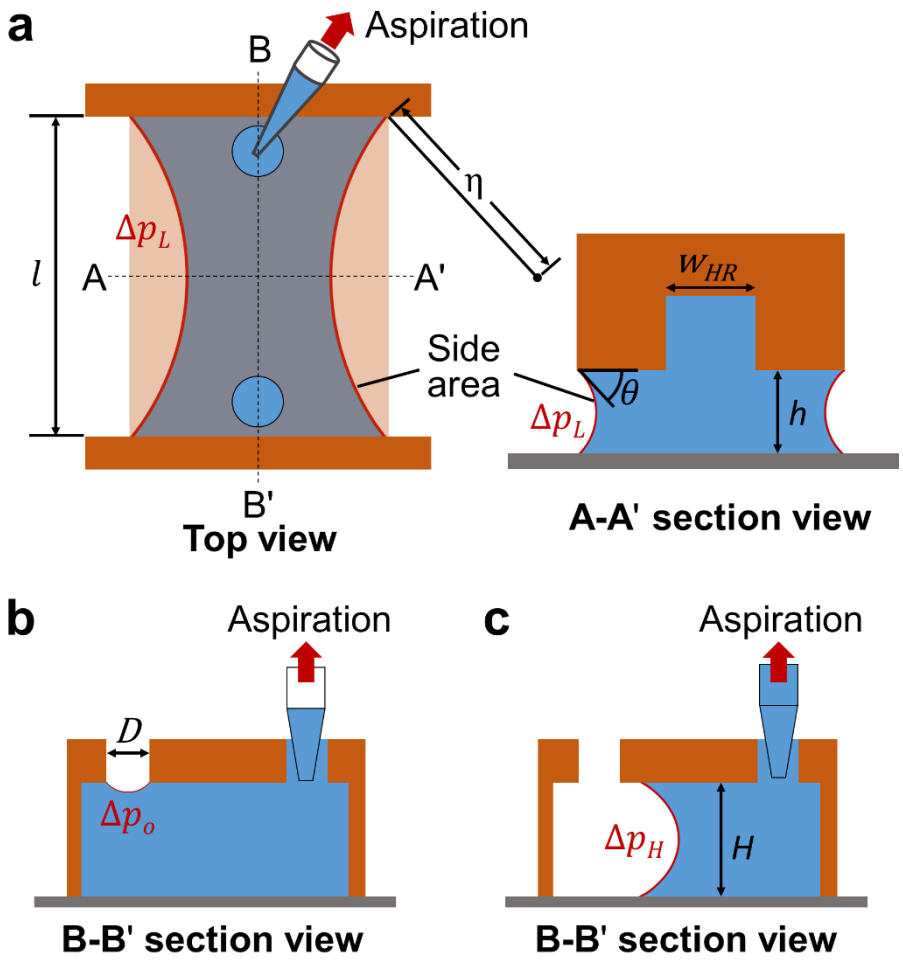

Figure 3.2. Schematic diagrams indicating key device dimensions and the Laplace pressures of menisci (a) immediately after aspiration, (b) as the port interface deforms, and (c) as the receding interface travels along HR.

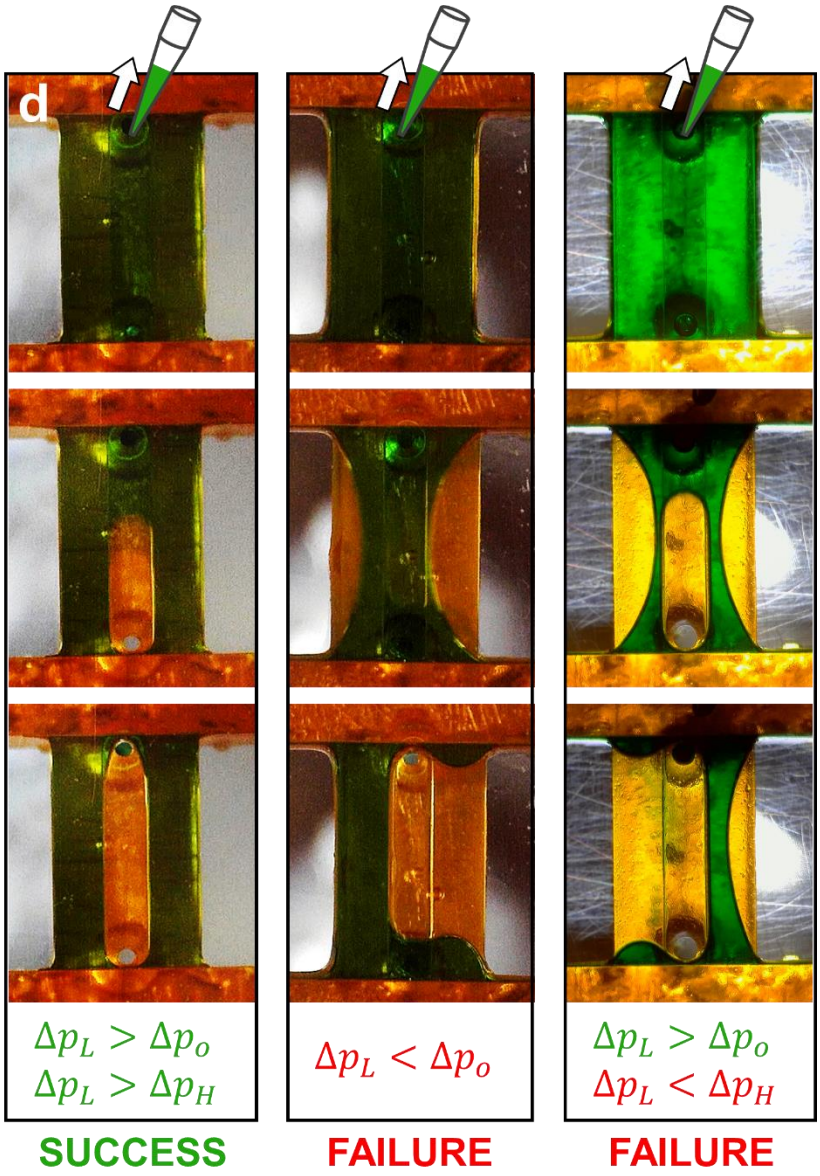

Figure 3.3. Meniscus dynamics during aspiration under three different combinations of critical capillary pressures. The dimensions of the structures are such that [*H*, *h*, *D*]=[300, 100, 300] μm, (Left column), [300, 200, 300] μm (middle column), [200, 175, 500] μm (Right column). Lengths and widths of all rails are fixed as 5 and 1 mm, respectively.

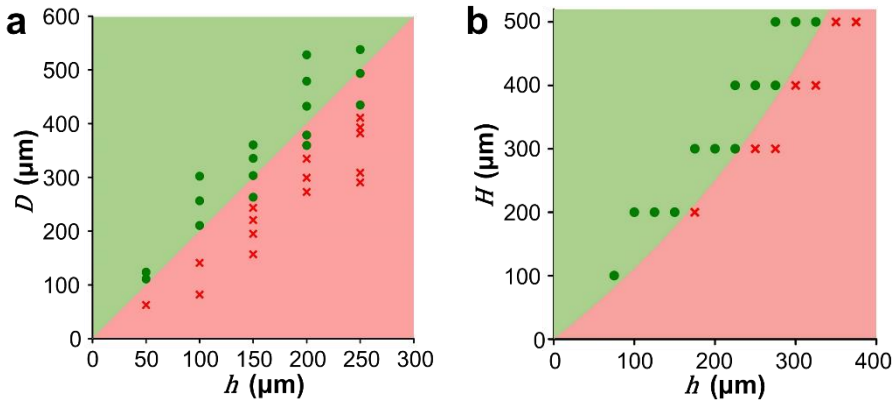

Figure 3.4. (a) Plots of the effects of port diameter and LR height on bursting at the open port. (b) Plots of the effects of HR height and LR height on formation of microchannel. Shaded regions demarcate dimensions suitable (green) and unsuitable (red) for microchannel formation based on the theoretical calculations. Markers indicate successful (green) and unsuccessful (red) microchannel formation in experiments. Lengths and widths of all rails are fixed as 5 and 1 mm, respectively.

3.3.3. Formation of multiple discrete microchannels

Studies of fluid dynamics under the basic rail structure verify that the air-liquid interface with the smallest critical capillary pressure tends to move first along the rail. Leveraging this phenomenon can provide control over the sequential formation of discrete microchannels with a single aspiration. Figure 3.5 and 3.6 exemplify multiple channel formation using various critical capillary pressures at air-liquid interface pinned at holes. In this device, a rectangular LR, 75 μm from the underlying PSA film surrounds 'S', 'N', and 'U' shaped HRs, 300 μm apart from PSA. The diameter of fluid ports decreases in the order of S1 to U1 as listed in the table in Figure 3.5 while U2 has the largest port diameter. When aspirating dyed water filling under the rail structure from the port labeled 'U2', the air-liquid interface at the largest opposing port (S1) begins traveling along the rail to form an 'S' shaped microchannel (the second panel of Figure 3.3b). As the suction continues at U2, the air-liquid interface at the next largest port (N1) now begins to recede (the third panel of Figure 3.3b). Consequently, microchannels with shapes of 'S', 'N', and 'U' form via a single aspiration process through one port as shown in Figure 3.5.

During multiple channel formation, differences in port diameter

within the same channel lead to orderly movement of the air-liquid interface. If ports of the same diameters are employed, air can infiltrate into the channel through the identical ports simultaneously, to form a thin film of liquid between the infiltrating air from the two ports, as shown in Figure 3.7. Breaking the thin film to form a continuous microchannel requires additional pressure drop since foam films have larger Laplace pressures than droplets of equal curvature, owing to the presence of two air-liquid interfaces (*103*). In the video, a continuous microchannel forms in the top right HR because it contains the port of aspiration, and thus only a single port for air infiltration. In contrast, a similar device employing asymmetrical port sizes in each HR exhibits unidirectional movement of air-liquid interfaces beneath HRs as shown in Figure 3.8.

This unique liquid patterning technique enables versatile rendering of microchannel in hydrogels. Figure 3.9a and b show devices with multiple hydrogel channels arranged in parallel lines and a lattice of squares, respectively. Figure 3.9c and d respectively highlight the ability of our scheme to generate a single circular and two concentric channels. We note that the circular designs can facilitate investigation of radial interaction between patterned cells as described earlier (*104*).

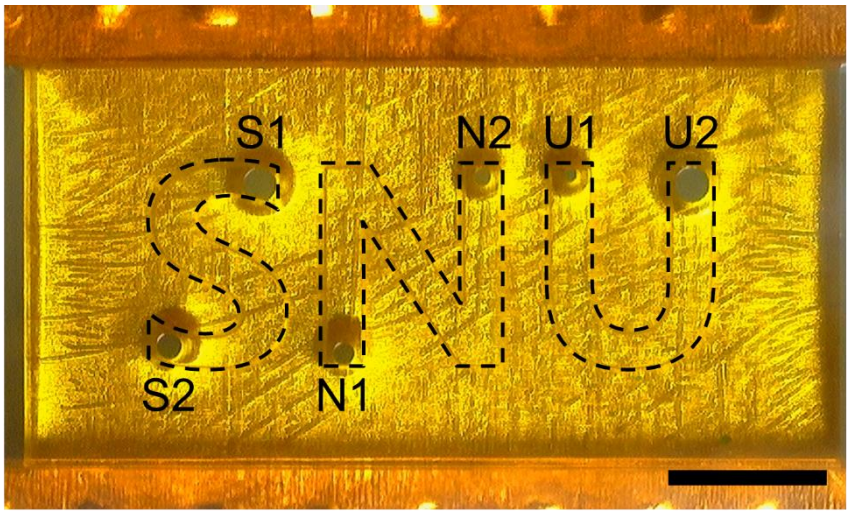

Port	Diameter (μm)	Port	Diameter (μm)
S1	400	S2	300
N1	250	N2	190
U1	140	U2	420

Figure 3.5. An open microfluidic model for rendering multiple discrete microchannels using different port sizes. An image of the underside of a device with three HRs in the shapes of 'S', 'N', and 'U', surrounded by a rectangular LR (scale bar: 2 mm). Loading and aspiration occur through port U2. Opposing port sizes decrease from S1 to U1 as indicated in the bottom table.

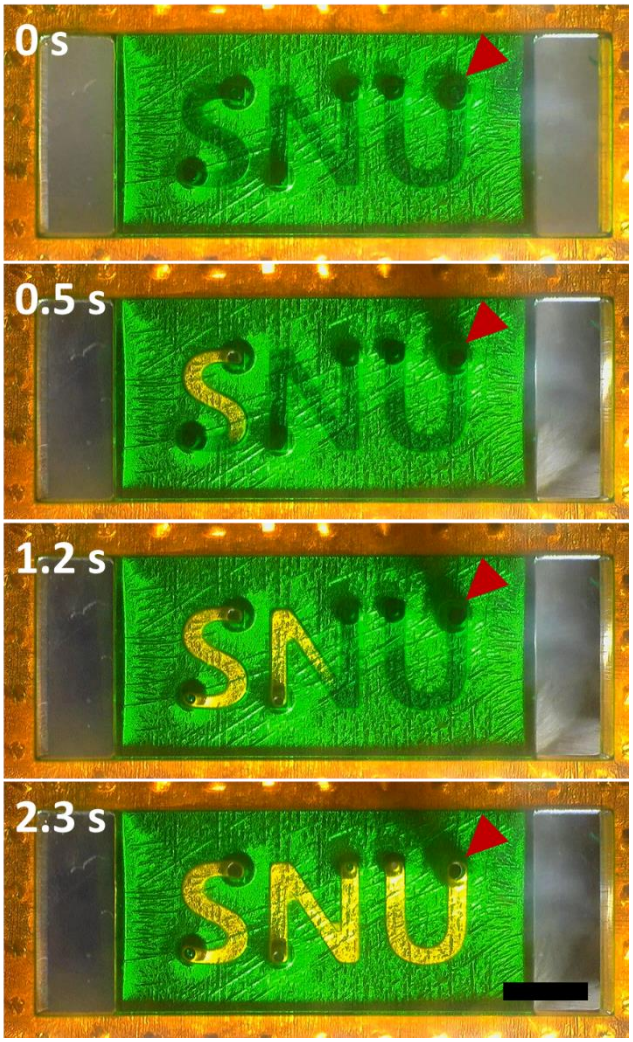

Figure 3.6. Sequential snapshots (top to bottom) viewed from the bottom of the device during aspiration. Air-liquid interfaces preferentially advance from the largest port to the smallest port. Red arrows indicate the aspirating port, U2. (Scale bar: 2 mm)

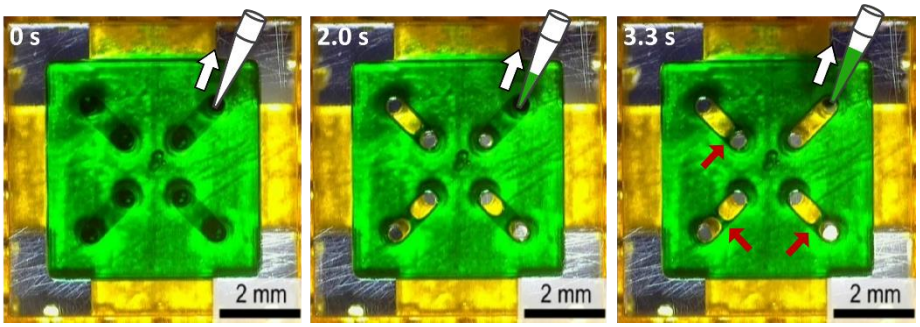

Figure 3.7. Sequential snapshots viewed from the bottom of a square-shaped device during aspiration. Air-liquid interfaces at both holes connected with a single channel burst into the area under HRs due to the identical hole size, resulting in thin film formation of liquid. Arrows indicate the thin film of liquid.

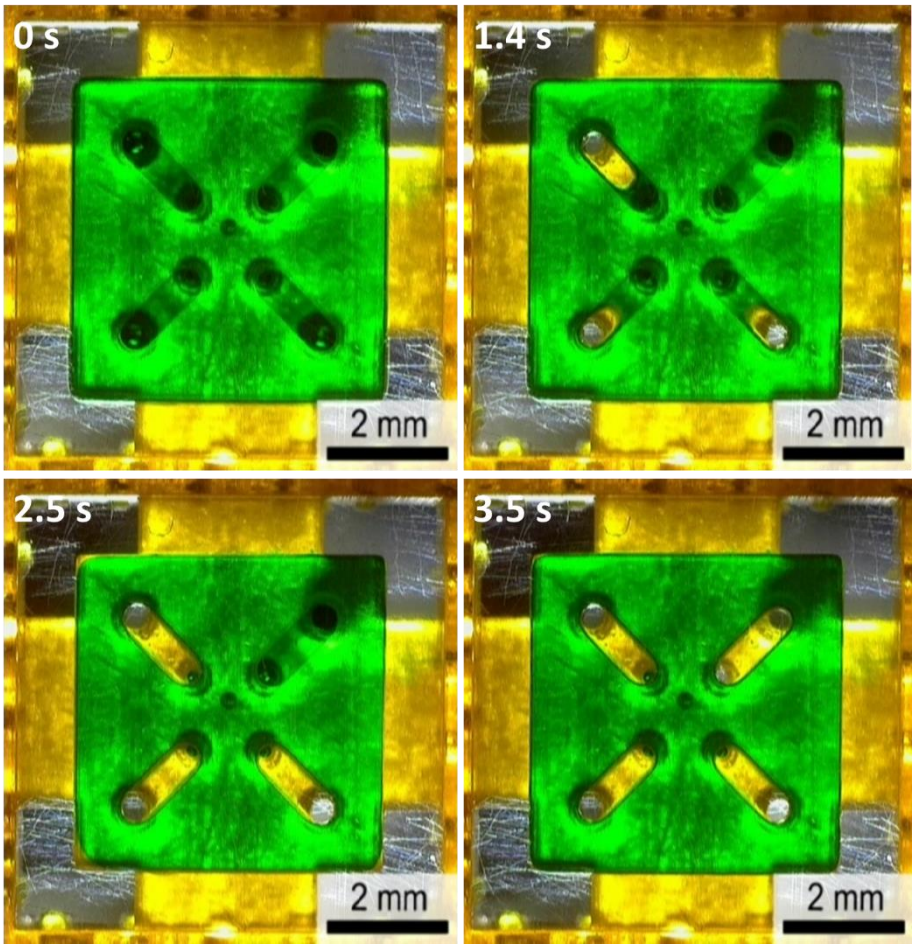

Figure 3.8. Sequential snapshots viewed from the bottom of a square-shaped device during aspiration. Air-liquid interfaces pinned at larger holes burst into the area under HRs, resulting in unidirectional movement of interfaces, resulting in formation of four channels.

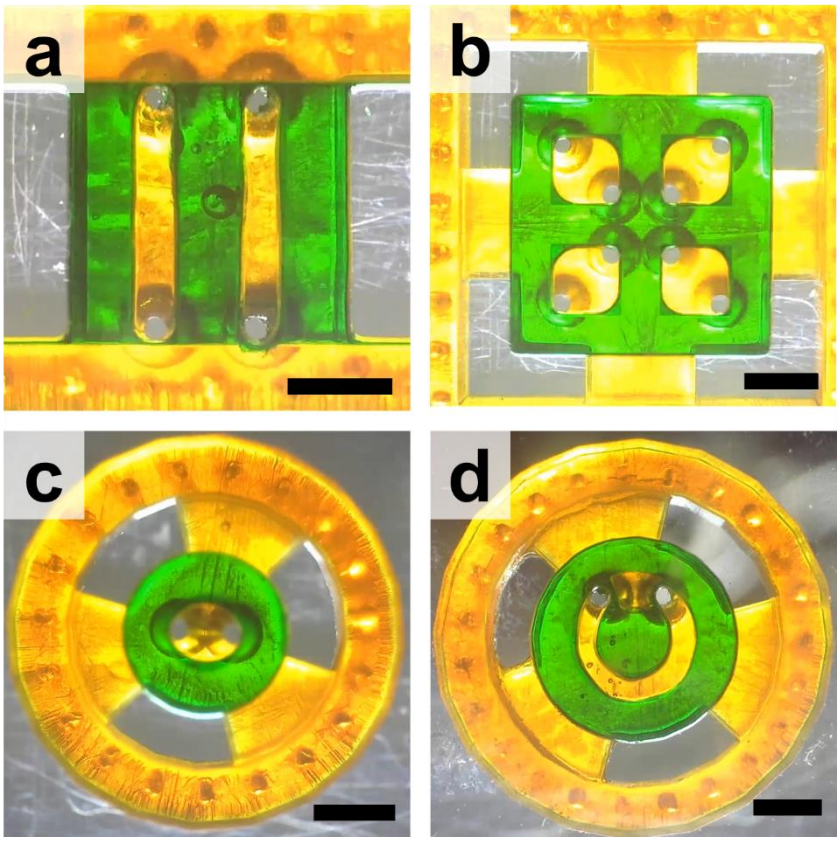

Figure 3.9. Bottom view images of devices with multiple green hydrogel channels organized into (a) parallel lines, (b) a square lattice, (c) a circle, and (d) concentric circles. Scale bar, 2 mm.

3.3.4. An application for screening vasculogenic capacities

Modification of the device in Figure 3.9b provides a platform for convenient and effective comparison of paracrine signaling induced by co-culture of five cell types. Here, the microfluidic device contains four linear HRs surrounded by a square LR (Figure 3.10a and b). Four support structures suspend the rail structures by connecting them to the well walls, which form growth medium reservoirs when bonded to a PSA film. Patterning of a fibrin hydrogel (2.5 mg/ml) containing a mixture of human umbilical vein endothelial cells (HUVEC, 4 x 10^6 cells/ml) and lung fibroblasts (LFs, 1 x 10^6 cells/ml) under the LR, and subsequent seeding of gels containing different cell types into the rendered microchannels establishes the basic experimental setup. The present studies involve eleven devices with channels containing different combinations of LFs, colon fibroblast cell line (CCD-18Co), liver cancer cell line (HepG2), glioblastoma cell line (U87MG), and lung carcinoma cell line (H1299). All gels contain cell concentrations of 5 x 10^6 cells/ml except for an acellular fibrin gel as a control. Figure 3.11a presents a confocal image of an exemplary device taken after 5 days of cultivation. Regions of interest (ROI) measuring 1 x 1.8 mm^2 in area, which is located around each HR, encompass the interfaces between the HUVEC-

LF gel and the gels containing cells of interest. Analysis of z-projected confocal images yield quantification of the vasculogenic capacities of the cells of interest (Figure 3.11 and 3.12). In alignment with previous studies (*93, 100, 105*), LFs vigorously promote formation of vasculature. Furthermore, acellular gels and gels containing LFs exhibit angiogenic sprouting into the channels. On the other hand, U87MG and H1299 gels inhibit the growth of surrounding vessels and do not provoke cancer angiogenesis. Gels containing CCD-18Co and HepG2 show no significant difference in vasculogenic capacity compared against the acellular matrix. The results of these tests corroborate the ability of the platform for screening candidates for cancer angiogenesis in vitro. Furthermore, the versatility of the channel rendering method supports facile device adaptation to study a broad range of paracrine signaling cues in various conformations.

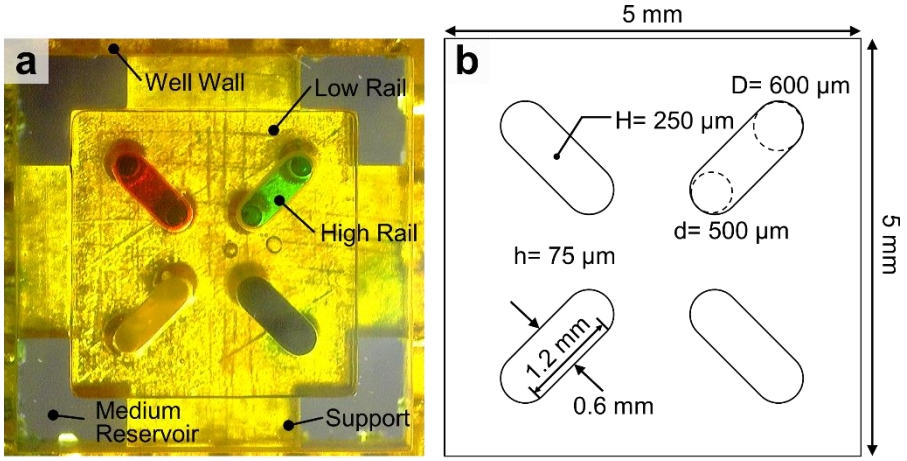

Figure 3.10. An open microfluidic design of multiple channel rendering for screening vasculogenic capacities of multiple cell types. (a) Bottom view image of microfluidic device with four channels and a square shaped LR. (b) Illustration of device dimensions.

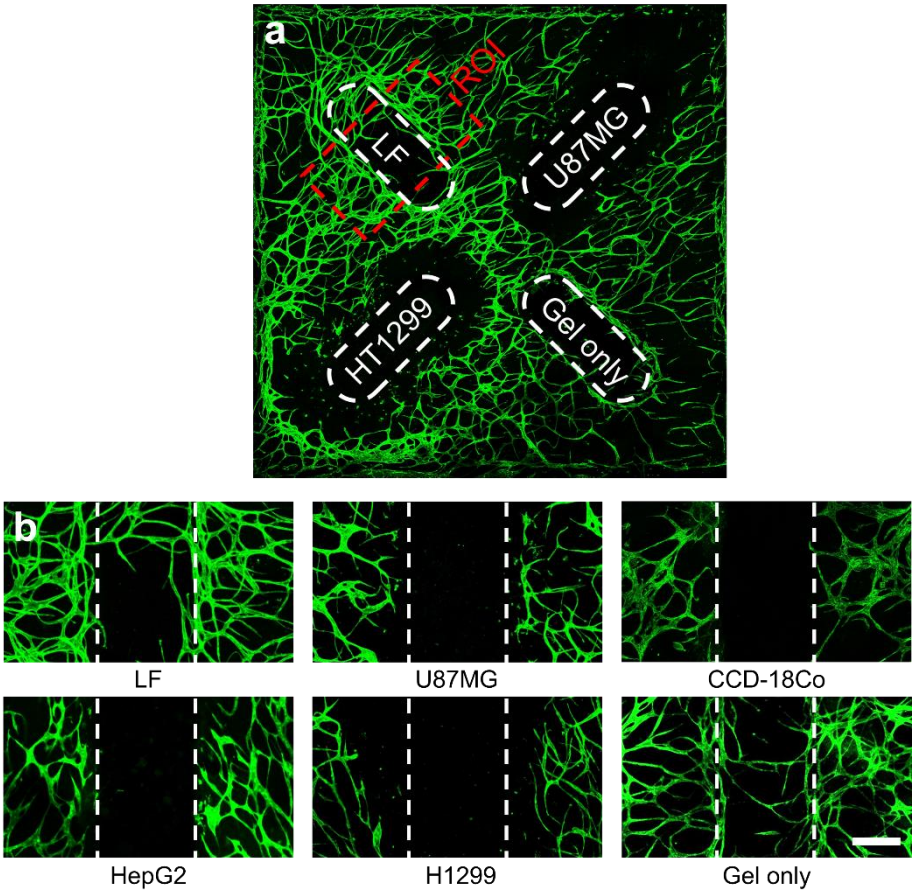

Figure 3.11. Confocal fluorescence images of the vasculogenic co-culture model showing CD31 labeled HUVECs with green fluorescence. (a) A confocal image displaying vessel network under the whole culturing area under rail structure. Red dashed box delineates an example region of interest (ROI). (b) Representative confocal micrographs of ROIs in channels containing different cell types. Scale bar, 300 μm.

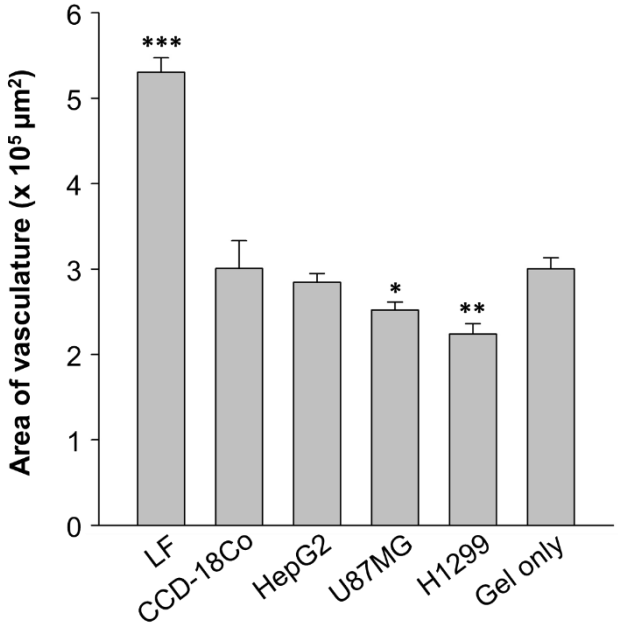

Figure 3.12. Plot of vascularized area within the ROIs for each cell line. Statistical significances (*$p < 0.05$, **$p < 0.01$, and ***$p < 0.001$) result from unpaired two-tailed Student's t-tests for comparison with the 'Gel only' condition.

3.4. Conclusions

The reported hydrogel patterning method based on interfacial capillary dynamics and associated device design strategies form the foundation of a new class of aspiration-mediated open microfluidic devices featuring versatile designs and simple operation. The rail structures in these devices, composed of different heights of rails with embedded fluid ports, embody varying critical capillary pressures at each air-liquid interface. Systematic studies corroborated by theoretical models reveal fundamental design rules based on the relationships between geometric parameters of these structures and the capillary pressures. Leveraging these insights serves the development of devices where aspiration selectively removes injected hydrogel precursor beneath high rails to leave behind precisely rendered microchannels. Furthermore, this concept extends to the generation of multiple discrete channels via aspiration from a single fluid port, enabling a wide range of patterning designs with simple fabrication. A demonstrated high-throughput co-culture model for assessing vasculogenic capacities of multiple cell types highlights the practical applications of the multiple channel formation method.

These rail-based microfluidic devices allow simple and robust

patterning based on aspiration, dramatically enhancing experimental throughput and mitigating users' error faced by conventional approaches. When using hydrogel as ECM, simplified patterning process increases the number of samples obtained from a single mixture of hydrogel precursor during cross-linking. The shortened patterning time can also enhance uniformity in properties of hydrogels between samples. Furthermore, the simple geometries of the rail structure are compatible with scalable manufacturing techniques such as injection molding. The enhanced experimental throughput and productivity offered by the outlined strategies can contribute to new high-throughput screening models and accelerate commercialization of microfluidic cell culture models.

Chapter 4. High-throughput microfluidic 3D cytotoxicity assay for cancer immunotherapy

4.1. Introduction

Adoptive transfer of *ex vivo* cultured/engineered cytotoxic lymphocytes (CLs) is arising as a promising approach to treat cancers (*106*). In particular, T cells expressing chimeric antigen receptor (or CAR-T cells) have been extremely successful in the treatment of CD19 expressing leukemia and lymphoma (*107-109*). The success has led to FDA approval of two CAR-T cell-based therapies, Kymriah (Novartis) and Yescarta (Gilead), and new CAR engineering strategies have been studied to improve the performance, reduce toxicity, and broaden applications of CAR-T therapy (*110, 111*). In addition, NK cells and γδ T cells, which exhibit low cytotoxicity and minimum graft-versus-host disease in allogeneic transfer compared with T cells, have been developed as alternatives of CAR-T cells as an off-the-shelf therapeutics. (*112, 113*) In spite of these efforts, the performance of adoptive transferred CLs against solid tumors is still limited due to complex tumor microenvironment (TME) that limit trafficking and effector functions of CLs (*114, 115*). In addition to highly immuno-suppressive

microenvironments caused by acidic and hypoxic conditions and enrichment of suppressive cells (*116-118*), fibrotic tumor stroma is an important factor limiting successes of cancer immunotherapy by acting as a physical barrier for CLs to access tumor cells (*119, 120*). Therefore, various factors comprising TME need to be considered for the development of engineered CLs for solid tumors.

Cytotoxicity assay measuring killing ability of CLs is one of the most critical assays for the development of CLs for cancer immunotherapy. Chromium or calcein release assay based on the measurement of released radioactive ^{51}Cr or fluorescence calcein from lysed cancer cells has been a standard method for assessing cell-mediated cytotoxicity (*121, 122*). These methods have been widely used because cytotoxicity can be assessed simply by co-culturing CLs with tumor cells loaded with ^{51}Cr or calcein. In addition, these assays are compatible with 96 well formats, thus can be performed in high-throughput fashions. However, in these assays, tumor cells are either adhered on flat surfaces or suspended in medium, thus complex TME in solid tumors limiting CL activity are lacking.

Microfluidic-based platforms, which allow the reconstitution of complex 3D microenvironments of human tissues in *in vitro* by

compartmentalization of multiple cell types, applying chemical and mechanical stimulations, and controlling chemical gradient (*123*), can be a powerful method for the assessment of lymphocyte cytotoxicity for solid tumors (*124*). Recently, microfluidic chips based on poly(dimethyl siloxane) (PDMS), a common material for microfluidics, were developed as preclinical models to evaluate antitumor activities of engineered T cells expressing T cell receptors specific for tumor antigens (or TCR-T cells) (*125, 126*) or engineered NK cells expressing Fc receptors (*127*) in 3D microenvironments recapitulating various aspects of TME. Specifically, microfluidic chips compartmentalized with 3D ECM gels containing tumor cells and TCR-T cell loading zones were used to assess the roles of hypoxia, inflammatory cytokines, immunosuppressive conditions induced by mTOR inhibitors, and monocytes on the cytotoxicity of TCR-T cells (*125, 126*), and microchips filled with ECM gels containing tumor cell spheroids and perfusable tubular vasculatures were used to recapitulate TME for NK cell trafficking toward solid tumors and to test combination of immuno-stimulatory biologics with NK cell therapy (*127*). However, the devices aforementioned requires labor and time intensive batch fabrication processes because the device was made of PDMS (*128*).

In this study, we introduce a 3D cytotoxicity assay using an injection molded plastic array culture (CACI-IMPACT) platform with which we can monitor both migration and cytotoxic activity of CLs in 3D microenvironment, by customizing our previous IMPACT device (*99*). We adopted extracellular matrix (ECM), which is a basic component of TME and did not exist in the standard protocols of cytotoxicity assays. ECM acted as physical barrier to restrict CLs from access cancer cells embedded in it. The limited accessibility resulted in low cytotoxicity compared with 2D assay. In addition, fibrotic ECM of TME was reconstituted by using denser collagen which lowered migration and cytotoxicity in observation of large area, but induced faster lysis process than sparser ECM. Furthermore, we improved the assay throughput compared with PDMS devices due to enhanced productivity oriented by changing material and usability mediated by rail-based microstructures. This model allowed us to test the effect of the physical properties of the 3D microenvironment on cytotoxic activity and we expect that this model can be used for high-throughput screening platform for estimating the efficacy of engineered lymphocytes in more *in vivo* like environment than conventional assays.

4.2. Materials and Methods

4.2.1. Cell culture

HeLa cells were cultured in Dulbecco's modified eagle's medium (DMEM) with 10% of fetal bovine serum (FBS) and 1% of penicillin–streptomycin (PS). NK-92 cells were cultured in minimum essential media alpha (MEM α) with 15% of FBS, 15% of horse serum (HS) and 1% of PS and other supplements, including myo-inositol (0.2 mM), 2-mercaptoethanol (0.1 mM), folic acid (0.02 mM). NK-92 cells were sub-cultured in every two days in 6 ml of the full medium and 1200 units of Interleukin-2. Sub-culture was conducted in T25 flasks with cell concentration of 10^5 cells/ml.

4.2.2. Fluorescent labeling of live and dead cells

HeLa cells were labelled with CellTrace™ CFSE Cell Proliferation Kit (Thermo fisher, C34570) by incubating the cells in serum free DMEM with 2 μM of CFSE for 30 minutes. NK-92 cells were labeled with CellTrace™ Far Red Cell Proliferation Kit (Thermo fisher, C34572) by incubating the cells in serum free MEM α with 2 μM of the reagent for 20 minutes. To detect dead cells, propidium iodide (PI) was used. For

live imaging, PI-containing medium was used from the beginning of imaging. For imaging after 24 h of NK-92/HeLa co-culture, the medium was replaced with PI-containing medium 30 min prior to imaging.

4.2.3. 3D cytotoxicity assay using gel patterned device

CFSE-labeled HeLa cells were mixed with collagen gel pre-solution, which is a mixture of rat tail oriented collagen type I (Corning, 354249) with concentration of 9 mg/ml and 150 mM HEPES buffer at 2:1 ratio (v/v). The collagen pre-solution containing HeLa cells were patterned under the low rails of a CACI-IMPACT device (Figure 4.3a) following air plasma treatment with 70W for 3 min. The device was incubated in a cell culture incubator with 37°C and 5% of CO_2 for 30 min to crosslink the collagen. The cross-linked collagen gel blocks were immersed in media and further incubated for 24 h in the cell culture incubator. NK-92 cell suspension (2×10^6 cells/ml, 2 μl) was loaded into the channel, and the device was stored in the incubator for 20 min at an angle of 90 degrees to let the NK-92 cells settle down on one side of the collagen block encapsulating HeLa cells. Then, the two medium reservoirs were filled with MEMα, and the devices were stored in the incubator for 24 h, or in a live imaging system. PI was added in the

medium, and fluorescence images were acquired to assess cytotoxicity.

4.2.4. Image analysis

Time-lapse images were acquired using an inverted microscope system (Nikon eclipse Ti-E). Endpoint images of NK-92/HeLa co-culture were acquired using a confocal microscope (Nikon Ti 2 A1) through optical z-sectioning (depth: 100 μm, interval: 4 μm). For image analysis, we used Fiji. Z-projected images were used for display and the images were converted into binary images using auto threshold ('Mean' method) in Fiji for quantitative analysis. The number of NK cells in each sub-region was estimated by dividing the total area of NK cells into the average single NK cell area. Similarly, the percentage of killed HeLa cells were estimated using HeLa cell areas. Since live HeLa cells exhibited extended morphology whereas dead HeLa cells were rounded, areas of dead HeLa cells were converted to those of equivalent number of live HeLa cells by multiplying an average ratio of single live and dead HeLa cell area. Finally, the percentage of killed HeLa cells were calculated by (converted dead HeLa cell area)/(live HeLa cell area + converted dead HeLa cell area). Five unbiased students manually selected 20 NK and HeLa cells respectively and the average areas of the

selected 100 NK and HeLa cells were used for single cell area of each cell type.

4.2.5. 2D cytotoxicity assay

CFSE-labeled HeLa cells were plated in each well of a 24 well-plate (6 x 10^4 cells/well) and cultured for 24 h. Then, various numbers of NK-92 cells were added to the well, and HeLa and NK-92 cells were co-cultured for another 24 h. PI was added to the media to have final concentration of 3 μM, and the percentage of dead HeLa cells were measured by fluorescence microscopy.

4.3. Results

4.3.1. Design and fabrication of devices

To fabricate microfluidic devices for cytotoxicity assays in 3D ECM gels, we first designed and fabricated injection molded microfluidic devices that enable facile hydrogel patterning (Figure 4.1). To efficiently observe cytotoxic activity of CLs through fluorescence microscopes equipped in typical biology labs, the device was designed to have the same dimension as a standard microscope slide (3″ x 1″), and

rail-based microstructures under which cytotoxicity assays would be conducted were embedded in 2 x 6 rectangular array of wells with the same pitches as the conventional 96 well-plate (Figure 4.1a). The rail-based microstructures for hydrogel patterning is composed of two primary patterning rails (low rail, or LR), which are 100 μm apart from the bottom surface, and one secondary patterning rail (high rail, or HR), 500 μm apart from the bottom surface (Figure 4.1b). The rail-based microstructures allowed spatially compartmented hydrogel patterning to be performed by a simple and fast patterning process (Figure 4.2). First, the surfaces of the device are hydrophilically modified via air plasma treatment. Next, hydrogel pre-solution was injected through an injection hole to fill the entire microstructures (Figure 4.2a), and subsequently aspirated away by pipetting. Due to the hydrophilicity of the surfaces, only hydrogel pre-solution underneath LR regions remained (Figure 4.2b). Importantly, this process can be performed for 12 wells in a slide within 30 s. After crosslinking the hydrogel underneath LR regions, the second solution was loaded underneath the HR region to form two separate compartments (Figure 4.2c). Compared with the PDMS devices widely used in microfluidics that requires tedious batch processes for fabrication, this injection molding-based device can substantially

enhance throughput of the assay because the devices can be massively produced. In addition, hydrophilic rail-based microstructures permit hydrogel patterning to be conducted by simple pipetting, thus entire devices can be readily fabricated without requiring any sophisticated equipment/techniques.

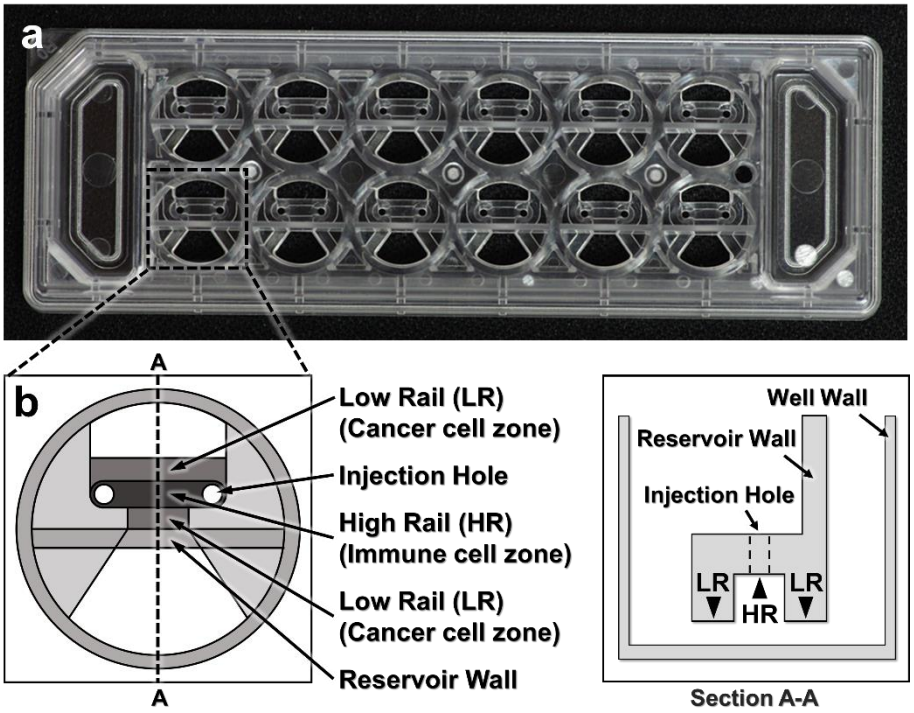

Figure 4.1. A CACI-IMPACT platform and its working process. (a) Rail-based microstructures are embedded in microwells with 96 well plate format and the structures are integrated in a 2 x 6 rectangular array. Water tanks are allocated in both sides to maintain humidity in samples. (b) Schematic top and section view of a single well. The microstructure in a single well consists of two low rails (LRs) for primary hydrogel patterning and one high rail (HR) to form a channel for secondary fluid patterning after hydrogel cross-linking.

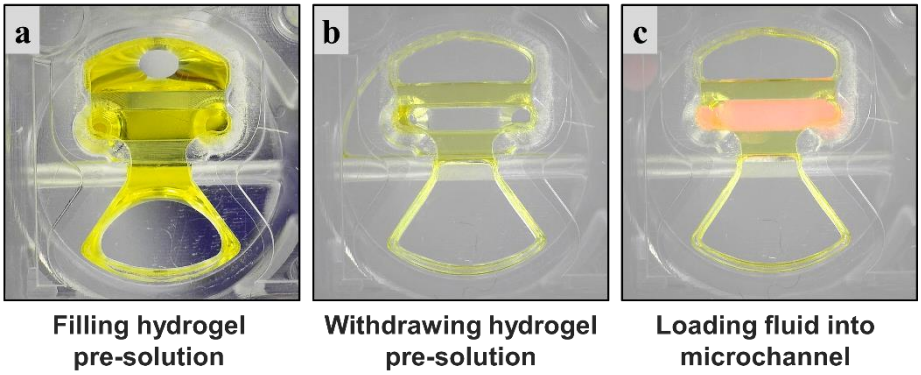

Figure 4.2. Procedure of using the device. Once a hydrogel pre-solution is filled and withdrawn through an injection hole, the solution remains only underneath LRs. When the hydrogel is cross-linked, a microfluidic channel is formed where another fluid can be loaded.

4.3.2. Cytotoxicity assay in 3D ECM environment

Using the hydrogel patterning technique, we first fabricated collagen gels encapsulating HeLa cells underneath LR regions (Figure 4.3a Day 0), and cultured for one day. Then, NK-92 cell suspension was loaded next to the collagen gel, and the device was tilted to 90o for 20 min to accumulate NK-92 cells on one side of the collagen gel by sedimentation (Figure 4.3a Day 1). NK-92 cells attached on the collagen gel surfaces penetrated into collagen gel blocks and migrated toward HeLa cells to exert cytotoxicity. Figure 4.3b shows the initial state of the assay on Day 1.

HeLa cells and NK-92 cells were labeled with two distinct fluorophores, and propidium iodide (PI), a fluorescence dye labeling dead cells, was added in the media to visualize dead cells. In this way, we can simultaneously observe NK-92 cell migration and cytotoxicity along the collagen matrix containing HeLa cells by live imaging (Figure 4.4 and 4.5). NK-92 cells uniformly deposited on collagen block at the beginning of imaging penetrated and migrated into collagen matrix as shown in time-lapse images acquired with a low magnification objective lens (Figure 4.4). As NK-92 cells propagated into collagen gels, PI-stained HeLa cells near NK-92 cells increased, meaning NK-92 cells

exerted cytotoxicity against HeLa cells in collagen gels. Detailed procedures in CL-mediated cytotoxicity of cancer cells, rounding by detachment and subsequent membrane permeabilization allowing PI incorporation (*129*), can be visualized by time-lapse images using a high magnification objective lens: CFSE-labeled HeLa cells turned round after they made contact with NK-92 cells, followed by PI uptake (Figure 4.5).

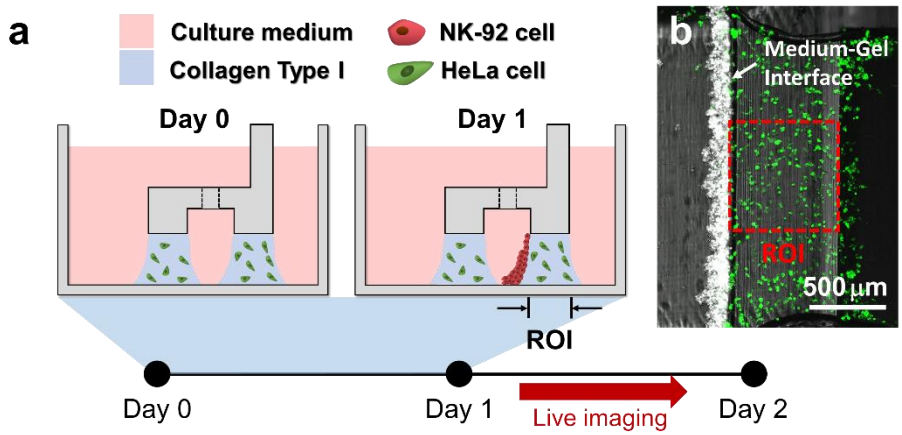

Figure 4.3. Procedure of 3D cytotoxicity assay and its outputs. (a) Schematic process of the assay. HeLa cells embedded in collagen were patterned under low rails (Day 0). After 24 hours of cultivation, NK-92 cells were loaded into a microchannel formed by the hydrogel. By tilting the device at an angle of 90 degrees, NK-92 cells were deposited on a collagen block (Day 1) and cultured for additional 24 hours to observe migration and cytotoxic activity of NK cells. (b) Initial state of the assay (Day 1).

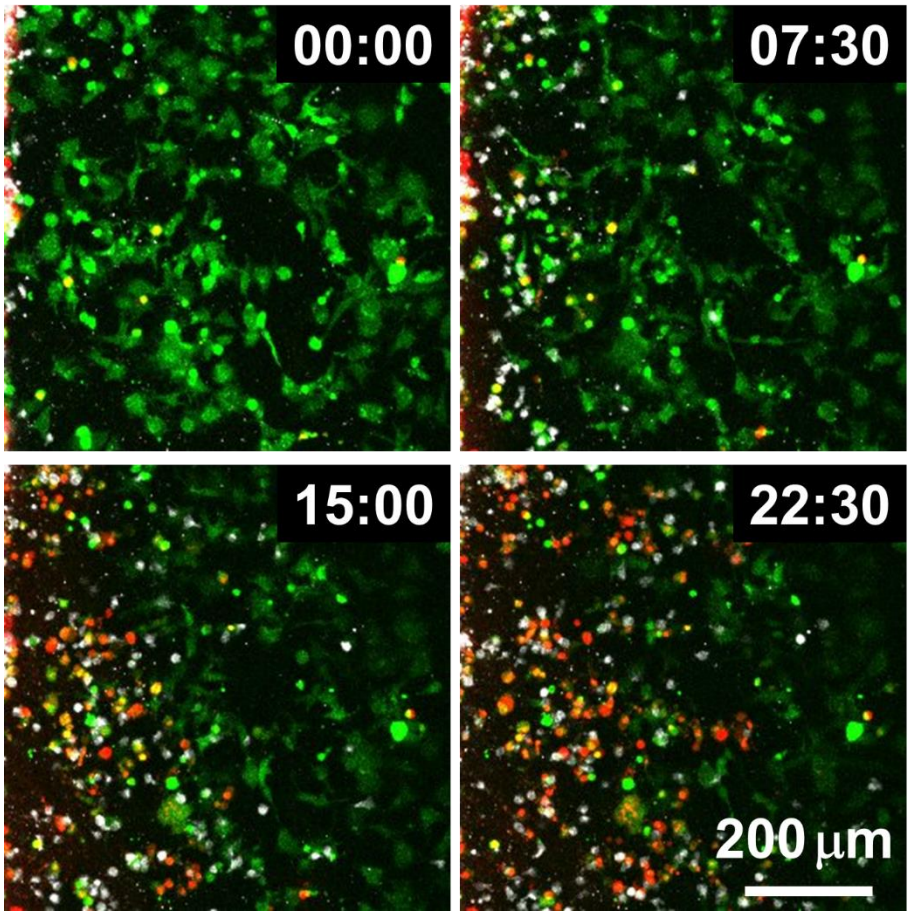

Figure 4.4. Live monitoring of migration and cytotoxic activity of NK-92 cells with 10X objective lens. NK-92 cells (white) penetrate into collagen matrix where HeLa cells are encapsulated. Propidium iodide (Red) displays dead cells. Time is indicated in HH:MM in the top right corner of each image.

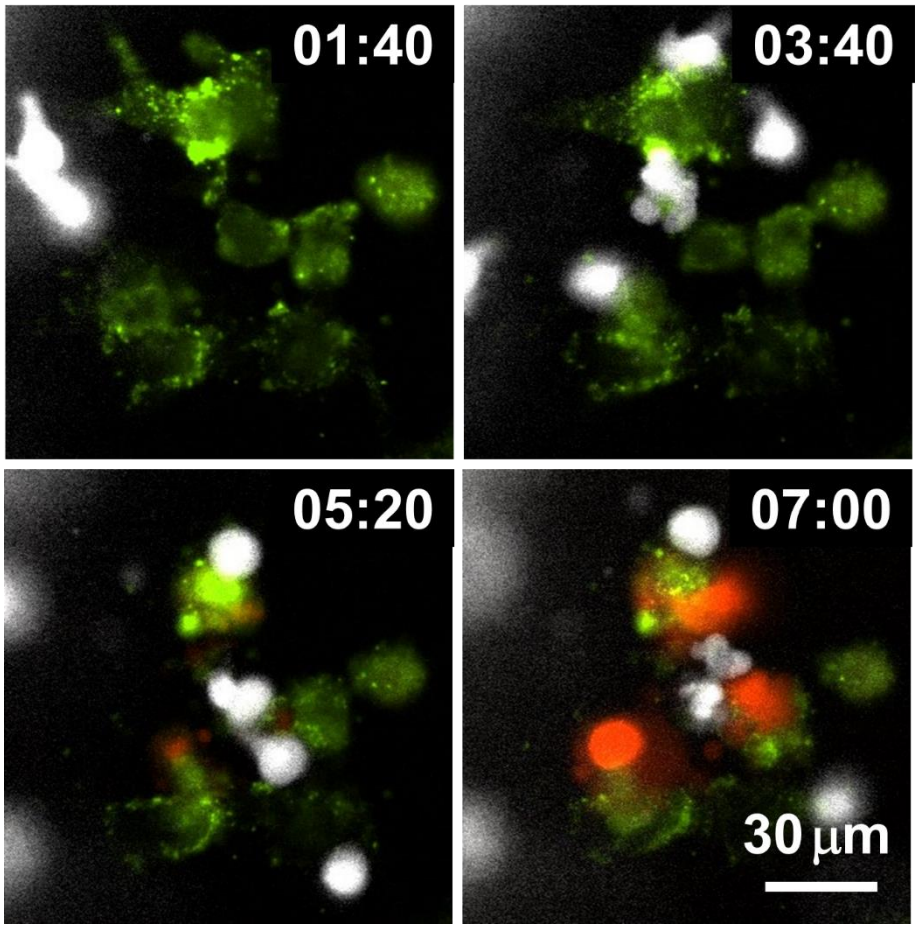

Figure 4.5. Live monitoring of migration and cytotoxic activity of NK-92 cells with 20X objective lens. NK-92 cells (white) penetrate into collagen matrix where HeLa cells are encapsulated. Propidium iodide (Red) displays dead cells. Time is indicated in HH:MM in the top right corner of each image.

4.3.3. 3D ECM reduce cytotoxicity

With this experimental setting, we first investigated how the presence of ECM and the density of cancer cells influenced NK cell cytotoxicity. HeLa cells in two different cell densities (0.8 x 10^6 cells/ml and 3.2 x 10^6 cells/ml) were encapsulated in collagen gels (3 mg/ml) while the NK-92 cell density added in the media was fixed (2.0 x 10^6 cells/ml), thus effectively total NK-92:HeLa were 5:1 and 20:1, typical ratio used for conventional cytotoxicity assays. Fluorescence images of square region of interest (ROI) with a side length of 700 μm, which is the dimension of the low rail width under which NK cells interact with HeLa cells, were acquired using a motorized stage 24 h after NK-92 cell seeding. The ROI was divided into seven sub-regions with a width of 100 μm, R0 to R6 (Figure 4.6). The number of NK cells penetrated into the collagen gels and the percentage of killed HeLa cells, or PI-labeled HeLa cells, in each sub-region were measured and plotted (Figure 4.7a and 4.7b). R0 and R6 were not considered because they were located near the interface between collagen gel and liquid media where capillary force-mediated meniscus formed (Figure 4.6), thus boundaries were not clearly defined in some cases.

NK-92 cell number was the highest in R1, and gradually decreased

as the sub-region became deeper (Figure 4.7a). NK-92 cells exhibited significantly higher cell numbers in all sub-regions for the lower HeLa cell density, or 20:1, than the case of 5:1 except for R1 (Figure 4.7a). Similar trends were observed for HeLa cell killing, as HeLa cell killing requires close proximity of NK-92 cells and HeLa cells (Figure 4.7b). These results indicate that HeLa cells in collagen gels hold NK-92 cells nearby by forming dynamic immunological synapses (*130*), thus NK-92 cell migration toward deeper sub-regions gets delayed until they kill substantial fraction of HeLa cells. Percentages of killed HeLa cells in entire sub-regions R1-R5 were measured and compared with 2D cytotoxicity assays performed with equivalent NK-92:HeLa ratio. In 2D, NK-92 cells killed ~ 90% of HeLa cells regardless of the ratio, whereas significantly lower percentage of HeLa cells were killed in 3D, and the higher HeLa cell killing occurred with the NK-92:HeLa ratio of 20:1. These results indicate that accessibility of cancer cells is a limiting factor, and migration of CLs is a rate limiting step in cytotoxicity in 3D ECM microenvironments.

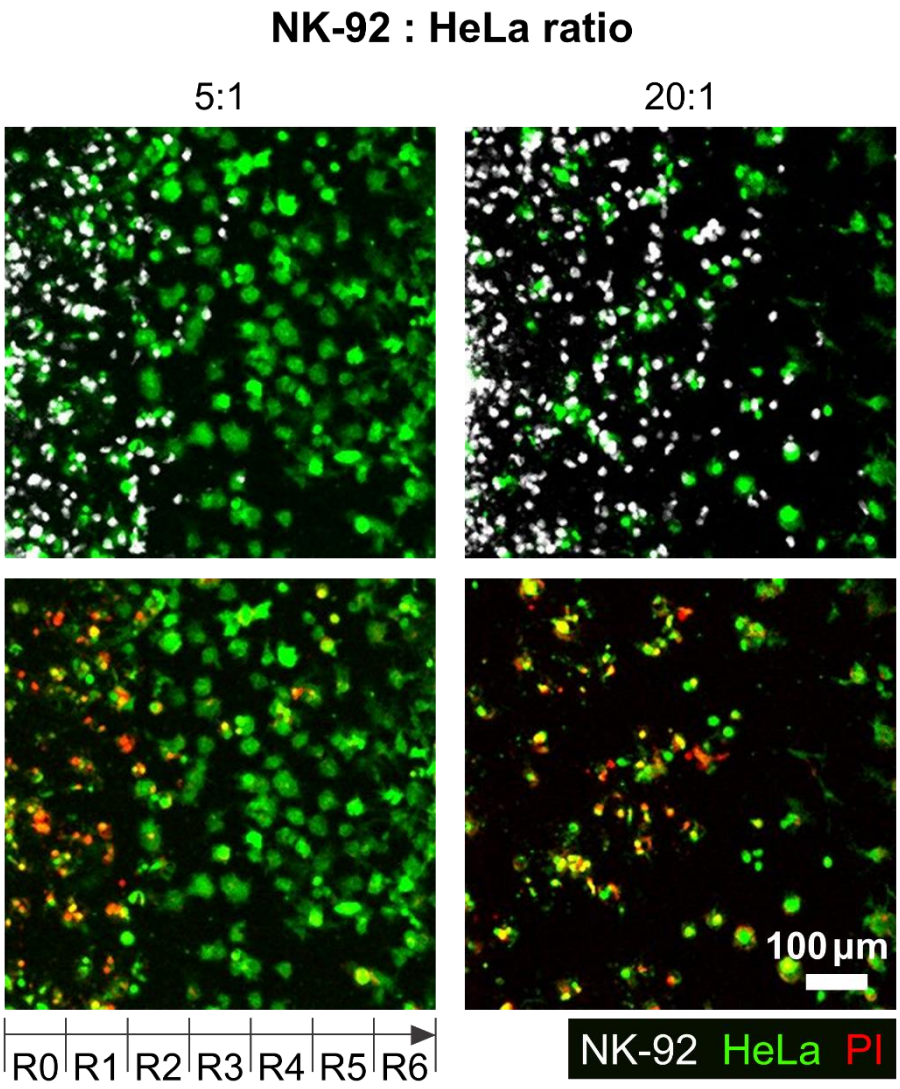

Figure 4.6. Images taken after 24 hours of interaction of NK cells and HeLa cells in two NK-92:HeLa ratios. HeLa cells (green) and NK-92 cells (white) are displayed in upper images and lower images show live/dead HeLa cells at the same moment with the upper images.

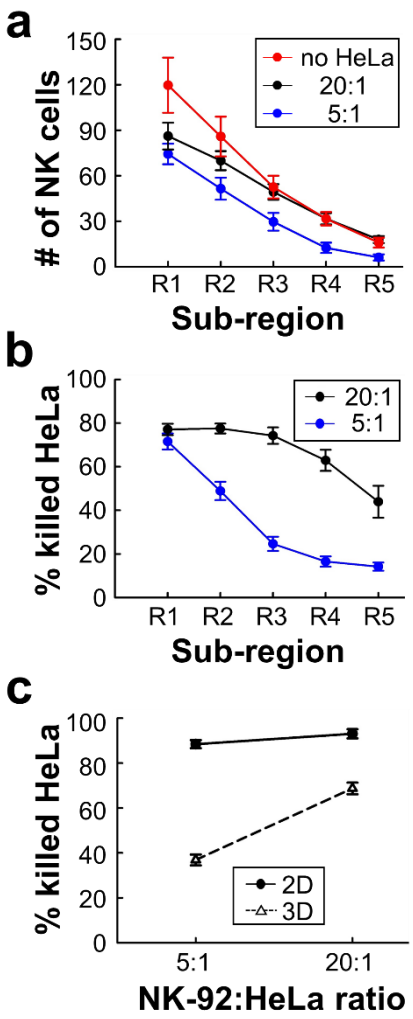

Figure 4.7. 3D ECM reduces cytotoxicity by limiting cancer cell accessibility. (a) The numbers of NK cells and (b) the percentage of killed HeLa cells within the ROI sub-regions in the two NK-92:HeLa ratios ($n \geq 18$). (c) The percentage of killed HeLa cells within the whole ROI from R1 to R5 in the two NK-92:HeLa ratios. ($n = 3$ for 2D assay, $n \geq 18$ for 3D assay). Dot plots in (b)-(d) show mean ± SEM.

4.3.4. Dense ECM impede migration of CLs

In many solid tumors, fibrosis characterized by dense and stiff ECM generation occurs surrounding areas of tumor cells. Fibrosis not only affects cancer cells by triggering various mechanotransduction pathways by stiffening ECM (*131*), but also influences immunotherapy efficacy by limiting CL infiltration into tumors (*114, 132*). We sought to investigate the role of ECM density, a key component of fibrosis, on lymphocyte cytotoxicity in 3D by using the device patterned with various concentrations of collagen (2, 3, 4 mg/ml). Effective NK-92:HeLa ratio was fixed to 5:1. Representative still images of the patterned collagen gels with various collagen concentrations 24 h after NK-92 cell seeding are shown in Figure 4.8. NK-92 cells distributed throughout the collagen gels in 2 mg/ml of collagen gel, whereas few NK-92 cells were observed in R4-R6 in 4 mg/ml of collagen gel. Overall, NK cell number was the highest in R1 and gradually decreased as the sub-region became deeper for all collagen concentrations (Figure 4.9a), and NK cell number was the highest for the lowest collagen concentration and gradually decreased as the collagen concentration increased for all sub-regions (Figure 4.9a). Similar trends in the percentage of killed HeLa cells were observed (Figure 4.9b). These results indicate that ECM density plays an important

role in NK cell migration in collagen gels, and consequently affects NK cell cytotoxicity.

Next, we investigated detailed interactions between NK-92 cells and HeLa cells encapsulated in different concentrations of collagen. By performing time-lapse imaging, we directly visualized NK-92 cell-HeLa cell interactions at a single cell level (Figure 4.10), and assessed how much time is needed for each NK-92 cell to successfully kill HeLa cells. Time for killing, which measures time from initial NK-92/HeLa contact to PI uptake in HeLa cells, was measured for each NK-92 cell successfully killed NK-92 cell and plotted for NK-92 cells in collagen gels with 2 and 4 mg/ml (Figure 4.11). Interestingly, time for killing of NK-92 cells in 4 mg/ml collagen gels was significantly lower than that of NK-92 cells in 2 mg/ml collagen gels. This result indicates that cytotoxicity of individual NK-92 cells is higher in higher concentration of collagen gels. Taken together, ECM density can influence both migration and cytotoxicity of CLs.

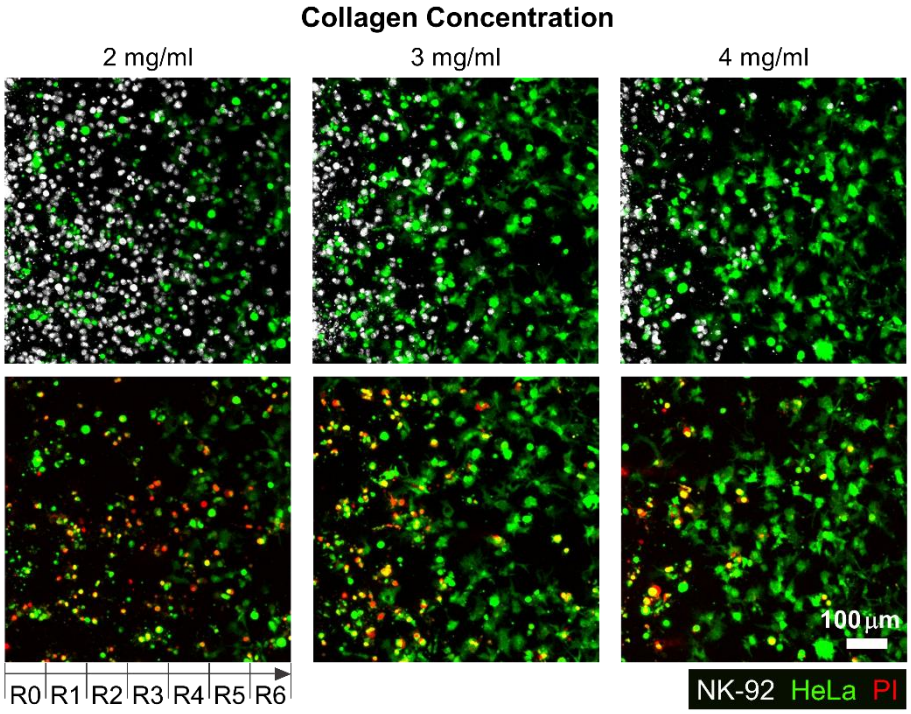

Figure 4.8. Images taken after 24 hours of interaction of NK cells and HeLa cells in three collagen concentrations. HeLa cells (green) and NK-92 cells (white) are displayed in upper images and lower images show live/dead HeLa cells at the same moment with upper images.

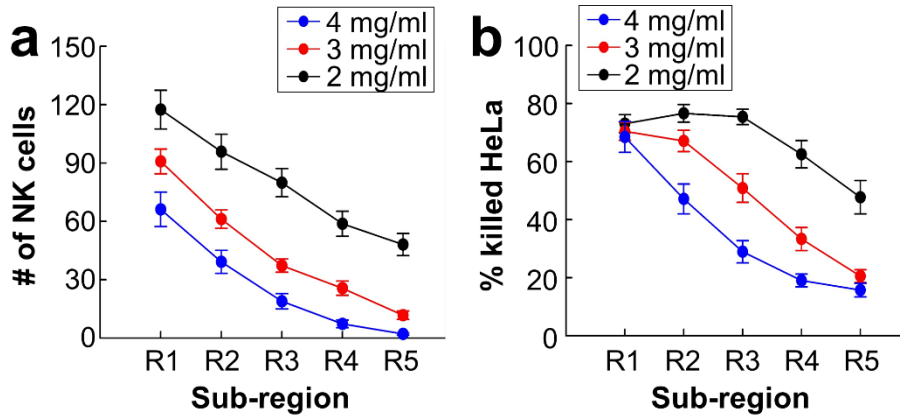

Figure 4.9. Dense ECM impedes cytotoxic activity of NK cells. (a) The numbers of NK cells and (b) the percentage of killed HeLa cells within the ROI sub-regions ($n \geq 16$).

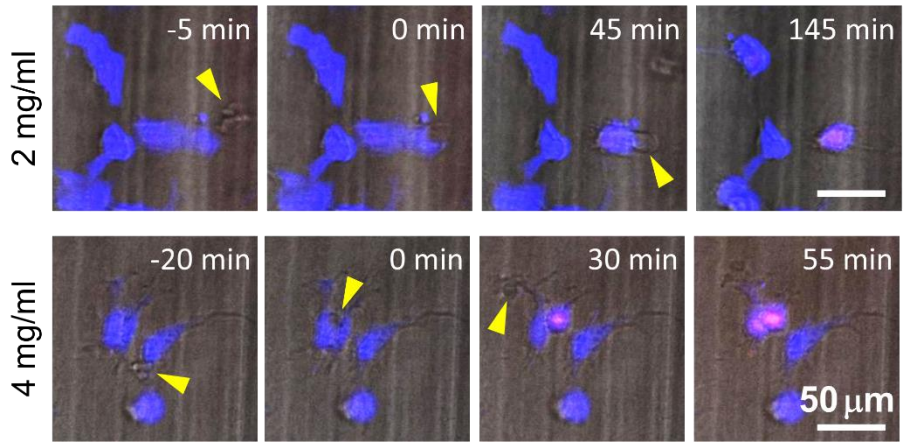

Figure 4.10. Live monitoring of cytotoxic activities of NK-92 cells (Yellow arrows) against HeLa cells (Blue). Propidium iodide (Red) shows the death of HeLa cells.

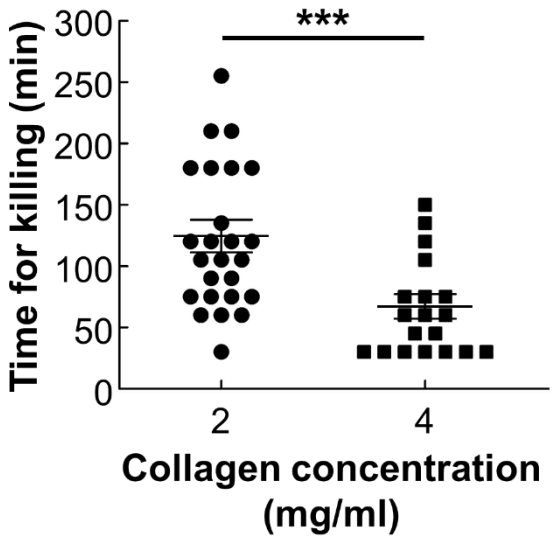

Figure 4.11. PI uptake time from the moment that NK-92 cells made a contact with HeLa cells in 2 and 4 mg/ml of collagens. Each dot was obtained from a single HeLa cell killed by a single NK-92 cell. For statistical comparison, unpaired two-tailed Student's t-test was performed, and the statistical significance was displayed as follows; *$p < 0.05$, **$p < 0.01$, ***$p < 0.001$.

4.4. Conclusions

Traditional *in vitro* 2D cytotoxicity assays against cancer cells have been widely used to evaluate *ex vivo* engineered or cultured CLs due to simplicity in assays, but the assay results may not be consistent with *in vivo* results due to the absence of 3D tumor microenvironment (TME). PDMS-based microfluidic devices recapitulating various aspects of TME, including hypoxia, inflammatory cytokines, immunosuppressive conditions, and vasculatures, have been developed to evaluate CLs in 3D (*125*-*127*).

However, PDMS-based devices require labor and time intensive batch fabrication processes, thus device fabrication limits experimental throughputs (*128*). To overcome this limitation, the CACI-IMPACT devices used in this study were massively produced using injection molding with polystyrene (PS) by customizing the design of the IMPACT device (*99*), which was previously developed by our group for 3D compartmentalized cell culture. In our experience of conducting the same 3D cytotoxicity assays using our PDMS-based co-culture device (*93*), approximately two days of serial processes, including casting (7 h), punching (1 h), bonding (10 m), and surface hydrophobicity restoration (> 1 d), were required. The series of manual processes can cause defects,

resulting in lower yields or lower uniformity of the final devices to be used in experiments. Furthermore, pressure sensitive loading process in PDMS device reduces usability and experimental throughput. In sharp contrast, CACI-IMPACT device requires less than 10 minutes for device preparation including 3 min of hydrophilic surface modification. In case that the device was packed after plasma treatment, no preparation is required except opening the packaging. Rail-based microstructures with hydrophilic surfaces further facilitated experiments by enabling simple and fast hydrogel patterning to be performed, and multi-well format further enhanced experimental throughputs by allowing multiple experiments to be performed simultaneously in a single device. In addition to improved device fabrication and experimental throughputs, long term monitoring of CL-cancer cell interactions is possible, as media change can be readily performed by aspirating media in the media reservoir and filling new media without perturbing hydrogels containing cells.

Using the injection molded devices, we performed 3D cytotoxicity assays with various density of cancer cells and various collagen concentrations. First, we found the presence of ECM and cancer cells could significantly reduce cytotoxicity of CLs by impeding

migration and limiting accessibility of cancer cells compared with 2D cytotoxicity assays (Figure 4.7). Presence of cancer cells in ECM may play dual role in cytotoxicity: it may impede infiltration of CL by interacting with CLs as we have shown, but at the same time, cancer cells can promote CL migration by producing chemokines such as CXCL9, 10, and 11 (*133*). As shown in Figure 4.7a, NK-92 cell distribution in collagen gels lacking HeLa cells (no HeLa) was comparable to that in collagen gels with low density of HeLa cells (20:1) except for entry regions, where NK-92 cell numbers were slightly higher for collagen gels lacking HeLa cells, indicating chemotaxis-mediated NK-92 cell migration was minimal in our system. Second, we found ECM density played an important role in 3D cytotoxicity by independently regulating migration-mediated cancer cell contact and direct cancer cell killing (Figure 4.9). Indeed, collagen density can influence various physical properties of collagen gels such as pore size and stiffness (*134*). When collagen concentration was increased, NK cell infiltration into collagen gels was substantially reduced presumably due to reduced pore size that limits amoeboid-mode immune cell migration (*135*). Indeed, increased ECM density observed in fibrotic tumors reduced activity of T cells by limiting physical access of tumor cells (*119*), indicating our device may

be a good model system to evaluate *ex vivo* engineered CLs for fibrotic tumors. Interestingly, cytotoxicity of individual NK cells were significantly enhanced when collagen concentration was increased (Figure 4.11). While detailed mechanisms for enhanced cytotoxicity in collagen-dense environments need to be determined, it is possible that stiff ECM environments in high concentration of collagen facilitate tumor cell lysis by increasing tumor cell tension, which enhances perforin-mediated pore formation on tumor cell membrane (*136*).

Our preliminary 3D cytotoxicity assay using human primary NK cells revealed that CACI-IMPACT platform can be used for primary lymphocytes, while detailed assay conditions need to be adjusted depending on cell types (Figure 4.12). Primary NK cells exhibited much higher motility and cytotoxicity compared with NK-92 cells: they uniformly distributed in entire collagen gels (Figure 4.12b) and killed the majority of HeLa cells (Figure 4.12c) within 12 h in dense ECM (4mg/ml of collagen), in which NK-92 cells killed only ~ 40% of HeLa cells for 24 h (Figure 4.9b). Superior cytotoxicity of primary NK cells in our assay is partly due to smaller size of primary NK cells (diameter ~ 8 μm) compared with that of NK-92 cells (diameter ~ 14 μm), which plays important role in cell migration in dense ECM (*134*), further confirming

importance of lymphocyte motility in 3D cytotoxicity.

To sum up, we introduced an injection molded microfluidic device for assessing cytotoxicity of CLs in 3D environment. The proposed device is characterized by (i) enhanced productivity via injection molding, (ii) enhanced experimental throughput mediated by multi-well format of the device, and (iii) hydrophilic rail-based microstructures facilitating hydrogel patterning with simple pipetting. Using the device, we found 3D ECM significantly reduce cytotoxicity of CLs by impeding migration and access to tumor cells compared with traditional 2D assays. We also found denser ECM impede migration of CLs but enable effective killing once CLs contact with tumor cells. The results show how important the presence of ECM is for accessing cytotoxicity of CLs against solid tumors. We think this injection molded 3D culture platform could be used to evaluate cytotoxicity of CLs in 3D environment and to identify new therapeutic approaches mediated by adoptive transferred CLs against solid tumors.

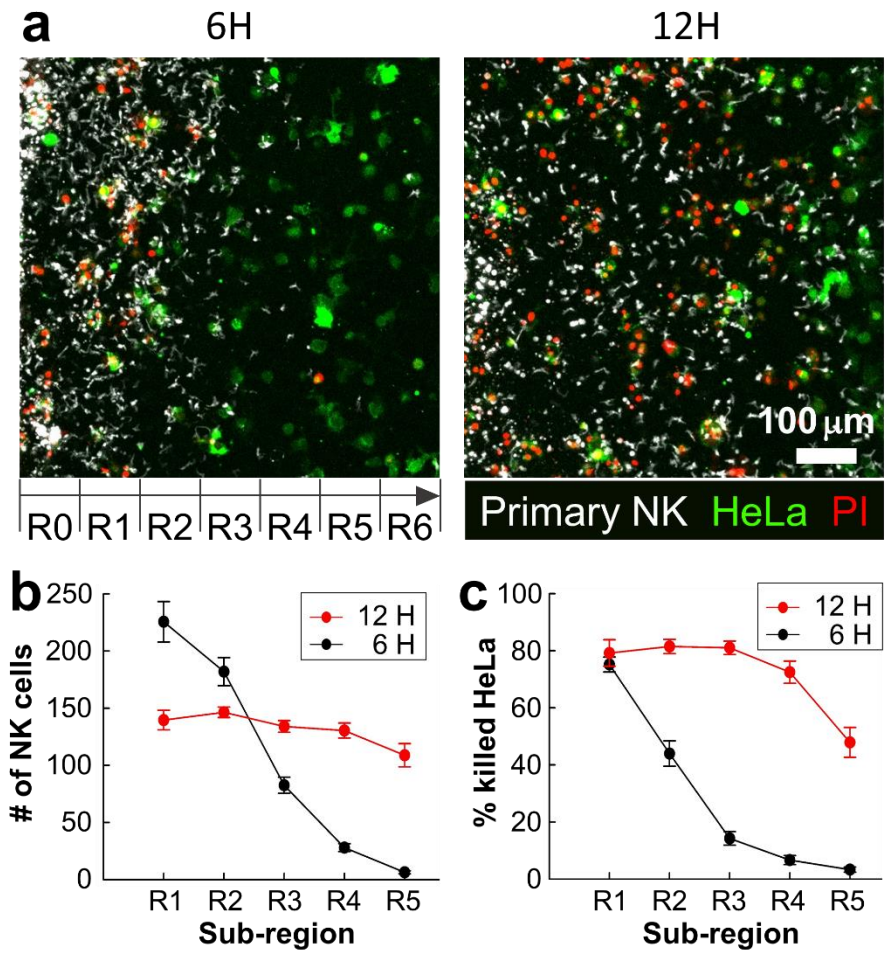

Figure 4.12. 3D cytotoxicity assay performed with primary NK cells against HeLa cells. (A) Representative images taken after 6H (left) and 12H (right) of primary NK/HeLa cells co-culture. (B) The number of primary NK cells and (C) the percentage of killed HeLa cells within the ROI sub-regions after 6H (black) and 12H (red) of primary NK/HeLa cells co-culture.

Chapter 5. Concluding Remarks

In this thesis, we suggested two CGP methods by integrating microstructures with conventional cell culturewares. In chapter 2, micropillar array embossed on petri-dish enabled multiscale liquid patterning by sweeping bulk liquid over the surface. The patterning mechanism on a basic form of a 2 × 2 rectangular array of circular pillars is analyzed theoretically and verified with experiments. Nanoliter-to-microliter volumes of liquids are patterned into various shapes by arranging the pillars based on the analysis. Furthermore, an array of geometrically modified pillars can capture approximately 8000 droplets on a large substrate (55 mm × 55 mm) in one step. Given the simplistic method of wipe patterning, the proposed platform can be utilized in both manual benchtop and automated settings. We will provide proof of concept experiments of single colony isolation using nanoliter-scale liquid patterning and of human angiogenic vessel formation using sequential patterning of microliter-scale liquids.

In chapter 3, rail-based microstructure was introduced to guide air-liquid interface retrieved by aspiration, resulting in remaining hydrogels only under low rails. We provide a design rule for the device structure

and the capillary pressure condition upon verifying a theoretical model to explain the physical principle. We demonstrate formation of multiple hollow channels or hydrogel islands with a single aspiration. Then we test vasculogenic capacity of various cell types using a microfluidic co-culture system obtained by our technology, to illustrate its capabilities as a viable micro-manufacturing scheme for high-throughput cellular co-culture.

In chapter 4, we introduced a 3D cytotoxicity assay to assess cytotoxicity of lymphocytes in 3D microenvironment in high-throughput fashions. Rail-based microfluidic design described in chapter 3 was integrated within a single 96-well and the wells were rectangularly arrayed in 2 × 6 to enhance the experimental throughput. The rail-based microstructures facilitate hydrogel patterning with simple pipetting so that hydrogel pre-solution aspirated with 10 μl pipette can be patterned in 12 wells within 30 s. To demonstrate 3D cytotoxicity assay, we patterned HeLa cells encapsulated by collagen gel and observed infiltration, migration and cytotoxic activity of NK-92 cells against HeLa cells in the collagen matrix. We found that 3D ECM significantly reduced migration of cytotoxic lymphocytes and access to cancer cells, resulting in lower cytotoxicity compared with 2D assays.

Compared with traditional closed microfluidic devices made with PDMS, the open microfluidic platforms utilizing CGP methods (i) are scalable, (ii) have enhanced experimental throughput, (iii) are compatible with automated liquid dispenser or imaging systems due to their standardized format, and (iv) are highly accessible to the cultured tissue. We expect open microfluidic devices introduced so far can address limitations that impede commercialization of organs-on-chips and help organs-on-chips to be used in industry such as pre-clinical drug screening and developmental process of drugs or cosmetics.

Bibliography

1. C. D. Chin, V. Linder, S. K. Sia, Commercialization of microfluidic point-of-care diagnostic devices. *Lab Chip* **12**, 2118-2134 (2012).
2. S. Kim, H. J. Kim, N. L. Jeon, Biological applications of microfluidic gradient devices. *Integr Biol (Camb)* **2**, 584-603 (2010).
3. P. Shrimal, G. Jadeja, S. Patel, A review on novel methodologies for drug nanoparticle preparation: Microfluidic approach. *Chemical Engineering Research and Design* **153**, 728-756 (2020).
4. P. Sajeesh, A. K. Sen, Particle separation and sorting in microfluidic devices: a review. *Microfluidics and Nanofluidics* **17**, 1-52 (2013).
5. S. Halldorsson, E. Lucumi, R. Gomez-Sjoberg, R. M. T. Fleming, Advantages and challenges of microfluidic cell culture in polydimethylsiloxane devices. *Biosens Bioelectron* **63**, 218-231 (2015).
6. D. Di Carlo, L. P. Lee, Dynamic single-cell analysis for quantitative biology. *Analytical chemistry* **78**, 7918-7925 (2006).
7. J. Fu *et al.*, Mechanical regulation of cell function with geometrically modulated elastomeric substrates. *Nat Methods* **7**, 733-736 (2010).
8. D. Huh *et al.*, Reconstituting organ-level lung functions on a chip. *Science* **328**, 1662-1668 (2010).
9. H. Cho, H. Y. Kim, J. Y. Kang, T. S. Kim, How the capillary burst microvalve works. *J Colloid Interface Sci* **306**, 379-385 (2007).
10. T. E. Park *et al.*, Hypoxia-enhanced Blood-Brain Barrier Chip recapitulates human barrier function and shuttling of drugs and antibodies. *Nat Commun* **10**, 2621 (2019).
11. H. J. Kim, D. Huh, G. Hamilton, D. E. Ingber, Human gut-on-a-chip inhabited by microbial flora that experiences intestinal peristalsis-like motions and flow. *Lab Chip* **12**, 2165-2174 (2012).
12. N. Jusoh, S. Oh, S. Kim, J. Kim, N. L. Jeon, Microfluidic vascularized bone tissue model with hydroxyapatite-incorporated extracellular matrix. *Lab Chip* **15**, 3984-3988 (2015).

13. K. H. Benam *et al.*, Small airway-on-a-chip enables analysis of human lung inflammation and drug responses in vitro. *Nat Methods* **13**, 151-157 (2016).
14. K. J. Jang *et al.*, Human kidney proximal tubule-on-a-chip for drug transport and nephrotoxicity assessment. *Integr Biol (Camb)* **5**, 1119-1129 (2013).
15. C. D. Edington *et al.*, Interconnected Microphysiological Systems for Quantitative Biology and Pharmacology Studies. *Sci Rep* **8**, 4530 (2018).
16. I. Maschmeyer *et al.*, A four-organ-chip for interconnected long-term co-culture of human intestine, liver, skin and kidney equivalents. *Lab Chip* **15**, 2688-2699 (2015).
17. J. Vriend *et al.*, Flow stimulates drug transport in a human kidney proximal tubule-on-a-chip independent of primary cilia. *Biochim Biophys Acta Gen Subj* **1864**, 129433 (2020).
18. N. R. Wevers *et al.*, A perfused human blood-brain barrier on-a-chip for high-throughput assessment of barrier function and antibody transport. *Fluids Barriers CNS* **15**, 23 (2018).
19. C. Beaurivage *et al.*, Development of a Gut-On-A-Chip Model for High Throughput Disease Modeling and Drug Discovery. *Int J Mol Sci* **20**, (2019).
20. A. Petrosyan *et al.*, A glomerulus-on-a-chip to recapitulate the human glomerular filtration barrier. *Nat Commun* **10**, 3656 (2019).
21. M. B. Chen *et al.*, On-chip human microvasculature assay for visualization and quantification of tumor cell extravasation dynamics. *Nat Protoc* **12**, 865-880 (2017).
22. D. Huh *et al.*, Microfabrication of human organs-on-chips. *Nat Protoc* **8**, 2135-2157 (2013).
23. C. P. Huang *et al.*, Engineering microscale cellular niches for three-dimensional multicellular co-cultures. *Lab Chip* **9**, 1740-1748 (2009).
24. P. Vulto *et al.*, Phaseguides: a paradigm shift in microfluidic priming and emptying. *Lab Chip* **11**, 1596-1602 (2011).
25. H. van Heeren, R. Tantra, P. Salomon, Microfluidic devices: a road forward by standardization of interconnects and classification. *Microfluidics and Nanofluidics* **19**, 1203-1207 (2015).
26. S. B. Berry *et al.*, Upgrading well plates using open microfluidic patterning. *Lab*

Chip **17**, 4253-4264 (2017).

27. A. R. Aref *et al.*, 3D microfluidic ex vivo culture of organotypic tumor spheroids to model immune checkpoint blockade. *Lab on a chip* **18**, 3129-3143 (2018).
28. D. T. Le *et al.*, PD-1 Blockade in Tumors with Mismatch-Repair Deficiency. *N Engl J Med* **372**, 2509-2520 (2015).
29. J. Kaiser, Too much of a good thing? *Science* **359**, 1346-1347 (2018).
30. P. S. Hegde, D. S. Chen, Top 10 Challenges in Cancer Immunotherapy. *Immunity* **52**, 17-35 (2020).
31. A. Zloza *et al.*, Workshop on challenges, insights, and future directions for mouse and humanized models in cancer immunology and immunotherapy: a report from the associated programs of the 2016 annual meeting for the Society for Immunotherapy of cancer. *J Immunother Cancer* **5**, 77 (2017).
32. S. N. Bailey, D. M. Sabatini, B. R. Stockwell, Microarrays of small molecules embedded in biodegradable polymers for use in mammalian cell-based screens. *Proceedings of the National Academy of Sciences of the United States of America* **101**, 16144-16149 (2004).
33. J. E. Bradner *et al.*, A robust small-molecule microarray platform for screening cell lysates. *Chem Biol* **13**, 493-504 (2006).
34. R. A. Lindquist *et al.*, Genome-scale RNAi on living-cell microarrays identifies novel regulators of Drosophila melanogaster TORC1-S6K pathway signaling. *Genome Res* **21**, 433-446 (2011).
35. D. J. Siegwart *et al.*, Combinatorial synthesis of chemically diverse core-shell nanoparticles for intracellular delivery. *Proceedings of the National Academy of Sciences of the United States of America* **108**, 12996-13001 (2011).
36. J. Ziauddin, D. M. Sabatini, Microarrays of cells expressing defined cDNAs. *Nature* **411**, 107-110 (2001).
37. C. J. Flaim, S. Chien, S. N. Bhatia, An extracellular matrix microarray for probing cellular differentiation. *Nature methods* **2**, 119-125 (2005).
38. A. Huebner *et al.*, Quantitative detection of protein expression in single cells using droplet microfluidics. *Chem Commun (Camb)*, 1218-1220 (2007).
39. V. Chokkalingam *et al.*, Probing cellular heterogeneity in cytokine-secreting immune cells using droplet-based microfluidics. *Lab on a chip* **13**, 4740-4744

(2013).

40. S. L. Sjostrom *et al.*, High-throughput screening for industrial enzyme production hosts by droplet microfluidics. *Lab on a chip* **14**, 806-813 (2014).
41. H. F. Chan, Y. Zhang, K. W. Leong, Efficient One-Step Production of Microencapsulated Hepatocyte Spheroids with Enhanced Functions. *Small* **12**, 2720-2730 (2016).
42. Q. Chen *et al.*, Controlled assembly of heterotypic cells in a core-shell scaffold: organ in a droplet. *Lab on a chip* **16**, 1346-1349 (2016).
43. J. C. Baret *et al.*, Fluorescence-activated droplet sorting (FADS): efficient microfluidic cell sorting based on enzymatic activity. *Lab on a chip* **9**, 1850-1858 (2009).
44. M. T. Guo, A. Rotem, J. A. Heyman, D. A. Weitz, Droplet microfluidics for high-throughput biological assays. *Lab on a chip* **12**, 2146-2155 (2012).
45. E. Ueda, F. L. Geyer, V. Nedashkivska, P. A. Levkin, DropletMicroarray: facile formation of arrays of microdroplets and hydrogel micropads for cell screening applications. *Lab on a chip* **12**, 5218-5224 (2012).
46. A. N. Efremov, E. Stanganello, A. Welle, S. Scholpp, P. A. Levkin, Micropatterned superhydrophobic structures for the simultaneous culture of multiple cell types and the study of cell-cell communication. *Biomaterials* **34**, 1757-1763 (2013).
47. A. A. Popova *et al.*, Droplet-Array (DA) Sandwich Chip: A Versatile Platform for High-Throughput Cell Screening Based on Superhydrophobic-Superhydrophilic Micropatterning. *Adv Mater* **27**, 5217-5222 (2015).
48. A. I. Neto *et al.*, Fabrication of Hydrogel Particles of Defined Shapes Using Superhydrophobic-Hydrophilic Micropatterns. *Adv Mater* **28**, 7613-7619 (2016).
49. E. Kim, Y. N. Xia, X. M. Zhao, G. M. Whitesides, Solvent-assisted microcontact molding: A convenient method for fabricating three-dimensional structures on surfaces of polymers. *Adv Mater* **9**, 651-654 (1997).
50. J. Bico, U. Thiele, D. Quéré, Wetting of textured surfaces. *Colloids and Surfaces A: Physicochemical and Engineering Aspects* **206**, 41-46 (2002).
51. C. Semprebon, P. Forsberg, C. Priest, M. Brinkmann, Pinning and wicking in regular pillar arrays. *Soft Matter* **10**, 5739-5748 (2014).
52. S. J. Kim *et al.*, Liquid spreading on superhydrophilic micropillar arrays. *Journal*

of Fluid Mechanics **680**, 477-487 (2011).

53. S. J. Kim, J. Kim, M.-W. Moon, K.-R. Lee, H.-Y. Kim, Experimental study of drop spreading on textured superhydrophilic surfaces. *Physics of Fluids* **25**, 092110 (2013).
54. T. Podgorski, J. M. Flesselles, L. Limat, Corners, cusps, and pearls in running drops. *Physical review letters* **87**, 036102 (2001).
55. S. Ni, J. Leemann, I. Buttinoni, L. Isa, H. Wolf, Programmable colloidal molecules from sequential capillarity-assisted particle assembly. *Sci Adv* **2**, e1501779 (2016).
56. F. Brochard-Wyart, P. G. de Gennes, Dynamics of partial wetting. *Advances in Colloid and Interface Science* **39**, 1-11 (1992).
57. H.-Y. Kim, On Thermocapillary Propulsion of Microliquid Slug. *Nanoscale and Microscale Thermophysical Engineering* **11**, 351-362 (2007).
58. J. C. Love, J. L. Ronan, G. M. Grotenbreg, A. G. van der Veen, H. L. Ploegh, A microengraving method for rapid selection of single cells producing antigen-specific antibodies. *Nat Biotechnol* **24**, 703-707 (2006).
59. S. M. Park *et al.*, Molecular profiling of single circulating tumor cells from lung cancer patients. *Proceedings of the National Academy of Sciences of the United States of America* **113**, E8379-E8386 (2016).
60. D. K. Wood, D. M. Weingeist, S. N. Bhatia, B. P. Engelward, Single cell trapping and DNA damage analysis using microwell arrays. *Proceedings of the National Academy of Sciences of the United States of America* **107**, 10008-10013 (2010).
61. J. Gole *et al.*, Massively parallel polymerase cloning and genome sequencing of single cells using nanoliter microwells. *Nat Biotechnol* **31**, 1126-1132 (2013).
62. G. F. Christopher, S. L. Anna, Microfluidic methods for generating continuous droplet streams. *Journal of Physics D: Applied Physics* **40**, R319-R336 (2007).
63. A. V. Lemmo, J. T. Fisher, H. M. Geysen, D. J. Rose, Characterization of an inkjet chemical microdispenser for combinatorial library synthesis. *Analytical chemistry* **69**, 543-551 (1997).
64. T. B. Jones, M. Gunji, M. Washizu, M. J. Feldman, Dielectrophoretic liquid actuation and nanodroplet formation. *Journal of Applied Physics* **89**, 1441-1448 (2001).
65. S. Lindstrom, H. Andersson-Svahn, Overview of single-cell analyses:

microdevices and applications. *Lab on a chip* **10**, 3363-3372 (2010).

66. T. P. Lagus, J. F. Edd, A review of the theory, methods and recent applications of high-throughput single-cell droplet microfluidics. *Journal of Physics D: Applied Physics* **46**, 114005 (2013).
67. D. Hummer, F. Kurth, N. Naredi-Rainer, P. S. Dittrich, Single cells in confined volumes: microchambers and microdroplets. *Lab on a chip* **16**, 447-458 (2016).
68. J. R. Kovac, J. Voldman, Intuitive, image-based cell sorting using optofluidic cell sorting. *Analytical chemistry* **79**, 9321-9330 (2007).
69. W. H. Tan, S. Takeuchi, A trap-and-release integrated microfluidic system for dynamic microarray applications. *Proceedings of the National Academy of Sciences of the United States of America* **104**, 1146-1151 (2007).
70. W. H. Tan, S. Takeuchi, Dynamic microarray system with gentle retrieval mechanism for cell-encapsulating hydrogel beads. *Lab on a chip* **8**, 259-266 (2008).
71. Z. Zhu, O. Frey, D. S. Ottoz, F. Rudolf, A. Hierlemann, Microfluidic single-cell cultivation chip with controllable immobilization and selective release of yeast cells. *Lab on a chip* **12**, 906-915 (2012).
72. A. Morimoto *et al.*, High-Density Dielectrophoretic Microwell Array for Detection, Capture, and Single-Cell Analysis of Rare Tumor Cells in Peripheral Blood. *PloS one* **10**, e0130418 (2015).
73. H. S. Kim, T. P. Devarenne, A. Han, A high-throughput microfluidic single-cell screening platform capable of selective cell extraction. *Lab on a chip* **15**, 2467-2475 (2015).
74. D. J. Collins, A. Neild, A. deMello, A. Q. Liu, Y. Ai, The Poisson distribution and beyond: methods for microfluidic droplet production and single cell encapsulation. *Lab on a chip* **15**, 3439-3459 (2015).
75. T. C. Chang *et al.*, Microwell arrays reveal cellular heterogeneity during the clonal expansion of transformed human cells. *Technology (Singap World Sci)* **3**, 163-171 (2015).
76. L. I. Lin, S. H. Chao, D. R. Meldrum, Practical, microfabrication-free device for single-cell isolation. *PloS one* **4**, e6710 (2009).
77. H. Kaji, G. Camci-Unal, R. Langer, A. Khademhosseini, Engineering systems for

the generation of patterned co-cultures for controlling cell-cell interactions. *Biochim Biophys Acta* **1810**, 239-250 (2011).

78. W. F. Liu, C. S. Chen, Cellular and multicellular form and function. *Adv Drug Deliv Rev* **59**, 1319-1328 (2007).
79. A. Khademhosseini, R. Langer, J. Borenstein, J. P. Vacanti, Microscale technologies for tissue engineering and biology. *Proceedings of the National Academy of Sciences of the United States of America* **103**, 2480-2487 (2006).
80. J. Fukuda *et al.*, Micropatterned cell co-cultures using layer-by-layer deposition of extracellular matrix components. *Biomaterials* **27**, 1479-1486 (2006).
81. J. Tien, C. M. Nelson, C. S. Chen, Fabrication of aligned microstructures with a single elastomeric stamp. *Proceedings of the National Academy of Sciences of the United States of America* **99**, 1758-1762 (2002).
82. S. Takayama *et al.*, Patterning cells and their environments using multiple laminar fluid flows in capillary networks. *Proceedings of the National Academy of Sciences of the United States of America* **96**, 5545-5548 (1999).
83. M. Suzuki, T. Yasukawa, H. Shiku, T. Matsue, Negative dielectrophoretic patterning with different cell types. *Biosens Bioelectron* **24**, 1049-1053 (2008).
84. S. N. Bhatia, U. J. Balis, M. L. Yarmush, M. Toner, Microfabrication of hepatocyte/fibroblast co-cultures: role of homotypic cell interactions. *Biotechnology progress* **14**, 378-387 (1998).
85. F. Pampaloni, E. G. Reynaud, E. H. K. Stelzer, The third dimension bridges the gap between cell culture and live tissue. *Nat Rev Mol Cell Bio* **8**, 839-845 (2007).
86. S. Kim, H. Lee, M. Chung, N. L. Jeon, Engineering of functional, perfusable 3D microvascular networks on a chip. *Lab on a chip* **13**, 1489-1500 (2013).
87. Y. Du, E. Lo, S. Ali, A. Khademhosseini, Directed assembly of cell-laden microgels for fabrication of 3D tissue constructs. *Proceedings of the National Academy of Sciences of the United States of America* **105**, 9522-9527 (2008).
88. M. Kang *et al.*, Capillarity Guided Patterning of Microliquids. *Small* **11**, 2789-2797 (2015).
89. W. F. Liu, C. S. Chen, Cellular and multicellular form and function. *Adv Drug Deliver Rev* **59**, 1319-1328 (2007).
90. D. Huh, G. A. Hamilton, D. E. Ingber, From 3D cell culture to organs-on-chips.

Trends Cell Biol **21**, 745-754 (2011).

91. K. Yum, S. G. Hong, K. E. Healy, L. P. Lee, Physiologically relevant organs on chips. *Biotechnol J* **9**, 16-27 (2014).
92. C. Moraes, G. Mehta, S. C. Lesher-Perez, S. Takayama, Organs-on-a-chip: a focus on compartmentalized microdevices. *Ann Biomed Eng* **40**, 1211-1227 (2012).
93. S. Kim, H. Lee, M. Chung, N. L. Jeon, Engineering of functional, perfusable 3D microvascular networks on a chip. *Lab on a Chip* **13**, (2013).
94. S.-R. Lee *et al.*, Modeling neural circuit, blood–brain barrier, and myelination on a microfluidic 96 well plate. *Biofabrication* **11**, (2019).
95. M. Campisi *et al.*, 3D self-organized microvascular model of the human blood-brain barrier with endothelial cells, pericytes and astrocytes. *Biomaterials* **180**, 117-129 (2018).
96. J. S. Jeon *et al.*, Human 3D vascularized organotypic microfluidic assays to study breast cancer cell extravasation. *Proc Natl Acad Sci U S A* **112**, 214-219 (2015).
97. S. H. Lee *et al.*, Capillary based patterning of cellular communities in laterally open channels. *Anal Chem* **82**, 2900-2906 (2010).
98. B. P. Casavant *et al.*, Suspended microfluidics. *Proceedings of the National Academy of Sciences of the United States of America* **110**, 10111-10116 (2013).
99. Y. Lee *et al.*, Microfluidics within a well: an injection-molded plastic array 3D culture platform. *Lab Chip* **18**, 2433-2440 (2018).
100. S. Lee *et al.*, Engineering tumor vasculature on an injection-molded plastic array 3D culture (IMPACT) platform. *Lab Chip* **19**, 2071-2080 (2019).
101. J. Berthier, K. A. Brakke, E. Berthier, *Open microfluidics*. (John Wiley & Sons, 2016).
102. J. Ko *et al.*, Tumor spheroid-on-a-chip: a standardized microfluidic culture platform for investigating tumor angiogenesis. *Lab Chip* **19**, 2822-2833 (2019).
103. P.-G. De Gennes, F. Brochard-Wyart, D. Quéré, *Capillarity and wetting phenomena: drops, bubbles, pearls, waves*. (Springer Science & Business Media, 2013).
104. J. Ko, Y. Lee, S. Lee, S. R. Lee, N. L. Jeon, Human Ocular Angiogenesis-Inspired Vascular Models on an Injection-Molded Microfluidic Chip. *Adv Healthc Mater* **8**, e1900328 (2019).

105. X. Wang *et al.*, Engineering anastomosis between living capillary networks and endothelial cell-lined microfluidic channels. *Lab Chip* **16**, 282-290 (2016).
106. S. A. Rosenberg, N. P. Restifo, Adoptive cell transfer as personalized immunotherapy for human cancer. *Science* **348**, 62-68 (2015).
107. S. L. Maude *et al.*, Chimeric antigen receptor T cells for sustained remissions in leukemia. *N Engl J Med* **371**, 1507-1517 (2014).
108. D. L. Porter, B. L. Levine, M. Kalos, A. Bagg, C. H. June, Chimeric antigen receptor–modified T cells in chronic lymphoid leukemia. *New England Journal of Medicine* **365**, 725-733 (2011).
109. J. N. Kochenderfer *et al.*, Eradication of B-lineage cells and regression of lymphoma in a patient treated with autologous T cells genetically engineered to recognize CD19. *Blood* **116**, 4099-4102 (2010).
110. C. H. June, R. S. O'Connor, O. U. Kawalekar, S. Ghassemi, M. C. Milone, CAR T cell immunotherapy for human cancer. *Science* **359**, 1361-1365 (2018).
111. W. A. Lim, C. H. June, The Principles of Engineering Immune Cells to Treat Cancer. *Cell* **168**, 724-740 (2017).
112. C. Guillerey, N. D. Huntington, M. J. Smyth, Targeting natural killer cells in cancer immunotherapy. *Nat Immunol* **17**, 1025-1036 (2016).
113. R. Handgretinger, K. Schilbach, The potential role of gammadelta T cells after allogeneic HCT for leukemia. *Blood* **131**, 1063-1072 (2018).
114. J. A. Joyce, D. T. Fearon, T cell exclusion, immune privilege, and the tumor microenvironment. *Science* **348**, 74-80 (2015).
115. M. M. D'Aloia, I. G. Zizzari, B. Sacchetti, L. Pierelli, M. Alimandi, CAR-T cells: the long and winding road to solid tumors. *Cell Death Dis* **9**, 282 (2018).
116. M. Binnewies *et al.*, Understanding the tumor immune microenvironment (TIME) for effective therapy. *Nat Med* **24**, 541-550 (2018).
117. K. G. Anderson, I. M. Stromnes, P. D. Greenberg, Obstacles Posed by the Tumor Microenvironment to T cell Activity: A Case for Synergistic Therapies. *Cancer Cell* **31**, 311-325 (2017).
118. D. E. Speiser, P. C. Ho, G. Verdeil, Regulatory circuits of T cell function in cancer. *Nat Rev Immunol* **16**, 599-611 (2016).
119. H. Salmon *et al.*, Matrix architecture defines the preferential localization and

migration of T cells into the stroma of human lung tumors. *J Clin Invest* **122**, 899-910 (2012).

120. K. Ganesh, J. Massague, TGF-beta Inhibition and Immunotherapy: Checkmate. *Immunity* **48**, 626-628 (2018).
121. R. Lichtenfels, W. E. Biddison, H. Schulz, A. B. Vogt, R. Martin, CARE-LASS (calcein-release-assay), an improved fluorescence-based test system to measure cytotoxic T lymphocyte activity. *J Immunol Methods* **172**, 227-239 (1994).
122. K. Brunner, J. Mauel, J.-C. Cerottini, B. Chapuis, Quantitative assay of the lytic action of immune lymphoid cells of 51Cr-labelled allogeneic target cells in vitro; inhibition by isoantibody and by drugs. *Immunology* **14**, 181 (1968).
123. W. J. Polacheck, R. Li, S. G. Uzel, R. D. Kamm, Microfluidic platforms for mechanobiology. *Lab Chip* **13**, 2252-2267 (2013).
124. G. Adriani *et al.*, Microfluidic models for adoptive cell-mediated cancer immunotherapies. *Drug Discov Today* **21**, 1472-1478 (2016).
125. A. Pavesi *et al.*, A 3D microfluidic model for preclinical evaluation of TCR-engineered T cells against solid tumors. *JCI Insight* **2**, (2017).
126. S. W. L. Lee *et al.*, Characterizing the Role of Monocytes in T Cell Cancer Immunotherapy Using a 3D Microfluidic Model. *Front Immunol* **9**, 416 (2018).
127. J. M. Ayuso *et al.*, Evaluating natural killer cell cytotoxicity against solid tumors using a microfluidic model. *OncoImmunology*, 1-11 (2018).
128. Y. Shin *et al.*, Microfluidic assay for simultaneous culture of multiple cell types on surfaces or within hydrogels. *Nat Protoc* **7**, 1247-1259 (2012).
129. N. J. Waterhouse *et al.*, Cytotoxic T lymphocyte-induced killing in the absence of granzymes A and B is unique and distinct from both apoptosis and perforin-dependent lysis. *J Cell Biol* **173**, 133-144 (2006).
130. J. Deguine, B. Breart, F. Lemaitre, J. P. Di Santo, P. Bousso, Intravital imaging reveals distinct dynamics for natural killer and CD8(+) T cells during tumor regression. *Immunity* **33**, 632-644 (2010).
131. J. J. Northey, L. Przybyla, V. M. Weaver, Tissue Force Programs Cell Fate and Tumor Aggression. *Cancer Discov* **7**, 1224-1237 (2017).
132. H. Jiang, S. Hegde, D. G. DeNardo, Tumor-associated fibrosis as a regulator of tumor immunity and response to immunotherapy. *Cancer Immunol Immunother*

66, 1037-1048 (2017).

133. N. Nagarsheth, M. S. Wicha, W. Zou, Chemokines in the cancer microenvironment and their relevance in cancer immunotherapy. *Nat Rev Immunol* **17**, 559-572 (2017).
134. K. Wolf *et al.*, Collagen-based cell migration models in vitro and in vivo. *Semin Cell Dev Biol* **20**, 931-941 (2009).
135. K. Wolf *et al.*, Physical limits of cell migration: control by ECM space and nuclear deformation and tuning by proteolysis and traction force. *J Cell Biol* **201**, 1069-1084 (2013).
136. R. Basu *et al.*, Cytotoxic T Cells Use Mechanical Force to Potentiate Target Cell Killing. *Cell* **165**, 100-110 (2016).

초록

장기모사칩은 2000년대 초부터 마이크로 공정 기술이 생물학적 연구에 활용됨에 따라 인간 장기 기능을 모사하기 위해 개발되었다. 구체적으로, polydimethylsiloxane (PDMS) 기반 미세유체 장치는 공간적으로 구분된 세포 패터닝을 가능케 함으로써 생체와 유사한 구조로 세포를 배양할 수 있게 해주었다. 이러한 세포 패터닝은 페트리 디쉬, 플라스크, 혹은 웰플레이트와 같은 기존의 세포 배양 도구에서는 수행하기 어려운 삼차원 세포 배양과 그 안에서의 시공간적 분석을 가능하게 하였다. 하지만, 종래의 장기모사칩은 PDMS에 기반한 닫힌 형태의 채널 설계로 인해 낮은 생산성, 낮은 실험 효율, 낮은 장비 호환성을 갖는다. 따라서, 본 연구는 대중적인 세포 배양 장치들에 마이크로 구조물을 통합한 두가지 모세관 현상 기반의 패터닝 방법을 제시한다. 첫번째 방법은 페트리 디쉬나 polystyrene (PS) 필름과 같이 개방된 PS 표면에 마이크로 기둥 어레이를 제작하여 그 위에서 액체가 쓸려 지나갈 때 기둥 구조물들 사이에 액체를 포획하는 방식이다. 마이크로 기둥 어레이의 배치에 따라 나노리터부터 마이크로리터에 이르는 액체를 빠르게 패터닝할 수 있게 한다. 이러한 기둥 구조를 활용하면 다양한 세포의 배치 및 배양이 가능하여, 본 연구에서는 삼차원 환경에서의 단일세포 배양과 다세포 공배양 플랫폼으로의 활용 가능성을 제시하였다. 두번째 방법은 마이크로 레일 형태의 마이크로구조물을 표준화된 마이크로 플레이트의 웰과

통합하여 고효율 삼차원 배양 플랫폼을 제시한다. 레일 구조의 아래에 주입된 액체가 빨아들여질 때 구조물에 의해 형성된 액체-기체 계면들의 순차적 이동을 활용하여 특정 레일의 아래에만 액체를 남기는 기술을 개발하였다. 이 두가지 모세관 현상 기반 패터닝 방법을 위한 장치들은 사출성형으로 대량생산이 가능하고 우수한 실험 효율을 갖는다. 이 중 레일 구조를 활용한 흡인 기반의 패터닝 방법을 이용하여 면역세포치료제의 성능 평가를 위한 사출 성형된 플라스틱 어레이 배양 장치(CACI-IMPACT)를 개발하였다. 흡인 기반 패터닝 덕분에 20 μl 파이펫으로 빨아들인 하이드로젤 용액을 30 초 이내에 12개의 웰에 패터닝 할 수 있었다. 면역세포치료제의 기능적 평가를 위해, 콜라겐 젤에 포함된 HeLa 세포를 패터닝하고 NK-92 세포의 콜라겐 매트릭스 내부로의 침투, 매트릭스 내부에서의 이동 및 암세포 살해 활동을 관찰하였다. 이를 통해 세포외기질이 세포 독성 림프구의 이동 및 세포 독성에 상당히 영향을 미친다는 것을 확인할 수 있었다. 따라서, 암세포와 세포 독성 림프구의 고효율 삼차원 공동 배양을 가능하게 하는 본 플랫폼은 고형 종양에 대한 면역 치료를 위해 개발된 세포 독성 림프구의 전임상 평가에 사용될 가능성이 있으며, 본 연구에서 개발 및 사용된 모세관 현상 기반 패터닝 기술들은 장기모사칩의 상용화를 가속화시킬 것으로 기대한다.